



HAL
open science

Laser Nonlinear Propagation In Gases: The Properties And Applications

Bing Zhou

► **To cite this version:**

Bing Zhou. Laser Nonlinear Propagation In Gases: The Properties And Applications. Plasma Physics [physics.plasm-ph]. Ecole Polytechnique X, 2011. English. NNT: . pastel-00604381

HAL Id: pastel-00604381

<https://pastel.hal.science/pastel-00604381>

Submitted on 28 Jun 2011

HAL is a multi-disciplinary open access archive for the deposit and dissemination of scientific research documents, whether they are published or not. The documents may come from teaching and research institutions in France or abroad, or from public or private research centers.

L'archive ouverte pluridisciplinaire **HAL**, est destinée au dépôt et à la diffusion de documents scientifiques de niveau recherche, publiés ou non, émanant des établissements d'enseignement et de recherche français ou étrangers, des laboratoires publics ou privés.

École Polytechnique(X)

DOCTORAL SCHOOL

Ph.D. Thesis from

École Polytechnique

Specialty: PHYSICS

Nonlinear Propagation of a Femtosecond
Laser Pulse in Gases: Properties and
Applications

Bing ZHOU

prepared at Laboratoire d'Optique Appliquée, ILM Group

defended on November 23, 2010

Jury:

<i>Reviewers:</i>	Jens BIEGERT	- ICFO (Spain)
	Danilo GIULIETTI	- University of Pisa (Italy)
<i>Thesis advisor:</i>	André MYSYROWICZ	- LOA (École Polytechnique)
<i>President:</i>	Patrick MORA	- CPHT (École Polytechnique)
<i>Examinators:</i>	Arnaud COUAIRON	- CPHT (École Polytechnique)
	Jean LAROUB	- LPP (École Polytechnique)
	Jérôme FAURE	- LSI (École Polytechnique)
	Selcuk AKTURK	- Istanbul Technical University (Turkey)



Acknowledgments

This is the time for a last and personal word. During those three years in Palaiseau, I have met a lot of people outside and inside the work that contributed to make my dissertation possible and enjoyable. So the purpose of these pages is to thank all of them.

First of all, I would like to thank the former director of Laboratoire d'Optique Appliquée Professor Gérard MOUROU, and the present director Professor Antoine ROUSSE. Thank you for allowing me to study in such a dynamic and prestigious laboratory.

I am also deeply indebted to Professeur André MYSYROWICZ. His positive attitudes and kind words have guided me during the last three years.

I must express my gratitude to Bernard PRADE. His physical insight, writing skills and diligence for the corrections of my manuscript helped me a lot.

Selcuk AKTURK has always provided wonderful insight and timely commentary. At early stage of the doctoral process, he was always encouraging and provided me motivation to forge ahead. Moreover, I have learned many experimental skills during the years that I worked with Selcuk AKTURK.

I am grateful to Yi LIU, Aurélien HOUARD and Michel FRANCO. It was always a pleasure to share with you new results and your constant cheering, interest and enthusiasm allowed me to push through and complete this thesis.

Cord ARNOLD has also provided great insight to my research ideas. He has been very supportive and has always had a kind humor.

Although doing a PhD is a painful process, one needs many people to collaborate with, whose skills allow the project to mature. Thanks to Professeur Paul CORKUM, Arnaud COUAIRON, Jean LAROUR and Christopher SMEENK. The discussions with them are always enlightening and constructive, I greatly appreciate. I also would like to thank Estelle SALMON, Noelle LASCoux and Zhuqiang HAO, who have worked with me on the plasma revival experiment with Teramobile laser.

Thanks to Benjamin FORESTIER. He spent a lot of time to correct my manuscript.

Jérôme CARBONNEL, Armino DOS SANTOS, Yves-Bernard ANDRE always provide timely support to enable experiments go well. Thank you for your support.

Furthermore, to my other colleagues Magali DURAND, Amélie JARNAC, Shihua CHEN, I want to say that it was a real pleasure to work with you.

I would like to thank the members of my dissertation committee, Professeur Patrick MORA, Arnaud COUAIRON, Professeur Jens BIEGERT, Professeur Danilo GIULIETTI, Jean LAROUR, Jerome FAURE, Selcuk AKTURK, for accepting to participate to my Ph.D. defense.

I would also like to thank all of the other LOA members, and my fellow graduate students for their help and support. Finally, I must convey my heartiest thanks to my family, friends, and my girlfriend for all of their support and encouragement, which I needed to see the doctoral study up to the end.

Contents

1	Introduction	1
1.1	Introduction	1
1.2	Principle of laser filamentation	5
2	Femtosecond laser induced plasma channel formed with an axicon	11
2.1	Properties of an axicon in the linear regime	11
2.1.1	Introduction	11
2.1.2	Comparison of intensity profiles between an ideal and a real axicon	12
2.1.3	Comparison between experiments and simulations	14
2.2	Properties of an axicon in the nonlinear regime	18
2.2.1	The formation of a long plasma channel by a lens and an axicon	19
2.2.2	Simulation of Bessel beams generated plasma channel	24
2.2.3	Discussion on laser propagation with an axicon	27
2.3	Conclusion	27
3	Revival of femtosecond laser plasma filaments in air by a nanosecond laser	31
3.1	Temporal evolution of the plasma density and determination of plasma lifetime	31
3.2	Experimental methods to increase the plasma lifetime with a double pulse technique	32
3.3	Revival of femtosecond laser plasma filaments with another nanosecond laser	34
3.3.1	Simulation and Results of the plasma revival	34
3.3.2	Optical breakdown inside the plasma channel revived with two nanosecond lasers	37
3.3.3	Experimental evidence for the existence of N_4^+	37
3.4	Conclusion of plasma revival	40
4	Measurement and control of longitudinal electric currents in the wake of femtosecond laser pulses in gases	43
4.1	A specially designed air-core high speed current monitor	45
4.1.1	Bi-components of B field near a filament	46
4.1.2	A specially designed high speed current monitor	47
4.1.3	Current signal inside a femtosecond filament	50
4.2	Oscillating currents inside femtosecond filaments	53
4.2.1	Oscillating current inside a filament plasma with external static electric field	54
4.2.2	Oscillating currents in nitrogen gas	55

4.2.3	The oscillating currents in Argon gas	61
4.2.4	The oscillating currents in other gases	64
4.3	A homeostasis of two forces inside a filament plasma	66
4.3.1	A classic model for an electron with laser field	66
4.3.2	The homeostasis inside a plasma column	69
4.4	The plasma oscillating currents in dilute air	73
4.4.1	A single plasma channel in dilute air	74
4.4.2	Laser intensity dependence of the currents in a non filament plasma channel	78
4.4.3	Laser polarization and gas pressure dependence of the currents in a non filament plasma channel	79
4.5	Controlled oscillating current with Bi-color laser pulse inside a filament	81
4.6	Conclusion on the oscillating current inside the laser induced plasma channel	83
5	Few-Cycle Pulses by External Compression	87
5.1	Ultra short laser pulse internal and external compression	88
5.1.1	Few cycle laser pulse compression by a gas filled hollow fiber .	89
5.1.2	Self-compression of optical laser pulses by filamentation . . .	90
5.2	Compression of ultrashort high energy laser pulses in planar hollow waveguides	93
5.2.1	Basic waveguide theory	94
5.2.2	Nonlinear pulse propagation in planar hollow waveguides . . .	96
5.2.3	Simulations of laser pulse propagation in planar waveguide . .	99
5.3	Experimental results of laser pulse compression in a planar waveguide	106
5.3.1	Experimental setup	106
5.3.2	Waveguide construction	107
5.3.3	Dependence of pulse compression on gas type and pressure . .	109
5.3.4	Variation of pulse duration along the beam transverse dimension	110
5.3.5	Spatial phase and focusability	112
5.3.6	Optimization of input pulse duration	115
5.4	Generation of a filament plasma in helium gas with few-cycle pulses .	116
5.5	Conclusion	117
6	Conclusion	121
7	Appendix	123
7.1	Ponderomotive energy and electron kinetic energy in a strong laser field	123
7.2	The motion of an electron with linearly polarized laser field	123
7.2.1	Electric field and the vector potential	123
7.2.2	Longitudinal Electron momentum	124
7.2.3	The ponderomotive force	124
7.2.4	Determination of $p_{//,0}$	125

7.3	The motion of an electron with circularly polarized laser field	127
7.4	Several optical devices and optical elements	128
7.4.1	Dispersive Chirped Mirrors	128
7.4.2	Dazzler: Acousto-Optic Modulators for Dispersion Compensation	130
7.4.3	SPIDER	131
7.4.4	FROG	132
7.5	Several processes in a plasma	134
7.5.1	Ionization	134
7.5.2	Electron collision inside the plasma	136
8	Appendix	141
8.1	Personal publication	141
8.2	International conference	142
	Bibliography	145

Chapter 1: Introduction

Introduction

Contents

1.1 Introduction	1
1.2 Principle of laser filamentation	5

1.1 Introduction

Laser technology has achieved remarkable progress during the past 50 years. It now allows us to obtain ultrashort optical pulses with peak powers well beyond the TW level. If such an intense ultrashort pulse is sent through atmosphere, it undergoes spectacular spatial, spectral and temporal changes, due to the cumulative optical nonlinearities it induces in the medium. In particular these changes give rise to a phenomenon called filamentation. Generally speaking, when the power of a femtosecond laser pulse reaches the critical power, the femtosecond laser beam will self collapse during the propagation. As a result, the intensity of the laser beam is high enough to ionize the media. Due to the dynamic competition between the self-focusing and plasma defocusing, there is a long thin channel formed over long distance. The first demonstration of femtosecond filamentation in air was reported by Braun *et al.* in 1995 [Braun 1995], and reproduced over longer distances 6 months later at Laboratoire d'Optique Appliquée in France [Nibbering 1996]. Femtosecond laser filamentation has been extensively studied in the laboratory during the past decade, thereby many interesting phenomena and application have been revealed. For instance, the white light continuum generated during self-guided propagation can be used for the detection of pollutants in the atmosphere by LIDAR technique [Yu 2001, Kasparian 2001, Bourayou 2005]; the creation of plasma channels in a filament can trigger and guide high-voltage discharges and could be used to control lightning [Comtois 2000, Rodriguez 2002, Ackermann 2004]; high local intensities can be used to identify targets at distance by laser induced Plasma Spectroscopy (LIPS) [Stelmaszczyk 2004]; the filament plasma can also deliver broadband THz radiation at long distances [D'Amico 2007, Houard 2008].

In the thesis, I have studied several new aspects of filamentation. The plan of my thesis is the following:

In the second chapter, I will study a novel type of filaments which is formed by focusing a femtosecond laser pulse in air with an axicon lens. This is the first time

that the filament formed by a Bessel beam in air has been studied experimentally in the nonlinear regime. With a conventional spherical lens, it is difficult to generate in laboratory a long filament at a short distance from the laser. A conical lens, axicons, has found an increasing use in optical applications, since their invention by McLeod [McLeod 1954]. The non-diffracting Bessel beams can retain high laser intensities over long distances [Durnin 1987]. Durfee and Milchberg [Durfee 1993] used an axicon to form laser-generated plasma in argon, which then served as a waveguide for another laser beam. Recently, Roskey *et al.* [Roskey 2007] have theoretically studied nonlinear propagation of axicon-focused beams in air, and predicted that underdense plasma channels may accompany the beams.

Laser beams propagating through axicons have mainly two significant properties: a on-axis line focus and ring-like profiles in the far field. Through an axicon the laser beam becomes much less diffractive. First I have characterized the linear propagation of the laser pulse after an axicon. Second, I experimentally observed the nonlinear propagation and the formation of a filament using an axicon. Lastly I have made a comparison between the characteristics of a filament formed by an axicon and those of a filament formed by a converging intense femtosecond pulse in the laboratory. I have also compared the experimental measurements with the numerical simulations. The consistency between the experiments and the simulations proves that the theoretical model is correct, subsequently more simulations will be presented to investigate the nonlinear propagation through an axicon.

In the third chapter, I will study the remnant signature of a filament long after the passage of the laser pulse and study a new method to increase the plasma lifetime. When a filament is formed in the atmosphere due to recombination and attachment processes, the number of electrons drops off rapidly, therefore the plasma lifetime limited to a few nanoseconds [Zhao 1995]. There have been several attempts to increase the filament plasma lifetime by using a second laser [Yang 2002, Hao 2005]. However, in all of these previous works, the plasma lifetime is increased at early times while free electrons are still present and the longitudinal extent of the effect is limited to the Rayleigh length of the focused nanosecond laser beam.

I will show that it is possible to revive the plasma track of a filament by the use of a delayed nanosecond laser pulse long after that the free electrons drop to negligible. The principle is to exploit the storage of weakly bound electrons onto oxygen molecules following the formation of the original plasma channel. The attached electrons provide a reservoir with a memory of the geometry of the filament over a time corresponding to the ion-ion recombination and diffusion of the negative oxygen molecules out of the initial filament core. During the plasma revival, the detachment and multiplication processes are not sensitive to the peak power of the laser pulse, but to the number of photons within a laser pulse. With sufficient ns laser pulse's energy, I will demonstrate the filament plasma can be revived up to a hundred ns. With two separated ns laser pulse, I will show that the full ionized plasma can be obtained directly. The revival can be interesting for future applications which require to increase the lifetime of the plasma column

formed during the filamentation process.

In the fourth chapter, I will study the longitudinal movement of free electrons that are produced during the filamentation process with a special designed current monitor. Short-lived longitudinal oscillating currents are initially excited within the short-existed plasma, as evidenced by the pulsed conical THz radiation emitted by filaments in the forward direction [D'Amico 2007, Houard 2007]. The mastering of these longitudinal currents are vital for the long term goal of grasping the electrons' movement and collisions in the atmosphere by intense short laser pulses [Esarey 2009].

In previous attempts to detect the longitudinal current, a Canadian group used a monopole antenna placed in the vicinity of the filament [Proulx 2000] to detect the radiation E field generated by the plasma column, and to estimate the distribution of free electrons in the plasma channel. However E field near the plasma column is too complex to analyze the measured signal. I will present a specially designed high speed current monitor along with its characteristics; this allows us to detect longitudinal currents with a good sensitivity. Then I will show how to process and characterize the current signal. A large set of currents inside a filament plasma as a function of gases, gas pressure, and laser polarizations will be presented. Based on the set of currents in different gases, the various dynamic aspects of the plasma channels will be discussed. Finally, a new model will be proposed to better understanding of THz generation and electron oscillations in a filament plasma formed by femtosecond laser pulses. I will interpret all the experimental results with a physical model, in which we calculate the total laser force acting on the free electrons, and qualitatively evaluate the coulomb force acting on the opposite direction.

The work presented in the last chapter concerns the long range goal of studying the filamentation in He gas. The filamentation in He is interesting, because it leads to self guided pulse with a peak intensity one order of magnitude higher than the one in air. To generate a filament in He, one needs to compress the laser pulse down to a few optical cycle. The general scheme of light pulse compression is the following [Couairon 2005a]. The input pulse is first injected into a phase modulator, which broadens the pulse spectrum imposing a frequency sweep (in time). The spectrally broadened and chirped pulse is sent in a dispersive delay line, which rephases all the new frequency components generated by the phase modulation. Ideally, the dispersive delay line would introduce the opposite chirp on the pulse, thus resulting in the compression of the pulse to its minimum width, $1/\Delta\omega$, where $\Delta\omega$ is the frequency sweep imposed on the pulse in the first step. Further, to compress femtosecond pulses, an ultrafast phase modulator has to be used.

Perspectives in the use of the hollow-fiber technique are related to its energy scalability. The technique can be easily employed up to mJ-level laser pulses; the upgrade toward higher energies (tens of mJ) is hindered by gas ionization, thus appearing to be problematic. Furthermore, it is hard to control the laser pulses to keep good coupling with the capillary and avoid damage of the fiber entrance. Therefore to gain the few cycle laser pulse with pulse-energy extending to tens of

mJ, a new way to compress the high energy pulse is necessary.

By filamentation, few cycle laser pulses can be reliably achieved. This technique presents a robust and simple alternative to hollow fiber pulse compression. The following aspects are unique to this technique: the filamentary propagation has been shown to yield an output pulse with a flat phase front, a feature confirmed by the experiments simulations. Furthermore, because filamentation is arrested by multi-photon ionization, a process scaling as intensity to the eleventh power in argon, a very effective intensity clamping is achieved. However, the shortcoming for filamentation is still obvious: the laser pulses energy can not go up to more than mJ. The high harmonics generation, which requires high pulse energy, is still crippled, therefore there is a need for a more sound way to compress the laser pulse.

With the planar hollow waveguide, as compared with the hollow capillaries and filamentation, is the superior scalability to high laser pulse energy, when the laser pulse was compressed down to few cycle regime. The energy level of 100 mJ for the compression of ultrashort pulses to the few-cycle regime could in principle be further increased by the choice of noble gases with higher ionization potential (Ne and He) as well as by increasing the waveguide separation. Furthermore, the transverse non-linear dynamics in the free waveguide dimension influence the output mode quality, the pulse duration, and the focusability of the output pulse. These aspects were in detail addressed both experimentally and numerically, and furthermore the possible improvements were highlighted. Based on the theoretical model and simulation, the region of stable waveguide propagation and its impact on energy scalability were investigated, which are in excellent agreement with experimental results.

I have contributed to the assembly of the planar hollow waveguide compression set-up, which includes a pulse compression system (down to 10 fs), and the associated short pulse diagnostic system. I will present the first results showing evidence for the filamentation in Helium.

Although I have been involved in all results presented in this thesis manuscript, there are many contributions from different colleagues who I want to recognize in the end.

The work on axicon has been directed by S. Akturk during his stay at LOA as a postdoc. S. Akturk has also designed and constructed the FROG system allowing to measure the laser pulse down to signal cycle duration. C. Arnold and S. Chen have been main contributors to the development and theoretical analysis of the planar compression stage (see Chapter 5). A. Couairon and P. Mora have calculated the laser force acting on a free electrons (see Appendix). Finally I received a lot of help from B. Prade, J. Larour, Y. Liu and A. Houard. Thank you to all my colleagues.

1.2 Principle of laser filamentation

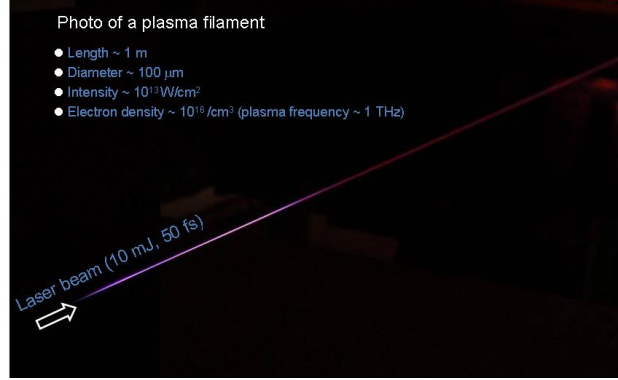


Figure 1.1: A photo of a filament. The laser pulse is 15 mJ, 45 fs. The focal length of the lens is 2 m. The filament length is 1 m, the diameter is 100 μm .

As I mentioned before, a filament results in the competition between the self-focusing and plasma defocusing. Figure 1.1 shows the femtosecond laser induced filament in air (1 bar). The fluorescence is emitted by laser induced excited nitrogen molecules. The laser pulse is 15 mJ, 45 fs. The focal length of the lens is 2 m. The filament length is 1 m, the diameter is 100 μm . During the laser filamentation process, the laser pulse undergoes two major effects:

The optical Kerr effect: When an intense laser propagates in a transparent medium, the refractive index n varies as described by $n = n_0 + n_2 I$ [Stolen 1989, Stolen 1992], where n_0 and n_2 are the linear and non-linear components of the refractive index, and I is the intensity of the laser. Since n_2 is positive in most materials, the refractive index becomes larger in the areas where the intensity is higher, usually at the center of a beam, creating a focusing density profile, leading to a self-focusing which cannot be arrested by diffraction, if the laser power is greater than the critical power [Marburger 1975]:

$$P_{cr} = \alpha \frac{\lambda^2}{4\pi n_0 n_2}, \quad (1.1)$$

where λ is the radiation wavelength in vacuum and α is a constant which depends on the initial spatial distribution of the beam. There is no general analytical expression for α , and its value has been derived numerically for many beam profiles. For a Gaussian beam $\alpha = 1.8962$, and for air $n_0 = 1$, $n_2 = 2.3 \times 10^{-19} \text{ cm}^2/\text{W}$ at $\lambda = 800 \text{ nm}$, and the critical power is then $P_{cr} \approx 5 \text{ GW}$, corresponding to an energy of about 0.3 mJ for a pulse duration of 100 fs.

The plasma defocusing: when the laser beam focuses, its intensity becomes so high that it ionizes the medium. Normally, the generation of a plasma involves a local reduction in the refraction index [Feit 1974], according to the law:

$$n \simeq n_0 - \frac{\rho(r, t)}{2\rho_c}, \quad (1.2)$$

where $\rho(r, t)$ is the density of free electrons and ρ_c denotes the value of the critical plasma density above which the plasma becomes opaque (for laser central wavelength at 800 nm, $\rho_c = 10^{21} \text{ cm}^{-3}$). The characteristic length L_{PL} for plasma defocusing is defined as the length over which the B-integral ($B = -k_0 \int_0^z \rho/(2n_0\rho_c) dz$) corresponding to the integrated nonlinear phase induced by a fully ionized plasma ($\rho = \rho_{at}$, where ρ_{at} is the neutral atom density) only changes by a factor of one. Following the same reasoning as for the derivation of $L_{SF} = 1/(n_2 k_0 I_0)$, L_{PL} is expressed as a function of the neutral atom density ρ_{at} :

$$L_{PL} = \frac{2n_0\rho_c}{k_0\rho_{at}}. \quad (1.3)$$

For a weakly ionized medium of density ρ , the length scale for plasma defocusing is therefore $L_{PL}\rho_{at}/\rho$. For a gas of density $\rho_{at} = 2 \times 10^{19} \text{ cm}^{-3}$, and an electron density $\rho = 10^{16} \text{ cm}^{-3}$, $L_{PL} \sim 22 \text{ }\mu\text{m}$ and $L_{PL}\rho_{at}/\rho \sim 44 \text{ cm}$. The reduction in the refraction index acts as a divergent lens, preventing the complete collapse of the beam on itself. Notably the forward part of the pulse generates the electron plasma which in turn defocuses mainly the trailing part of the pulse.

The self focusing and plasma defocusing compete each other along the laser pulse propagation inside the medium, as a result, a long filament is formed.

Theoretical description of laser nonlinear propagation during filamentation: In order to capture the physics of filamentation of ultrashort laser pulses in gases, solids and liquids, people started to develop various unidirectional propagation equations and the propagation codes for the numerical simulations. The first numerical simulations in this field started with a minimal model in the form of a nonlinear Schrödinger equation describing the pulse propagation and studying the various physical effects.

Brabec and Krausz (1997) proposed an envelope equation modeling the propagation of pulse of a few optical cycles (2.7 fs at 800nm). The main idea in the derivation of this equation. called the nonlinear envelope equation consists in assuming that the pulse envelope is slowly varying in the propagation direction z , but not in time. An equivalent formulation in the frequency domain was proposed by Bespalov et al [Bespalov 2002]. All high order dispersive terms can be also retained in the propagation equation when it is written in the frequency domain [Gaeta 2000, Couairon 2002, Sprangle 2002]. This extended nonlinear Schrödinger equation (NLSE) can be written as [Couairon 2007]:

$$U \frac{\partial \hat{E}}{\partial z} = \frac{i}{2k} \left[\Delta_{\perp} + \frac{n^2(\omega)\omega^2}{c^2} - k^2 U^2 \right] \hat{E} + F\{N(|E|^2, \rho)E\}. \quad (1.4)$$

Note that we have used the retarded time: $t = t_{lab} - z/v_g$, where v_g is the group velocity of the pulse. The operator Δ_{\perp} denotes the transverse laplacian and F denotes the Fourier transform from the time to the frequency domain. The fields $E(x, y, z, t)$

and $\hat{E}(x, y, z, \omega)$ are representations in the time and frequency domains respectively. The operator U is given by $U \equiv \left(1 + \frac{\omega - \omega_0}{kv_g}\right)$, where ω_0 is the pulse central frequency and k is the wavevector. The function N includes self focusing, plasma defocusing and photoionization effects, and is given by:

$$N(|E|^2, \rho) = T^2 N_{kerr}(|E|^2) + N_{plasma}(\rho) + TN_{MPA}(|E|^2), \quad (1.5)$$

where $T \equiv \left(1 + \frac{i}{\omega_0} \frac{\partial}{\partial t}\right)$ accounts for space-time focusing and self-steepening of the pulse. It also takes into account the deviations from the slowly varying envelope approximation. The Kerr effect term $N_{kerr}(|E|^2)$ results from the intensity dependent refractive index and includes both instantaneous and retarded contributions [Couairon 2003]:

$$N_{kerr}(|E|^2) = ik_0 n_2 \left[(1-f)|E(x, y, z, t)|^2 + f \int_{-\infty}^t R(t-t')|E(x, y, z, t')|^2 dt' \right], \quad (1.6)$$

where n_2 is the nonlinear index of refraction, f is the ratio of the fraction of the delayed contribution and R represents the molecular response of the gas. The delayed contribution is important for simulation in air, as rotational coherence of oxygen and nitrogen molecules are excited by femtosecond laser pulses [Nibbering 1997a, Ripoche 1997]. The plasma and multi-photon absorption (MPA) terms in Eq.(1.7) read:

$$\begin{aligned} N_{plasma}(\rho) &= -\frac{\sigma}{2}(1 + i\omega\tau_c)\rho, \\ N_{MPA}(|E|^2) &= -\frac{W(|E|^2)U_i}{2|E|^2}(\rho_{at} - \rho), \\ \sigma &= \frac{k_0}{2n_0\rho_c} \frac{\omega_0\tau_c}{1 + \omega_0^2\tau_c^2}, \end{aligned} \quad (1.7)$$

where, τ_c is the electron collision time, ρ is the electron density in the plasma, $\rho_c = m_e \varepsilon_0 \omega_0^2 e^{-2}$ is the critical plasma density (over which the plasma becomes opaque), σ is the cross section for inverse Bremsstrahlung [Yablonovitch 1972a], U_i is the ionization potential, ρ_{at} is the density of the neutral atoms and W is the photoionization rate, including multi-photon ionization (MPI) and tunnel ionization contributions.

Note that Eq. (1.6) can only be solved numerically. For this purpose we use a nonlinear propagation code developed by A. Couairon [Couairon 2000]. For instance, figure 1.2 shows the beam width during the filamentation process in air [Couairon 2007]. The laser pulse is 5 mJ, 50 fs, 800 nm. The laser beam self collapses on its axis due to Kerr effect, subsequently the laser intensity reach high enough to ionize the gas, therefore due to the competition of the Kerr effect and plasma defocusing, there is a long filament formed. Ionization of nitrogen is almost negligible with respect to ionization of oxygen since there is a departure of

two decades in their respective contribution to the total electron density. Similar (2+1)D simulation results that show the space-time reshaping of infrared laser pulses undergoing filamentation in air also can be found in several publications [Kandidov 1997, Lange 1998, Chiron 1999]. These results generically show the importance of a specific physical effect which can change the overall stability of the generated filament or some features such as the periodicity of the refocusing cycles but not the general scenario.

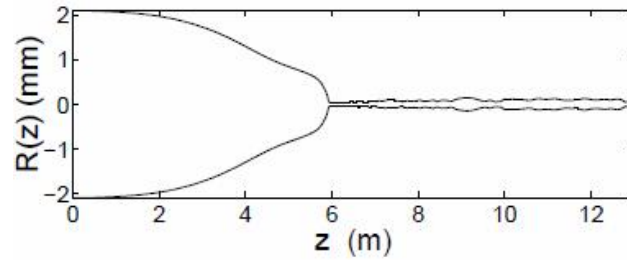
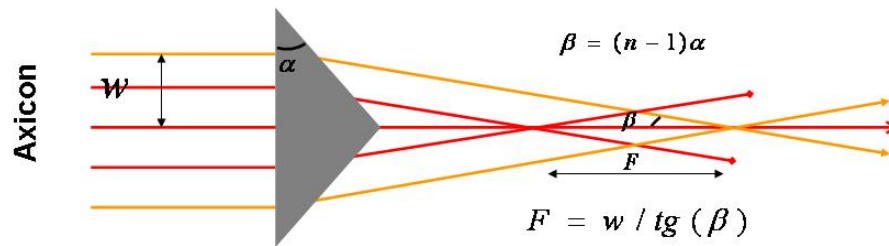
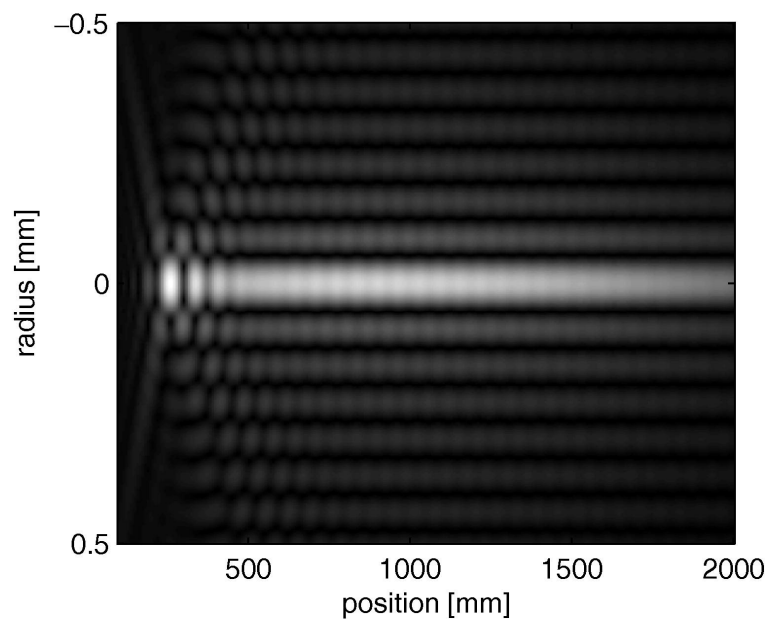


Figure 1.2: Evolution of the laser beam width along the propagation direction.



Chapter 2: Femtosecond laser induced plasma channel formed with an axicon



Femtosecond laser induced plasma channel formed with an axicon

Contents

2.1	Properties of an axicon in the linear regime	11
2.1.1	Introduction	11
2.1.2	Comparison of intensity profiles between an ideal and a real axicon	12
2.1.3	Comparison between experiments and simulations	14
2.2	Properties of an axicon in the nonlinear regime	18
2.2.1	The formation of a long plasma channel by a lens and an axicon	19
2.2.2	Simulation of Bessel beams generated plasma channel	24
2.2.3	Discussion on laser propagation with an axicon	27
2.3	Conclusion	27

The laser filamentation generated with the conventional spherical lens has been studied intensively, but it is difficult to generate in laboratory a long filament at a short distance from the laser. This requires the use of a converging beam geometry. In this chapter, I introduce a conical lens (also named axicon), through which the laser beam becomes diffraction-free. First I studied the linear propagation of the laser pulse after an axicon. Then, I experimentally observed the formation of a filament using an axicon. Finally the filaments formed with an axicon and a conventional lens will be compared.

2.1 Properties of an axicon in the linear regime

2.1.1 Introduction

Axicons have found an increasing use in optical applications, since their invention by McLeod [McLeod 1954]. Laser beams propagating through axicons have mainly two significant properties. First, they generate a line focus, where the on-axis intensity stays high over distances much longer compared to conventional lenses. Second, they generate ring-like profiles in the far field. Both of these properties proved useful in many applications. The long focal region, for example, is used to increase the depth range in optical coherence tomography [Ding 2002], as well as to guide

atoms as optical tweezers [Garces-Chavez 2002]. The ring profile in the far field is exploited to machine precision holes at an increased speed [Rioux 1978], and to trap atoms in the dark central region [Manek 1998]. The high on-axis intensities obtained around the focal region makes the axicons attractive for nonlinear optical application, where increased interactions lengths are desired, such as to generate long laser-induced plasma channels [Durfee 1993], and to study nonlinear propagation in air [Johannisson 2003].

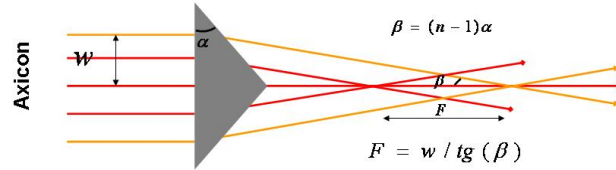


Figure 2.1: An ideal axicon.

Ideally, the effect of an axicon on an incoming beam is simply to introduce angularly symmetric and radially linear phase retardation (see Figure 2.1). If plane waves are incident on the axicon, they form a radial irradiance profile, described by zeroth-order Bessel functions [Herman 1991], forming "non-diffracting beams". Such waves, however, possess infinite energy, and hence are unrealistic. This problem can be resolved by using Gaussian input beam profile, which yield Bessel-like radial intensity profile, and a long transverse region where the beam intensity stays nearly constant. The radial position where maximum intensity occurs can be defined as the focal length of the axicon. Some distance after the focus, the beam forms a ring and propagates in this form henceforth.

2.1.2 Comparison of intensity profiles between an ideal and a real axicon

While the descriptions above yield smooth on-axis intensity profiles, practical issues cause some deviations from these expectations. Tanaka *et al.*, for example, calculated effects of the coma and astigmatism in case of axicons [Tanaka 2000]. The effect of a hard aperture at the edges and a stopper in the center was also studied theoretically in the case of plane waves [Jaroszewicz 1993], where the aperture was shown to cause oscillations in the on-axis intensity, and a beam stopper in the center can be used to minimize these oscillations. Apart from aberrations resulting from misalignments and diffraction effects from hard edges, there is also a very important practical consideration, regarding the center of the axicon; an ideal axicon would have a perfectly flat face with a sharp point tip. This, however, is practically impossible to realize, and the tip of the axicon is blunt, in reality. Depret *et al.* have shown that the blunt tip region of an axicon can be described by a hyperbola [Depret 2002]. They have analyzed the beam profile in the far field, where rings are formed, and shown that the bluntness causes non-zero central regions.

2.1.2.1 Theoretical modeling

We calculate the electric field distributions of light after an axicon, using Fresnel-Kirchoff integral. The input beam is assumed to be Gaussian. The system possesses cylindrical symmetry, hence the field will have only r and z dependence. In cylindrical coordinates, the Fresnel-Kirchoff integral can be written as

$$E(r_1, z) = \frac{1}{i\lambda z} \exp\left(ikz + \frac{r_1^2}{2z}\right) \int_0^\infty \exp\left(\frac{ik}{2z}r_0^2\right) J_0(kr_0r_1/z) E(r_0)r_0 dr_0, \quad (2.1)$$

where $E(r_1, z)$ is the light electric field at longitudinal position z and radius r_1 , $E(r_0)$ is the input field (including the phase change due to axicon), k is the wave vector, λ is the wavelength and J_0 is the zeroth-order Bessel function. The input field can be written as:

$$E(r_0) = \exp\left(-\frac{r_0^2}{w_0^2} - ik\frac{r_0^2}{2R}\right) \exp(i\phi_{axicon}), \quad (2.2)$$

where R is the radius of the curvature and ϕ_{axicon} is the phase retardation introduced by the axicon.

To take into account the bluntness of the axicon, we use a hyperbolic profile around $r = 0$, as described in [Depret 2002]. The hyperbola gives a good approximation of a practical axicon tip since it gives a flat face at $r = 0$, and asymptotically approaches the linear profile for larger r . We also show later that this approximation also gives very good match with the experimental results. We define a radius r_{hyp} , over which the axicon thickness is hyperbolic. As a result, the thickness of the axicon will be given by

$$d(r) = c_1 - R_{hyp} \tan^2(\gamma) \sqrt{1 + \frac{r^2}{R_{hyp}^2 \tan^2(\gamma)}} \quad \text{for} \quad r \leq r_{hyp}, \quad (2.3)$$

$$d(r) = c_2 - r \tan^2(\gamma) \quad \text{for} \quad r \geq r_{hyp}, \quad (2.4)$$

where R_{hyp} is the curvature of the hyperbola, γ is the axicon base angle, c_1 is a constant used to match the two profiles at $r = r_{hyp}$, and c_2 is a constant determined by the actual size of the axicon. The relative thicknesses of the axicon for ideal and blunt cases are shown in Fig 2.2, using experimentally determined values (see below). The corresponding phase retardation is then (after dropping constant phase factors):

$$\phi_{axicon}(r) = kd(r)(n - 1), \quad (2.5)$$

where n is the index of refraction of the axicon material.

Eq.(2.3) has two parameters that need to be determined: r_{hyp} and R_{hyp} . Whereas both can be used as fit parameters to find the best match between calculations and experiments, we show below that it is possible to directly measure R_{hyp} , leaving a single fit parameter.

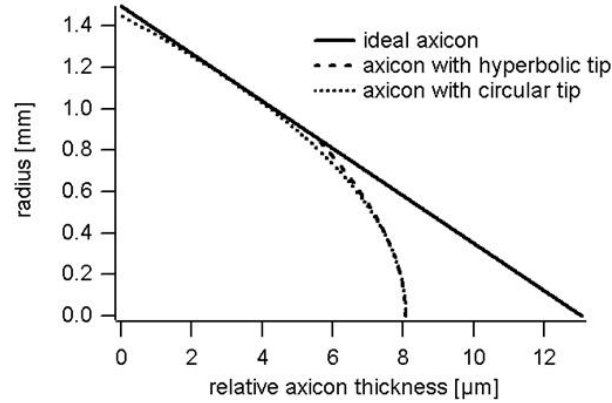


Figure 2.2: The relative thickness of axicon around the center for ideal (solid line), hyperbolic - as given in Eq. (2.3)- (dashed line), and circular -with radius R_{hyp} - (dotted line) profiles. The values, $r_{hyp} = 0.86$ mm and $R_{hyp} = 130$ mm are determined experimentally by fitting the calculated and measured on-axis intensities.

2.1.3 Comparison between experiments and simulations

To compare the calculations with the experiment, we used an axicon with a base angle of 0.5 degree, made of BK7 glass. We used a He-Ne laser as a light source, which had a spot size of $w_0 = 0.45$ mm. To do experiments with larger beam sizes, the beam is expanded around five times using a telescope. We measured the transverse intensity profile on a CCD (UEye 2210M) at 10 mm intervals. For each transverse profile, the on-axis intensity was extracted.

Figure 2.3 shows the measured on-axis intensity profile after the axicon with an unexpanded beam (solid line). Comparing this with calculations for an ideal axicon (dashed line) shows a dramatic difference, with the ideal focal distance being about four times shorter. On the other hand, when we use the profile described by Eq.(2.3), we obtain a very close match for the values, $r_{hyp} = 0.86$ mm and $R_{hyp} = 130$ mm.

The dramatic effect shown in figure 2.3 indicates that the bluntness of the axicon cannot be ignored, even though it affects only a small portion ($r < 0.85$ mm) of the element. In fact, from figure 2.2, it is evident that in the blunt region, the axicon profile is closely matched by a circle. This indicates that, in this region, the axicon acts much more like a conventional lens. Therefore, if the input beam size is comparable to the blunt region, the axicon acts just like a plano-convex lens. One can easily calculate the focal length of such lens using lens maker's formula [Hecht 1998]:

$$\frac{1}{f} = (n - 1) \left(\frac{1}{R_1} - \frac{1}{R_2} \right), \quad (2.6)$$

R_1 and R_2 being the radii of curvature of output and input surfaces respectively, n the index of refraction of the lens material and f the focal length. In our case, since the input face is flat and $n \approx 1.5$, the focal length becomes $f \approx 2R_1 = 260$ mm.

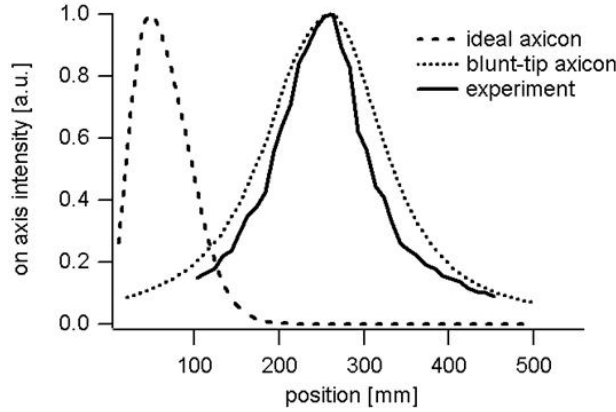


Figure 2.3: Measured on-axis intensity for $w_0 = 0.45$ mm (solid line), calculated on-axis intensity for ideal (dashed line) and blunt-tip (dotted line) axicons.

This yields a very good match with our calculated and measured intensity profiles, where the maximum intensity occurs at 258 mm.

This argument is further justified by examining the transverse intensity profiles at different positions. An ideal axicon would yield Bessel-like radial profile around the focal region, and an annular profile in the far field. The measured profiles in figure 2.4 show that neither of these happens and the measured profiles exhibit mere Gaussian beam diffraction.

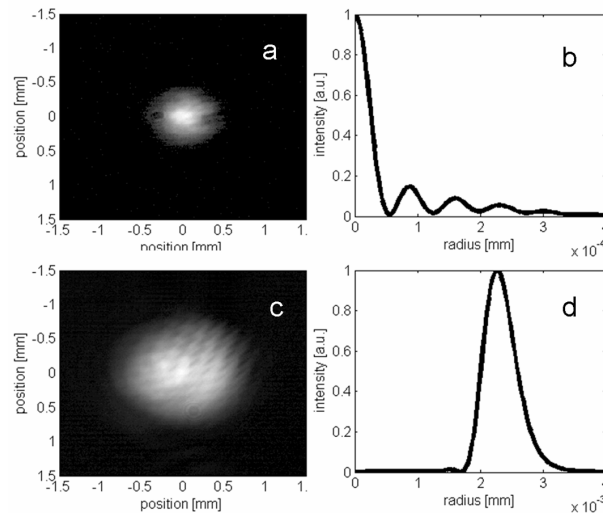


Figure 2.4: Measured transverse intensity profile and calculated radial profile for an ideal axicon at $z = 100$ mm (a-b) and at $z = 600$ mm (c-d). Square root of measured profiles is taken for better clarity. Note that the measured profiles show no trace of the effect of axicon.

Our observation that the axicon behaves like a lens at the tip shows that the

two free parameters in Eq.(2.3) reduce to one, namely, since R_{hyp} can be directly measured using the method prescribed above.

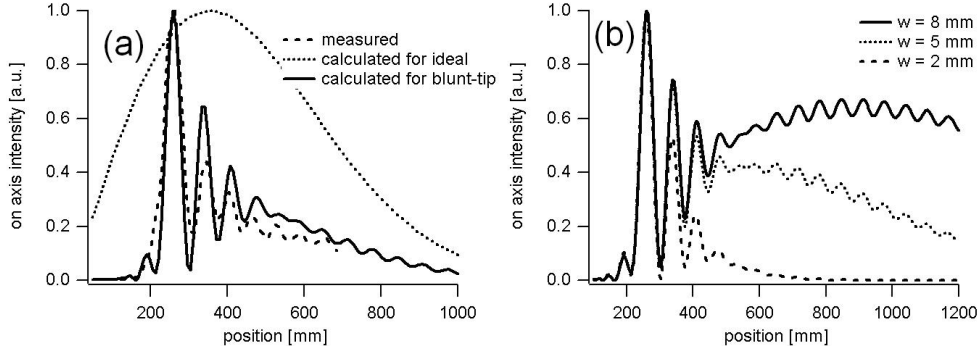


Figure 2.5: (a) Measured and calculated on-axis intensity profiles for input beam size $w_0 = 3.2$ mm; (b) Calculated on-axis intensity profiles for different input beam sizes. Note the two principal maxima for $w_0 = 8$ mm.

So far, we have shown simulations and measurements with a beam, which has the size comparable to the blunt region of the axicon. In order to further verify our finding and examine the effects for larger beams, we expanded the beam and repeated the measurements. Figure 2.5(a) shows the measured and calculated on-axis intensity profiles for an input beam size $w_0 = 3.2$ mm. From the figure, the dramatic effect of the axicon tip is evident. The measured profile matches very closely the calculated profile for blunt-tip with the same parameters mentioned above. The ideal axicon yields a profile significantly different. Figure 2.5(a) also shows that, when the input beam is larger than the blunt region, the on axis intensity exhibits strong oscillations. They are due to the interference from waves emerging from the lens-like center, and axicon surroundings. Figure 2.5(b) shows calculated on-axis intensity profiles for different beam sizes. The oscillations are present in all cases. It is interesting to note that, there is always a principal maximum, at the position, given by the effective focal length of the lens-like blunt region, defined above. For larger beams, a secondary peak (envelope of faster oscillations) appears at the position of the focal length of an ideal axicon, with the same base angle. The focal length of an ideal axicon is where on-axis intensity reaches its maximum, and it is given by (for small base angles):

$$f_{axicon} = \frac{w}{2\alpha(n-1)}. \quad (2.7)$$

For $w_0 = 5$ mm Eq.2.7 yields axicon $f = 560$ mm and for $w_0 = 8$ mm yields $f = 890$ mm. Note that these values match the secondary maxima in the calculated profiles.

We have shown so far that the intensity distribution after an axicon is dramatically modified by the bluntness of its tip. The on-axis intensity exhibits oscillations and the radial profile is not Bessel-like. We finish this section by showing our calculations of full $r - z$ profile of a beam, passing through a real axicon. Figure 2.6

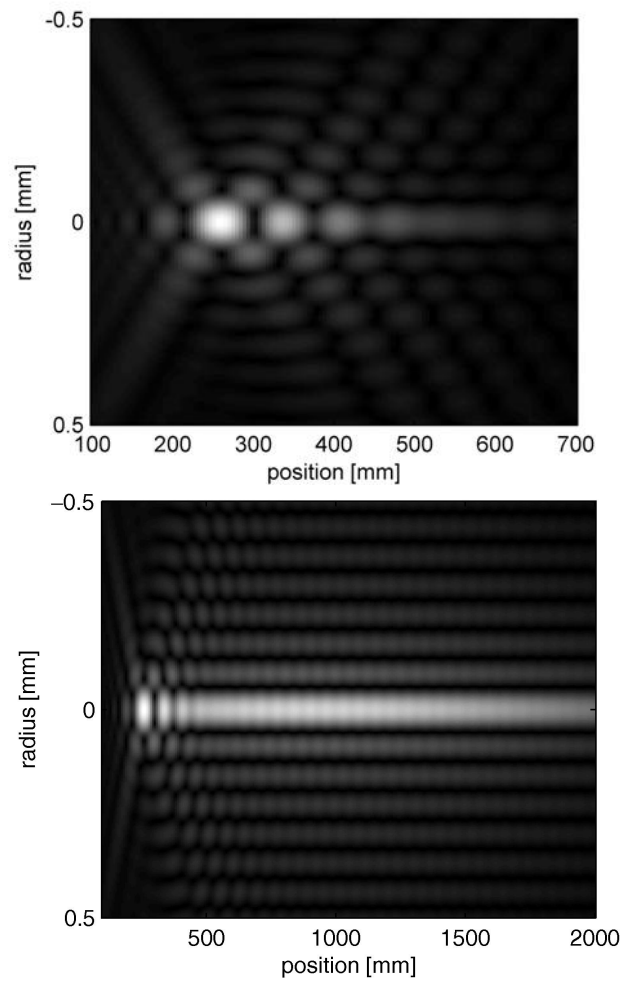


Figure 2.6: calculated full intensity profiles for $w_0 = 2$ mm (Top) $w_0 = 8$ mm (Bottom), for a real axicon. Square root of the light intensity is taken for clarity of low-intensity parts.

shows the calculated radial-transverse profile for the real axicon parameters above and with input beam size $w_0 = 2$ mm and $w_0 = 8$ mm respectively.

The results above show that for a real axicon, the on axis-intensity is not smooth but rather oscillating. These oscillations can be unwanted and biasing for applications of axicons. As a result, in this section, we propose ways to reduce these oscillations and smooth the intensity profile. Since the source of the oscillations is mainly interference from the center and surroundings, the first method we propose is to put a beam stop in the center of the axicon, the radius of which is comparable to the r_{hyp} . We measured the on axis intensity using the setup described above, with an addition of a beam stop (radius of 1 mm) at the center of the axicon. Figure 2.7 shows the measured and calculated intensities with the beam stop. The oscillations are reduced significantly, while the remaining ones are due to the diffraction from the hard edge of the beam stopper. The beam stopper causes some loss of energy, which in this case is about 10 percent.

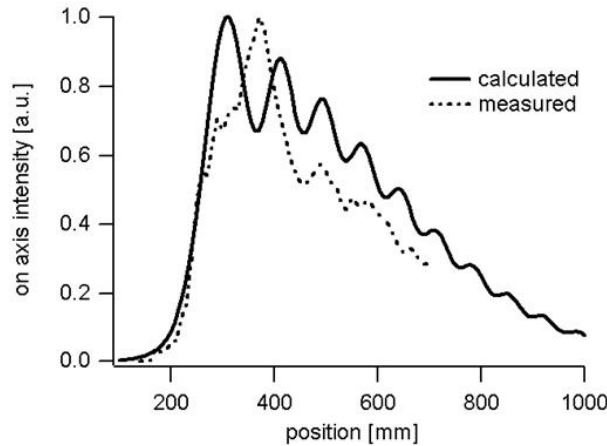


Figure 2.7: Calculated and measured on-axis intensity for a real axicon, with a 1 mm radius beam block at the center. The input beam size is $w_0 = 3.2$ mm.

In the section above, we have studied the intensity distribution of light passing through a real axicon. The bluntness of the tip causes significant deviations from an ideal case. The on-axis intensity distribution is strongly dependent on the beam size. For small beams, the real axicon acts like a regular lens, while for large ones, it exhibits two principal peaks, one coming from the lens-like center, and the other coming from the axicon. The overall profile shows strong oscillations. By blocking the center part of the axicon, the oscillations can be reduced, at the cost of some energy loss. These linear studies proved that through an axicon, a high and uniform on-axis intensity distribution can be generated over long distance, this unique property would be crucial for forming a longer plasma channel in transparent media.

2.2 Properties of an axicon in the nonlinear regime

Nonlinear optical propagation of laser pulses in media generates a broad range of light-matter interactions [Boyd 2003]. In most of these phenomena, the effective interaction length, i.e. the region over which the laser intensity stays high, plays a crucial role in determining the magnitude of the effect. For typical Gaussian laser beams focused by conventional lenses, the high intensity region is given by the Rayleigh length, which is proportional to the square of the beam waist size. As a result of the fixed power in the beam, the highest focused intensities correspond to the smallest Rayleigh lengths. This limitation can be relaxed by using waveguides, where the beam size is kept constant by using tailored refractive index structures. For high-power laser pulses, the intensity dependent refractive index may serve as a self-guiding mechanism, leading to long range, high intensity propagation, which is commonly known as optical filamentation [Couairon 2007]. At the intensity levels involved during filamentation, nonlinear absorption and ionization become significant effects, causing the generation of accompanying plasma, which also contributes to the propagation dynamics. The relatively long high intensity region during filamentation was foreseen to be very useful for many nonlinear optical applications ranging from pulse compression [Zair 2007] to LIDAR [Kasparian 2001, Kasparian 2003].

2.2.1 The formation of a long plasma channel by a lens and an axicon

The non-diffracting Bessel beams can retain high laser intensities over long distances [Durnin 1987]. Such beams can have sharp transverse intensity profiles within several wavelengths, independent of propagation distance. Unfortunately, ideal Bessel-beams are practically impossible to generate as they carry an infinite amount of energy. Nevertheless, approximations to the ideal case are possible. Gaussian beams focused by an axicon [McLeod 1954, McLeod 50], for example, generate Bessel-like beams, where the on-axis intensity stays high and changes slowly over relatively long distances, particularly when compared to focusing with conventional lenses. With sufficiently high input powers, the axicon-generated beams also become attractive for nonlinear optical applications. Several groups have studied the propagation of high-power ultrashort laser pulses focused by an axicon, in presence of third order nonlinearities including the optical Kerr effect [Johannisson 2003, Pyragaitė 2006, Roskey 2007, Polesana 2006] and three-photon absorption [Polesana 2002]. A particularly interesting consequence of using an axicon is the possibility of generation of long plasma channels in gases, including air, through multi-photon absorption (MPA). Durfee and Milchberg [Durfee 1993] used an axicon to form laser-generated plasma in argon, which then served as a waveguide for another laser beam. More recently, Roskey *et al.* [Roskey 2007] have theoretically studied nonlinear propagation of axicon-focused beams in air, and predicted that underdense plasma channels may accompany the beams. Polesana *et al.* have investigated Bessel filaments, formed by focusing laser beams with an axicon in air

and in condensed media. They obtained two different nonlinear regimes in which the filament takes the form of a stationary nonlinear Bessel beam identified as a nonlinear unbalanced Bessel beam [Porrás 2004]. The latter can be stable with clamped intensity, or unstable and propagate in an oscillatory regime leading to conical emission [Polesana 2007]. MPA plays a dominant role in establishing the stationary Bessel filaments; both the stable and unstable situations can be accompanied by plasma generation although in principle, the effect of plasma defocusing itself does not prevail in clamping the intensity in Bessel filaments.

In this part, I will present our experimental work on nonlinear propagation and generation of plasma channels in air by using axicon-focused ultrashort laser pulses. We have developed a method to detect the presence of the laser-generated plasma. The method is based on plasma screening of external electric field and it has sufficient longitudinal spatial resolution to investigate fine structure. We observe plasma channels as long as ~ 1 m using 8 mJ input pulse energy and ~ 3.5 m using 90 mJ input pulse energy. The plasma channels exhibit oscillations in the longitudinal direction, which are reminiscent of those present even in the linear propagation regime and originate from the bluntness of a real axicon as shown in the former section.

2.2.1.1 Experimental scheme for generating a longer plasma channel

The experimental scheme that we used is illustrated in figure 2.8. We have used two different Ti:Sapphire oscillator-amplifier chains. The first system has maximum pulse energy of 15 mJ, pulse duration of 40 fs and repetition rate of 100 Hz (**Thales** alpha 100). The second system has maximum pulse energy of 200 mJ, pulse duration of 150 fs and repetition rate of 10 Hz (**Teramobile**). Some portions of the outputs of these lasers were focused in air, by using an axicon. The axicon has 0.5 degrees base angle and is made of BK7 glass. In order to verify the presence of plasma generated by this scheme, we have developed a detection system shown in figure 2.8. We pass the beam between two square (with 2 mm sides) metal electrodes and apply high voltage ($V \sim 1$ kV) between them. The plate separation is 5 mm. One of the plates is connected to a resistor ($R \sim 1\text{M}\Omega$) and then grounded. The potential drop across the resistor is measured using an oscilloscope. A slit aperture is placed in front of the electrodes to avoid laser light directly hitting them, thereby causing parasitic photocurrent. The size of the electrodes determines the longitudinal spatial resolution of the detection, and is sufficient to resolve the structure in our experiments, as will be shown below. The detection system is placed on a translation stage, so that the measurement can be made at different positions along the laser propagation direction.

Vujicic *et al.* have used a scheme for measuring the plasma density, where they have applied a potential difference on probes along the laser direction and modeled the plasma as a time-dependent resistor [Vujicic 2006]. This method lacks the spatial resolution to investigate the changes in the laser direction. Another similar detection system was used by Eisenmann *et al.*, to investigate fine structure of laser-induced

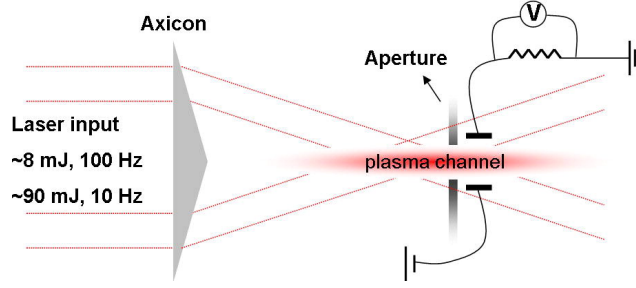


Figure 2.8: Setup used to detect plasma channels generated by axicon-focusing.

plasma channels in air [Eisenmann 2007]. They have used two electrodes with the laser passing in between (as in our case), and measured the change in the breakdown voltage in air in the presence of plasma to infer the plasma density. In this work, we operate at voltage levels much lower than breakdown in air. Our detection is rather based on the screening property of the plasma. In the presence of an external electric field, the charges in the plasma redistribute and screen out the external field [Chen 2006]. The new charge distribution generates a potential on the grounded plate, which in turn causes a current to flow from the resistor. As a result, by measuring the potential drop, hence the current through the resistor at different position along the laser propagation direction, we can have a mapping of the plasma density.

2.2.1.2 The probing method for laser induced plasma detection

The probe that we use to measure the potential drop has a capacitance of 11 pF and resistance of 10M Ω . This probe is connected to an oscilloscope, which itself has an input impedance of 1M Ω and capacitance of 15 pF. As a result, the circuit response time is much slower than the lifetime of femtosecond laser-generated plasma (order of a few nanoseconds [Couairon 2007]), hence, our detector acts as an integrator over time. Since the laser-induced plasma channel possesses cylindrical symmetry, and is a good conductor, the screening of the applied constant electric field generates a surface charge distribution in the form $\sigma(\phi) = \sigma_0(\phi)$, where σ is the surface charge density and ϕ is the azimuthal angle in the cylindrical coordinates [Gaižauskas 2006]. This charge distribution causes a change in the potential on the grounded plate. We assume that the surface charge density, hence the induced potential on the probed plate, follows the same temporal decay as the volume charge density, i.e.

$$\rho_e(t) = \frac{\rho_e(0)\exp(-\eta t)}{1 + \rho_e(0)\beta_{ep}t}, \quad (2.8)$$

where $\rho_e(t)$ is the volume charge density, η is the decay coefficient for electron attachment to oxygen and β_{ep} is the electron-ion recombination rate. Using experimentally measured values of $\eta = 2.45 \times 10^7 \text{ s}^{-1}$ and $\beta_{ep} = 2.2 \times 10^{-7} \text{ cm}^3/\text{s}$ along with Eq. 2.8 and calculated temporal response of our circuit, we calculated the maximum of current measured with the oscilloscope as a function of the plasma density. Figure

2.9 shows that, for electron densities between 10^{15} and 10^{17}cm^{-3} , the peak current changes linearly with the electron density. This density regime covers the values indicated by our simulation, as will be shown below. As a result, we can use the measured current to extract the relative changes in the electron density.

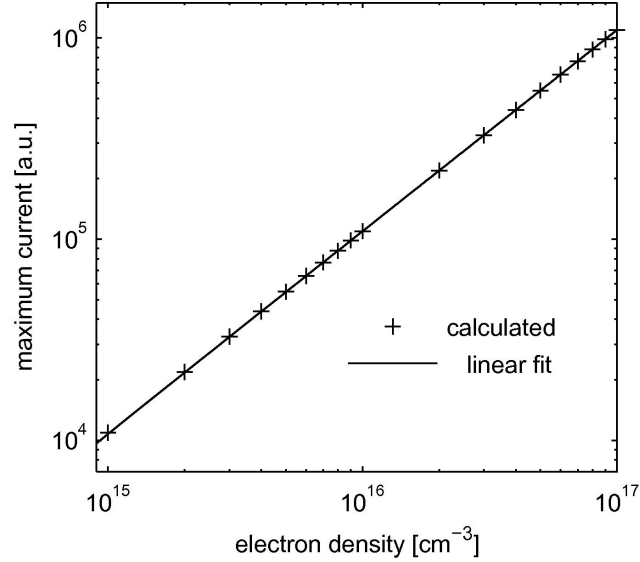


Figure 2.9: Calculated maximum current as a function of electron density using Eq. (2.8) and the temporal response of the circuit used in the experiment. The fit is made in linear-scale and displayed in log-log scale.

2.2.1.3 A longer plasma channel formed in air

Figure 2.10 shows the measured current (normalized) in the experiments, as a function of the transverse position. For this data set, the 100 Hz laser described above was used, with the output energy of 8 mJ. The input beam size is 8.2 mm (at $1/e^2$ of the intensity). Plasma channels were formed in air using an axicon, and for comparison using a conventional lens (1 m focal length). The current is measured at 2 mm intervals. It is apparent that the axicon generates a much longer plasma channel. The overall length of the plasma generated by the axicon exceeds 1m, while that formed by the lens is around 0.1 m. In the case of axicon, the corresponding on-axis intensity is estimated to be of the order 10^{13}W/cm^2 and plasma density to be 10^{16}cm^{-3} , from the solutions of nonlinear Schrödinger equation, which are presented in the next section.

The measurements of the current in figure 2.10 also show that, in the case of axicon, there are significant oscillations in the plasma density. Roskey *et al.* have shown that self focusing may cause some oscillations in the on-axis intensity profile [Roskey 2007]; Polesana *et al.* have shown that oscillations can arise either in a weakly nonlinear or in a fully nonlinear but unsteady Bessel filamentation regime [Polesana 2008]. Here, we identified the oscillations that we observed as

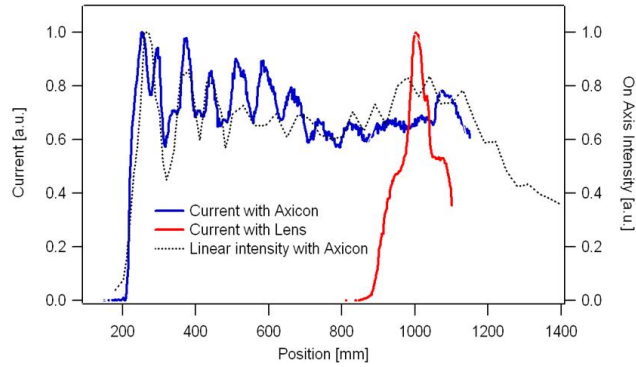


Figure 2.10: Normalized current through the resistor in the case of the axicon and 1 m focal length lens, using 8 mJ input pulse energy -left y-axis- and normalized on axis intensity in the linear regime -right y axis-.

mainly due to the linear evolution of the pulse field after the non-ideal axicon. To reconfirm, we have measured the on-axis intensity after the axicon by reducing the laser energy and measuring the beam profile on a CCD at different positions after the axicon. The right y-axis in figure 2.10 shows the measured linear on-axis intensity. It is evident that the measured plasma-induced current profile in the nonlinear propagation regime is primarily governed by the linear intensity profile. These oscillations in the intensity profile are due to the deviation of the shape of the axicon from ideal in its center region: the tip of the axicon is practically not infinitesimally sharp, but rather blunt. This causes significant deviations on the on-axis intensity profile, including the oscillations as we observed. The details of the considerations on real axicons can be found elsewhere [Depret 2002, Akturk 2008b].

We have performed similar experiments using a higher power laser system. We used the **Teramobile** system described above, with output power of 90 mJ. The transverse beam profile is nearly flat-top with full width at half maximum of 34 mm. The current is measured at 10 cm intervals. Figure 2.11 shows the measured current using our detection system, from which we can infer the presence of a plasma channel over about 3.5 m. The plasma profile in this case is smoother compared to figure 2.10, since the beam is larger, hence the blunt tip region of the axicon affects a relatively smaller portion of the beam.

2.2.2 Simulation of Bessel beams generated plasma channel

The experimental results presented in the previous section show that axicon-focused high power laser beams can generate relatively long plasma channels in air. The detection method we employed allows us to resolve the oscillation in the plasma density in the longitudinal direction. While the measured current yields a good approximation to relative changes in the electron density, the absolute value of the plasma density is rather difficult to extract directly from the measurements.

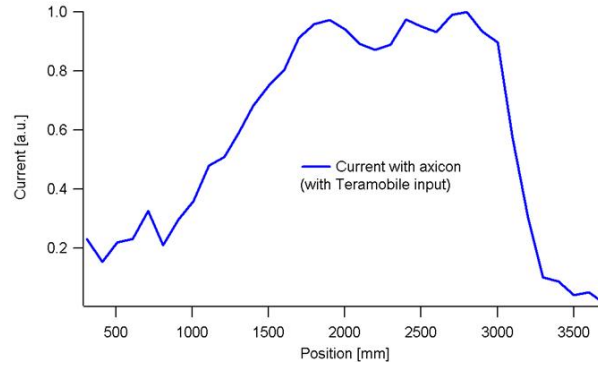


Figure 2.11: Normalized current through the resistor in the case of the axicon using 90 mJ input pulse energy.

2.2.2.1 Simulation of Nonlinear pulse propagation with an axicon

In order to have more quantitative analysis, we have performed numerical simulations of the nonlinear propagation involved in our experiments in air. The NLSE equation is solved using a Crank Nicholson scheme applied to each frequency [Couairon 2007]. The input electric field is constructed using the measured pulse and beam parameters. The axicon-focusing is modeled by a phase function, taking into account the real shape of the axicon including the blunt tip. Due to the cylindrical symmetry of the axicon and the input beam, we could perform the simulations in two spatial coordinates and time. As shown by Polesana *et al.* even in the presence of inhomogeneities in the input beam, the axicon forces the symmetry to be restored [Polesana 2002].

Figure 2.12 shows simulated on-axis intensities and electron densities generated by axicon focusing, at different input pulse energies. For Figure 2.12 the input pulse energy is 1 mJ (other parameters reflect the 100 Hz system described above). It shows the intensity profile closely following the linear case, with minimal contribution from the plasma, which has density around 10^{13} cm^{-3} over the whole propagation distance (Figure 2.12-bottom). The on-axis intensity is around 10^{13} W/cm^2 . The simulations allow us to separate the relative contributions of plasma defocusing and self-focusing to the propagation dynamics, by switching off the ionization; we observe that the small deviation from the linear case is mainly due to self-focusing, as can be seen from the calculations where ionization is switched off.

2.2.2.2 Optimization of Bessel beam induced plasma channel length

Above, in the linear case (Figure 2.4), we showed that, for the beam with larger diameter, after an axicon the on axis-intensity can be higher, and keeps constant over a longer distance. Consequently, if the intensity is sufficient to ionize air, with larger diameter, the Bessel beam can generate a longer plasma channel. In the experiment (see Figure 2.10 and Figure 2.11), we experimentally verified that with large pulse energy, the larger-diameter beam can form a longer and less modulated

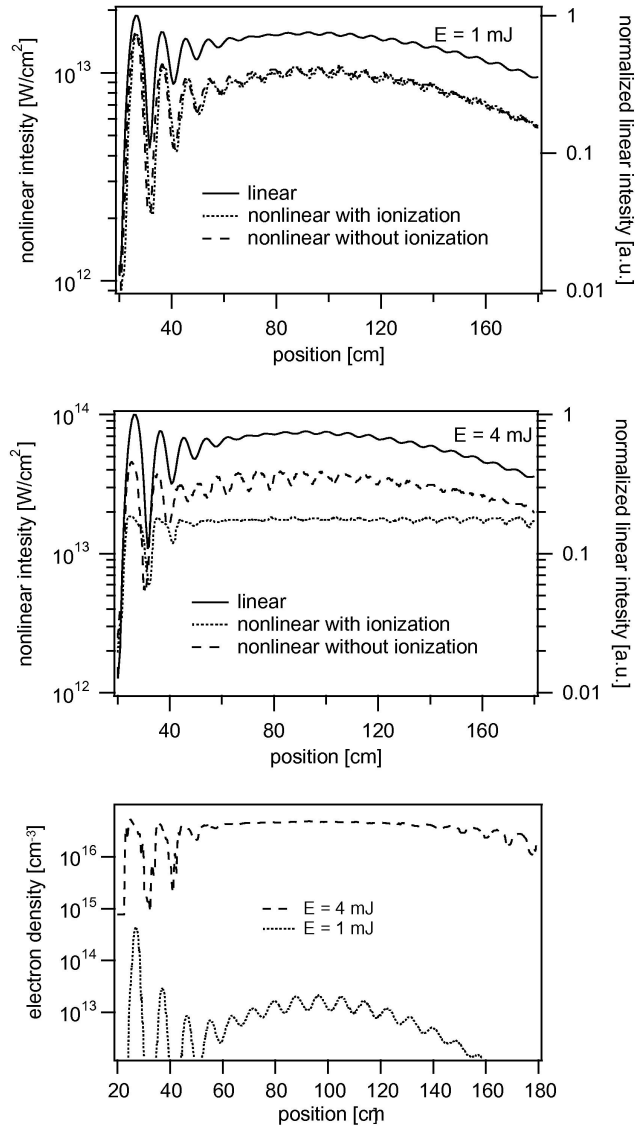


Figure 2.12: Top: On axis intensity profiles using a real axicon for 1 mJ input pulse energy (other parameters same as the experiment described above). Solid line: normalized linear intensity (right y-axis), dotted line: nonlinear intensity including ionization (left y-axis), dashed line: nonlinear intensity without ionization (left y-axis). Center: Same as the top figure, with the input pulse energy increased to 4 mJ. Bottom: electron densities for 1 mJ and 4 mJ input pulse energies.

plasma channel. With the simulation, based on the NLSE equations, we simulated the Bessel plasma channel formed by the 15 mJ, 50 fs, central frequency at 800 nm laser pulses with the beam diameters $D = 20$ mm and $D = 10$ mm respectively.

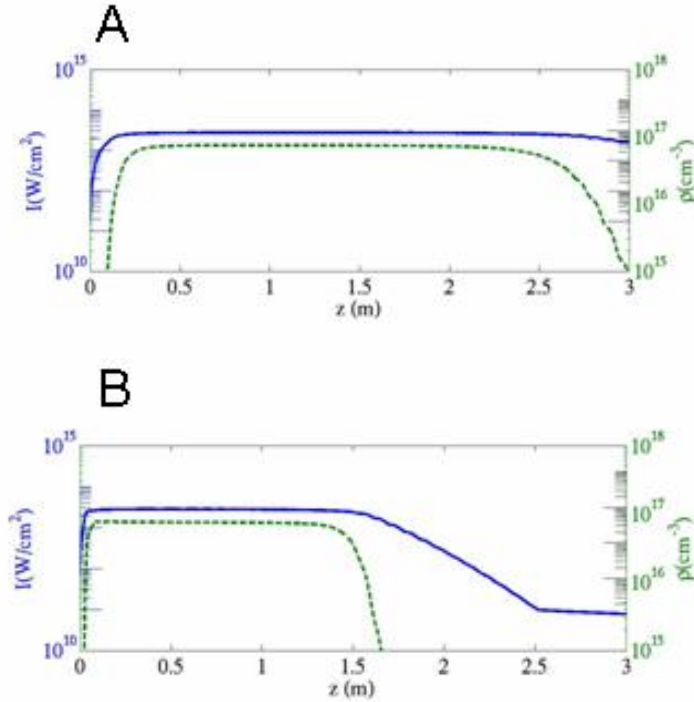


Figure 2.13: Electron density of Bessel beam formed plasma channel (green line). A: initial beam diameter of 20 mm. B: initial beam diameter of 10 mm. For both cases, the base angle of the axicon is 0.5 degree. The simulation is performed with the code of A. Couairon.

From Figure 2.13, we can see that the beam with 20 mm diameter generated nearly twice longer plasma channel. In both case, because of the intensity clamping, the electron densities are roughly the same. The simulation proved that compared with high intensity of the laser beam, the initial beam size plays a more critical role to create a longer Bessel plasma channel.

2.2.3 Discussion on laser propagation with an axicon

In order to understand the propagation dynamics of laser pulses focused by an axicon, it is crucial to distinguish contributions from different effects. It was predicted before that the Kerr effect causes oscillations in the intensity profile [Roskey 2007, Gadonas 2001]. More generally, strong nonlinear effects may cause an instability leading to interferences between the axial and conical emissions [Gaižauskas 2006, Polesana 2008]. However, as we show here, in practical cases, the bluntness of real axicons may cause stronger oscillations, mixing linear propa-

gation with strongly nonlinear effects. In Figure 2.12-top, it can be seen that the oscillations in the on-axis intensity in the nonlinear cases follow closely the linear case, with a slightly increased contrast caused by self focusing.

Regularization of the intensity profile is another important consideration. During nonlinear propagation of Gaussian beams, when the pulse possesses more than one critical power ($P_{cr} = 3.77\lambda^2/8\pi n_2$, λ being the laser center wavelength and n_2 the nonlinear index of refraction [Marburger 1975]), the beam would undergo collapse without any saturating mechanism. When the beam becomes sufficiently intense, plasma is generated and acts as a defocusing lens, thereby it constitutes a saturating mechanism leading to intensity clamping [Chin 2005]. However, multiphoton ionization is associated with MPA, which constitutes another saturating mechanism, due to the attenuation of the propagating pulse [Polyakov 2001]. In the case of axicon focusing, MPA prevails both in explaining the stationarity of Bessel filaments and the intensity clamping. We observed that intensity clamping with axicon focusing required more input power than that necessary with lens focusing, due to the annular nature of the propagating beam. Figure 2.14 shows the fraction of energy contained in the central peak in the cases of ideal and real axicons. In both cases, the center typically contains less than 4% of the total energy. As a result, the input power should be increased accordingly, so as to have significant contribution from MPA. This is consistent with our simulations; as shown in figure 2.12, when the energy is 1 mJ ($P \sim 6P_{cr}$, $P_{center} \sim 0.2P_{cr}$), the plasma has little contribution to the intensity profile, while for 4 mJ ($P = 30P_{cr}$, $P_{center} \sim 0.8P_{cr}$), the plasma density is a few orders of magnitude higher, indicating that a significant amount of energy is continuously absorbed by MPA, thus leading to intensity clamping. We can also infer that the axicon focusing may exhibit self-guided propagation (weakly nonlinear Bessel filaments) without significant contribution from plasma [Akturk 2007, Chiao 1964], if the fraction of the energy in the center lobe is much less than the critical power.

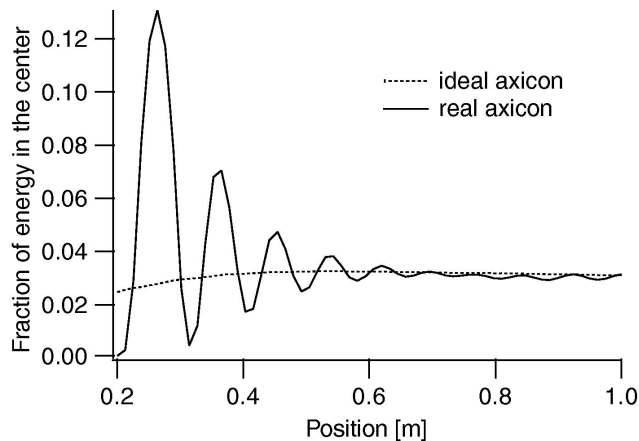


Figure 2.14: fraction of the transverse energy in the center peak for ideal and real axicon

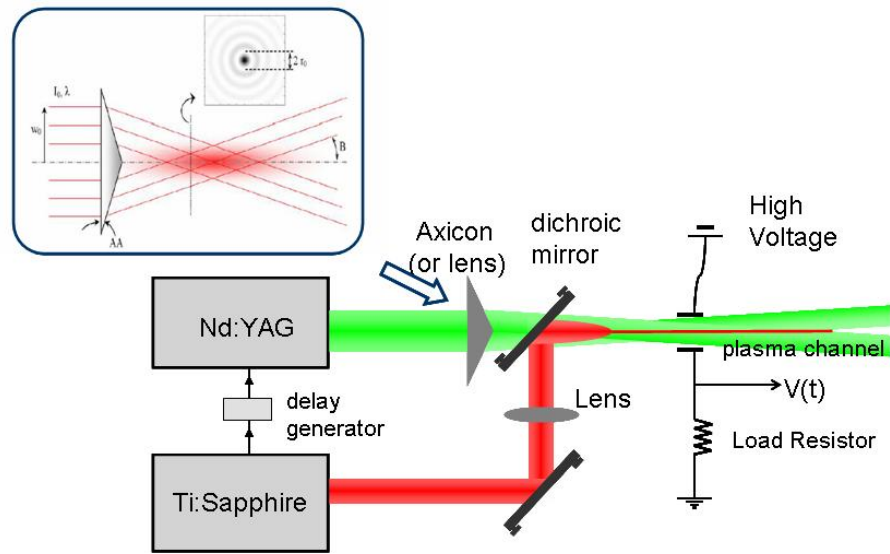
Table 2.1: Comparison of filaments in Laboratory

Filament type	Diffraction	Plasma Length	Electron density
With a conventional lens	yes	10 – 50 cm	$10^{16} - 10^{17} \text{ cm}^{-3}$
With an axicon	less	10 – 300 cm	$10^{13} - 10^{16} \text{ cm}^{-3}$

2.3 Conclusion

I have presented a theoretical and experimental study of the intensity distribution of a laser beam, after its propagation through a real axicon. It is surprising that, while an ideal axicon generates Bessel-like radial intensity profile and smooth on-axis intensity around the focal region, in practice, the bluntness of the tip of the axicon causes significant deviations from these profiles. In particular, strong oscillations occur on the on-axis intensity. The input beam size also plays a strong role; for small beams the axicon acts more like a conventional lens, while for the beam with a larger beam diameter, it exhibits two focal regions. A scheme for apodization has been also proposed to reduce real axicon induced oscillations. In all cases, the experiments match closely the calculations. Our results show that it is essential to take into account of the practical blunt profile of axicons for most applications.

Table 2.3 also shows the comparison of filaments with an axicon and a conventional lens in laboratory. By using an axicon, we can generate a longer plasma channel, but as the simulation shows, the electron density in the plasma channel strongly depends on the laser pulse energy, and varies from 10^{13} cm^{-3} to 10^{16} cm^{-3} . In contrast, although with a conventional lens, the plasma channel is much shorter, the electron density is one orders of magnitude larger than the one obtained with an axicon. Each method has its own advantage, and thereby one can chose the proper method according to the application.



Chapter 3: Femtosecond laser induced plasma channel: length extension and lifetime prolongation



Revival of femtosecond laser plasma filaments in air by a nanosecond laser

Contents

3.1	Temporal evolution of the plasma density and determination of plasma lifetime	31
3.2	Experimental methods to increase the plasma lifetime with a double pulse technique	32
3.3	Revival of femtosecond laser plasma filaments with another nanosecond laser	34
3.3.1	Simulation and Results of the plasma revival	34
3.3.2	Optical breakdown inside the plasma channel revived with two nanosecond lasers	37
3.3.3	Experimental evidence for the existence of N_4^+	37
3.4	Conclusion of plasma revival	40

When a filament is formed in the atmosphere due to recombination and attachment processes, the number of electrons drops off rapidly, thereby limiting the lifetime of the plasma channel to a few nanoseconds [Zhao 1995]. The short lived plasma poses a serious limitation in many applications. To resolve this major obstacle, we use a two beam technique to revive the plasma channel up to milliseconds after its disappearance. A first femtosecond laser pulse creates a filament, then a delayed nanosecond laser pulse will revive the plasma column long after the passage of the fs laser pulse.

3.1 Temporal evolution of the plasma density and determination of plasma lifetime

Several experiments have characterized the time evolution of free electrons' density in the wake of filaments [Schillinger 1999, Tzortzakis 1999, Ladouceur 2001]. For instance, by using time resolved diffraction method, in which the contrast of the fringes observed in far field is measured as a function of the delay between the

probe pulse and the self guided pulse, the plasma decay has been obtained (see Fig. 3.1.) [Tzortzakis 2000].

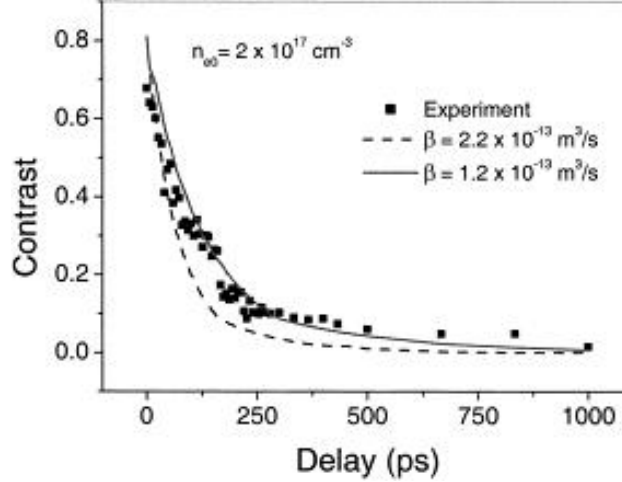


Figure 3.1: Optical contrast of the probe wave front central fringe as a function of delay. The dots are experimental results and the lines are simulations [Tzortzakis 2000].

In Figure 3.1, one can see two distinct phases with a rapid and a slow decay of the electron density. In the first phase, for a filament laser intensity of $5 \times 10^{13} \text{ W/cm}^2$, the initial free electron densities obtained in air reaches $10^{16} - 10^{17} \text{ cm}^{-3}$, mostly from multiphoton ionization of oxygen molecules of lower ionization potential (12 eV against 15 eV for N₂). At such densities electron recombination is dominated by the capture of the parent ions (see Eq. (3.1) below). This process leads to a decrease of the electron density by two orders of magnitude within a few nanoseconds (ns) [Ladouceur 2001]. Below 10^{14} cm^{-3} at delay $t = 220 \text{ ps}$, the capture by neutral oxygen molecules becomes the main recombination process. It gives rise to an exponential decay with a time constant $\sim 150 \text{ ns}$ in the second phase of the plasma evolution.

3.2 Experimental methods to increase the plasma lifetime with a double pulse technique

There have been several attempts to increase the filament plasma lifetime by using a second laser [Yang 2002, Hao 2005, Méjean 2006, Zhu 2006, Henis 2008, ?]. However, in all of these previous works, the plasma lifetime is increased at early times while free electrons are still present and the longitudinal extent of the effect is limited to the Rayleigh length of the focused nanosecond laser beam.

In this part, I will present what we believe is a significant progress in resolving the problem of obtaining a long-lived plasma channel. We demonstrate experimentally that it is possible to reestablish a conducting air column even milliseconds (ms) after

the passage of the fs pulse and to prolong its lifetime with the help of a second laser. The principle is to exploit the on-site storage of weakly bound electrons onto oxygen molecules following the formation of the original plasma channel [Zhao 1995]. The attached electrons provide a reservoir with a memory of the geometry of the filament over a time corresponding to the ion-ion recombination and diffusion of the negative oxygen molecules out of the initial filament core. This corresponds to times of the order of several ms. By using a Bessel-like ns duration laser beam to detach these electrons we show that it is possible to restore a plasma over a distance much longer than could be achieved with a conventional focusing system. In the present case, the restored plasma length is 50 cm, but it could be considerably extended with more powerful lasers. More importantly, the focused Bessel like beam has on-axis intensity sufficient not only to liberate the bound electrons, but also to multiply them through inverse bremsstrahlung and avalanche processes. We further show that by using a two-color scheme with sufficient pulse energies, the electron density in the revived plasma channel can even exceed the initial electron density from the femtosecond laser. The restored plasma channel lifetime lasts beyond one microsecond.

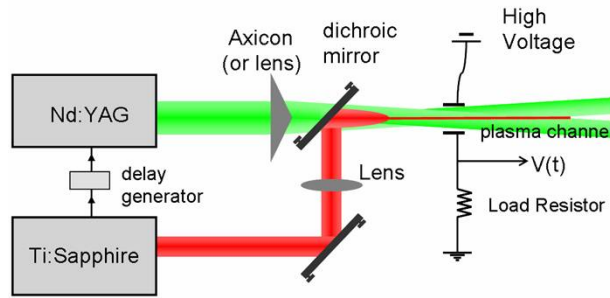


Figure 3.2: Experimental setup. The femtosecond laser generates the plasma channel and the delayed nanosecond laser revives it. The plasma channel is detected using electrodes with high voltage and/or a PMT (Photomultiplier tube)

The experimental setup is shown in Fig.3.2. The initial plasma channel was generated through the filamentation of fs laser pulses. We have used a Ti:Sapphire chirped pulse amplifier chain, which can provide up to 15 millijoules (mJ) pulse energy at a pulse duration of 50 fs (at 800 nm center wavelength) and the teramobile laser [Wille 2002] which can provide up to 250 mJ pulse energy at a pulse duration of 150 fs. To revive the plasma channels, we used a Nd:YAG laser at 1064 nm and/or its second harmonic at 532 nm, which can provide up to 250 mJ pulse energy at both wavelengths with a pulse duration of around 10 ns. The different laser systems were synchronized at 10 Hz repetition rate, with controllable delay between their pulses. The Nd:YAG laser was focused with an axicon (0.5 degree base angle, 5 cm diameter), which generated a Bessel-like transverse profile with a long focal region [Durnin 1987, Akturk 2008a]. The longitudinal focal range of the Bessel-like beam was about 50 cm with a central peak of 100 μm , which provides good longitudinal and transverse overlap with the filament. The fs laser beam was focused with a 75

cm focal length lens and aligned such that the filament overlapped with the axicon line focus. In order to detect the presence of plasma, we passed both beams between two square metal plates with ~ 5 kV voltage and 5 mm separation. To avoid the laser beams directly hitting the metal and generating photocurrent, the plates were covered with an insulator. In the presence of an external electric field, the charges in the plasma redistribute, screen out the external field [Chen 2006], modify the potential and generate a current through the grounded arm. The corresponding potential drop across the resistor was measured using an oscilloscope. We also used a photomultiplier tube (PMT) with a narrow interference filter centered at 338 nm (10 nm bandwidth) to detect the emission from excited N_2^* molecule fluorescence [Iwasaki 2003] (the detailed mechanic of fluorescence will be discussed later). The former method proved more sensitive in detecting low plasma densities, while the latter gives a faster temporal response.

3.3 Revival of femtosecond laser plasma filaments with another nanosecond laser

Figure 3.3(a) shows measurements of the revival of plasma channel generated by 90 mJ of the teramobile laser and reestablished by the Nd:YAG laser (at 532 nm) at 1 ms delay. The electrical method described above was used with a 1 M Ω load resistance in order to enhance detection sensitivity. Due to the circuit response the decays exhibited by the signals were slower than the actual plasma lifetime. The true plasma lifetime, obtained with a 50 Ω load resistance, is shown in the inset of Fig. 3.3(a). The first peak around $t = 0$ in Fig. 3.3(a) is caused by the filament plasma of the fs pulse. When the Nd:YAG beam focal axis was carefully aligned with the filament, we observed a second peak at the arrival time of this laser. The second peak disappeared when the detection system was enclosed in a box purged with nitrogen or when a strong nitrogen current was flowing between the detecting electrodes, since there are no longer oxygen molecules, and the attachment process disappears. The on axis intensity of the Nd:YAG laser around the focal region of the axicon was slightly above 10^{10} W/cm 2 , which is well below what is required to photoionize air. As a result, we attribute the appearance of the second peak to the detachment of the electrons from O_2^- ions and subsequent multiplication through an avalanche process. We observed this ns laser revived plasma at delays up to several ms in quiet atmosphere.

Figure 3.3(b) shows the measured magnitude of the second peak induced by the revived plasma, as a function of distance of the detection system from the beginning of the filament. It is seen that the plasma channel is revived over about half meter propagation distance. Note that a longer revived plasma channel would be obtained with higher ns laser energy and a larger initial beam diameter leading to a longer focal line. We also measured the magnitude of the signal as a function of the Nd:YAG laser energy (Fig. 3.3(c)). The sharp rise of the signal with laser energy above ~ 190 mJ reveals that an avalanche process is involved.

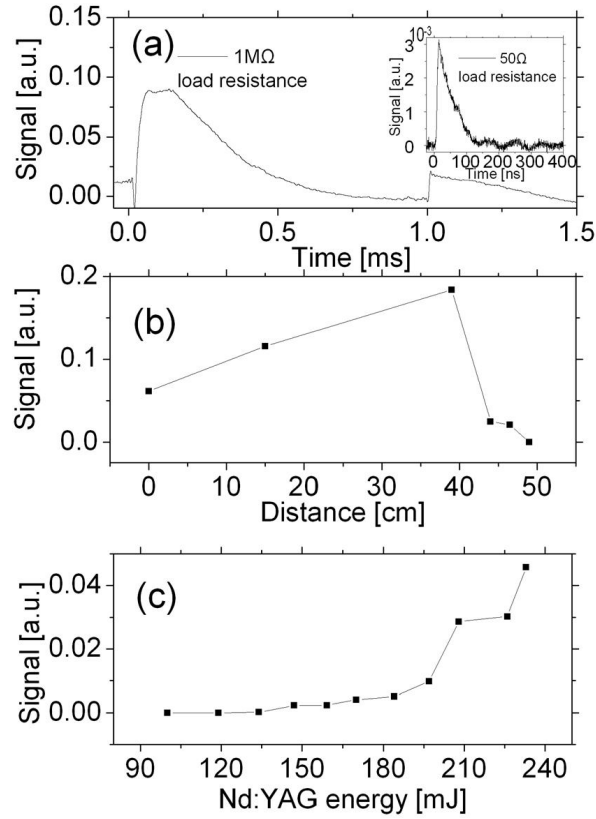


Figure 3.3: (a) Signal detected using the electrical method, showing plasma channel initially created by the fs laser and then revived by the ns laser (532 nm) after 1 ms.(b) Magnitude of the signal from the revived plasma at various distances from the beginning of the initial plasma filament. (c) Magnitude of the signal from the revived plasma as a function of the Nd:YAG laser pulse energy. In (b) and (c) each point corresponds to the average of 100 measurements. The mean fluctuation around the average is 5%.

3.3.1 Simulation and Results of the plasma revival

In order to compare our experimental results with theoretical models we have also numerically estimated the electron density evolution under conditions similar to the experiments. The chain of events leading to the revival can be cast into the following coupled nonlinear rate equations:

$$\frac{dn_e}{dt} = -\beta_{ep}n_en_p - \eta n_e + \alpha(I_2)n_e + \sigma \left(\frac{I_2(t)}{h\nu} \right) n_n, \quad (3.1)$$

$$\frac{dn_p}{dt} = -\beta_{ep}n_en_p - \beta_{np}n_n n_p + \alpha(I_2)n_e, \quad (3.2)$$

$$\frac{dn_n}{dt} = -\beta_{np}n_n n_p + \eta n_e - \sigma \left(\frac{I_2(t)}{h\nu} \right) n_n, \quad (3.3)$$

where n denotes density and the subscripts e , n and p denotes electrons, negative ions and positive ions, respectively. β_{ep} , β_{np} and η are the rates for electron-ion recombination, ion-ion recombination and attachment to neutral molecules. The attachment coefficient is a function of the amplitude of the laser electric field, and is found from the addition of the two-body and three-body interactions [Zhao 1995]. α is the impact ionization rate, which depends on the pulse intensity, ionization potential of the neutral molecules and laser wavelength; it is calculated according to Drude model [Yablonovitch 1972a]. I_2 is the intensity of the ns pulse, σ is the cross section for absorption of a photon and consequent detachment of the electron (calculated from the experimental results of Burch *et al.* [Burch 1958]), ν is the ns laser frequency and h is Planck's constant.

At $t = 0$, n_e and n_p are taken to be 10^{17} cm^{-3} and n_n to be zero consistent with measurements performed in filaments [Couairon 2007]. We numerically solved Eq. (3.1) in the absence of the last terms to obtain the densities at the arrival time of the ns laser, and reinserted these values as initial conditions for the same rate equations, last term included, which describe the change in the densities during and after this long pulse excitation. The results of the calculations (Fig. 3.4) agreed well with the experimental observation. Note that since the equations do not take into account the increase of absorption cross section with electron temperature, they are limited to describe the full evolution towards dielectric breakdown for higher intensities used during experiments shown below.

3.3.2 Optical breakdown inside the plasma channel revived with two nanosecond lasers

Based on Eq.(3.1), the principal interactions involved in the revival process have different frequency dependence. The photo detachment rate of O_2^- ions increases with increasing photon energy [Méjean 2006], whereas the avalanche process is more efficient at lower frequencies [Yablonovitch 1972b]. This brings up the opportunity of using together both the fundamental and the second harmonic frequencies of the YAG laser. In this case, the second harmonic can detach the electrons and the

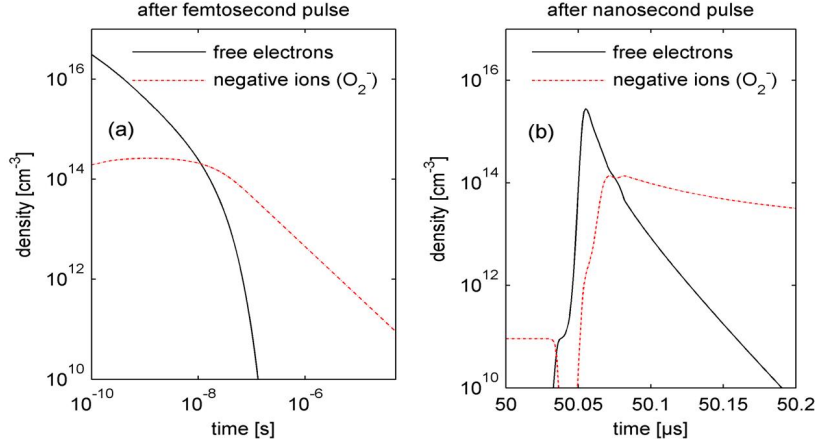


Figure 3.4: Evolution of free electron and O_2^- ion densities: (a) After the fs laser excitation. (b) During and after the delayed ns pulse (at 532 nm) excitation. The end of the time axis in (a) coincides with the beginning of time axis in (b). The fs pulse arrives at $t = 0$ and creates the initial plasma channel of density $10^{17} cm^{-3}$. The ns pulse is a Gaussian with 10 ns (FWHM) duration, has its peak 50 ns after the beginning of time axis of (b) (at $50.05 \mu s$) and it has a peak intensity of $10^{11} W/cm^2$.

fundamental can accelerate and multiply them. We performed such experiments using two separate YAG lasers emitting at 532 and 1064 nm respectively. By focusing both beams with conventional lenses and using the appropriate chronological order for the pulses, sufficient combined laser intensity was available to induce a full evolution of the plasma towards dielectric breakdown. The initial plasma filament in this case was generated by the 15 mJ fs laser focused by a 75 cm focal length lens. The fundamental beam made 10 degrees angle with the other two laser beams. The fundamental and second harmonic of the ns laser (focused with 40 cm and 75 cm focal length lenses, respectively) arrived after 53 microseconds (μs) delay, the second harmonic pulse was followed after 10 ns by the fundamental pulse. The characteristic spark due to optical breakdown was easily observed (see Fig.3.5(b)). We verified that no breakdown occurred when the fs laser was blocked. Figure 3.5(a) compares the revived plasma optical signal observed through the UV interference filter to that of the initial filament plasma. We note that the revived plasma lasts at least $1 \mu s$, and that the corresponding optical signal exceeds that of the filament during more than 200 ns. The probability to obtain a fully developed breakdown was measured as a function of the relative delay between the two ns pulses, for a fixed delay of $53 \mu s$ with respect to the fs laser pulse. In consistence with the expectations mentioned above, we observed a maximum probability of 100% when the 532 nm pulse arrived first and the 1064 nm pulse comes after a delay of 10 ns (see Fig. 3.5(c)). Moreover, with sufficiently strong lasers we could produce YAG Bessel-like beams with similar intensities and generate longer revived plasma channels.

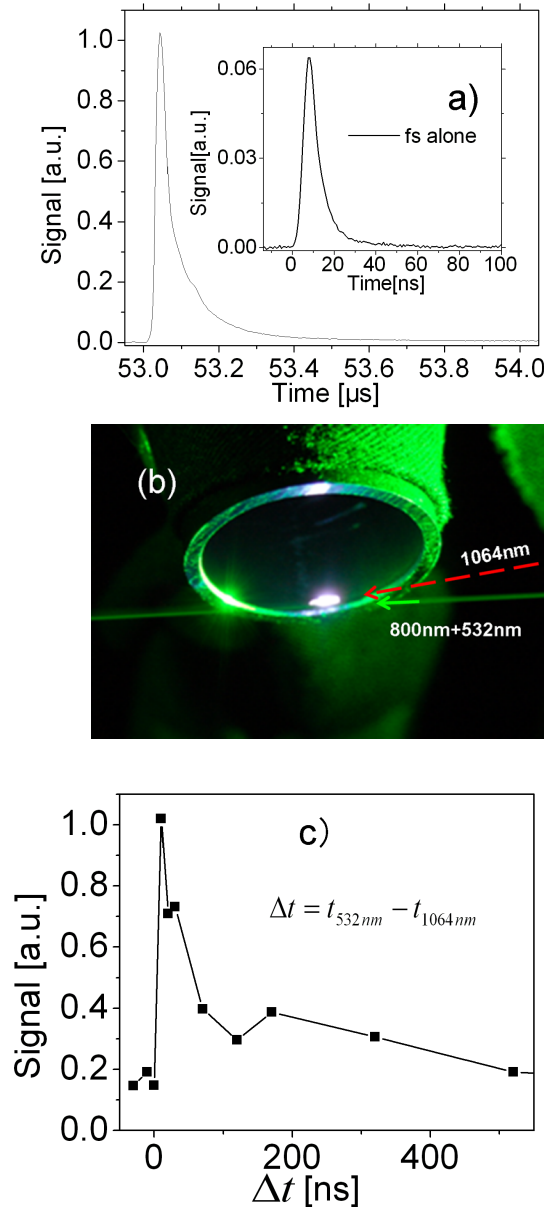
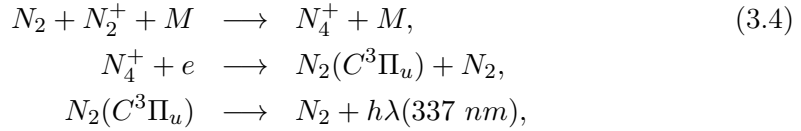


Figure 3.5: Three beam configuration when both YAG laser pulses are delayed by 53 μs with respect to the fs laser pulse: (a) Signals detected by the PMT with a 338 nm filter in the presence of breakdown. The laser pulse at 1064 nm arrives 10 ns after the pulse at 532 nm. The optical signal recorded under the same conditions with the fs laser alone is shown in the inset (the magnitudes can be compared). (b) Photograph of the breakdown spark in a three laser beams configuration. The beam paths are shown with a red and a green arrows respectively. (c) Revival plasma triggered breakdown probability as a function of delay between the 1064 nm and 532 nm. A positive delay corresponds to the 532 nm pulse arriving first. Each point is an average over 1000 shots (breakdown probability $p = \frac{N_{break}}{N_{laser}}$, where N_{laser} is the number of laser shots, and N_{break} is the number of breakdown).

3.3.3 Experimental evidence for the existence of N_4^+

Recently, a new mechanism of the near UV fluorescence (337 nm) of air inside a femtosecond laser plasma filament has been described [Xu 2009]. The primary reactions are the following:



where M is the third body as a buffer. Through the reactions, the electronic excited state $N_2(C^3\Pi_u)$ of N_2 is populated and emits the photon ($\lambda = 337 \text{ nm}$). Due to the balance between nonlinear focusing and plasma defocusing, the laser intensity is clamped to $5 \times 10^{13} \text{ W/cm}^2$ inside the filament core. After the passage of the laser pulse, most of electrons gain an energy less than $3.2U_p = 9.6 \text{ eV}$ ($U_p \approx 3 \text{ eV}$ is ponderomotive energy [Krausz 009]). The energy required for exciting $N_2(C^3\Pi_u)$ state by direct electron impact is around 14.1 eV, thus electrons do not have enough kinetic energy to directly excite this state.

By a three body reaction with the buffer M , N_2 and N_2^+ can interact with each other to form a dimer ion N_4^+ . The generation of the state $N_2(C^3\Pi_u)$ is obtained by a dissociation of this dimer ion with a free electron to emit the UV fluorescence line.

The inner structure of the dimer ion N_4^+ is $N_2^+ :: N_2$, and it is interesting to note that the bonding energy between the ion and molecule is 1.15 eV, which is a single photon energy at 1064 nm. To detect N_4^+ , we used the similar experimental set-up (Figure 3.2). We changed the ns laser pulse frequency to 1064 nm.

Figure 3.6 shows the fluorescence of a filament plasma channel fs filament alone and with a synchronized ns linearly polarized laser pulse. Both signals are obtained with a PMT and by averaging on 100 shots in order to reduce the noise. One can see that the amplitude is reduced in presence of the ns laser pulse. Indeed, the bond between N_2 and N_2^+ is broken by the 1064 nm photons and then the reservoir for the excited state is depleted. It leads to a reduction of 30% of the fluorescence. There are three types of bonds between the N_2 and N_2^+ [Casto 1981], so the fluorescence decrease could depend on the duration, the polarization and the energy of the laser pulse.

3.4 Conclusion of plasma revival

We have demonstrated experimentally and verified theoretically that a fs laser generated plasma channel can be revived in air long after the passage of the fs laser pulse. The attachment of free electrons to oxygen molecules, which is usually perceived undesirable, can be turned to advantage as it provides storage of low affinity electrons. With a delayed ns laser, these electrons can be detached and multiplied

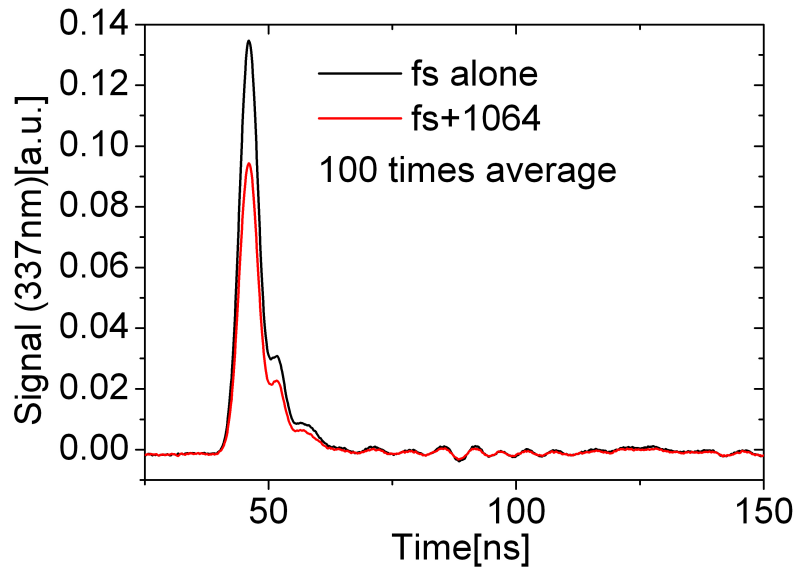
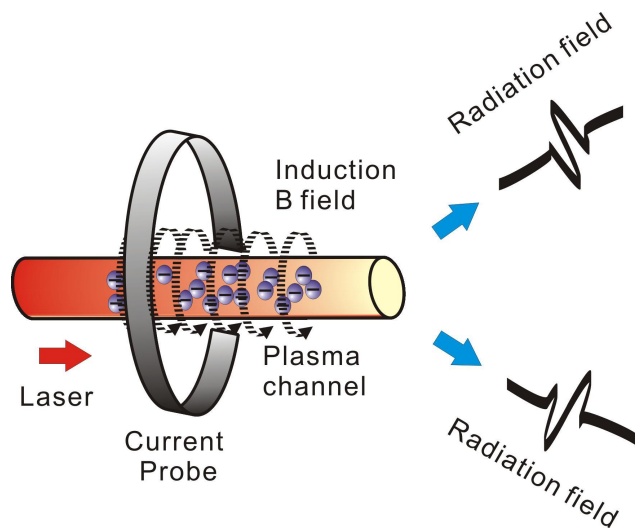
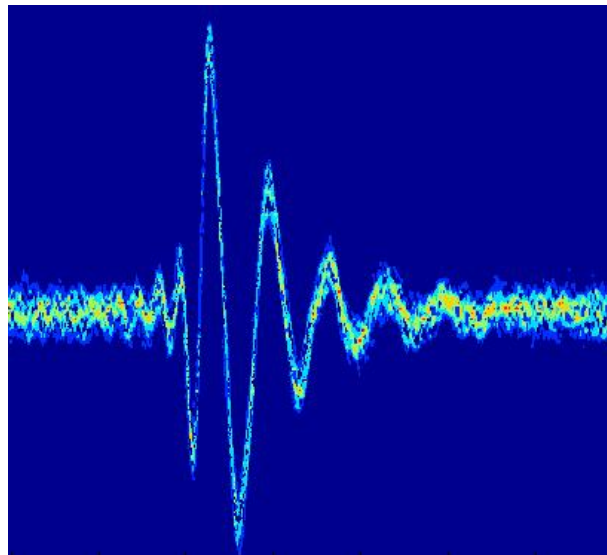


Figure 3.6: Fluorescence of the filament plasma fs laser alone and with a simultaneous 1064nm ns linearly polarized laser pulse.

through impact ionization. We have observed revivals at delays as large as several ms. With sufficient ns laser intensity, the avalanche process could be pushed up to dielectric breakdown. The plasma lifetime in this case reaches μs . These results may prove to be important for applications of long distance filamentation in air, where the short lifetime of the plasma poses strong limitations, but a very energetic ns laser pulse would be required to revive a long plasma channel.



Chapter 4: Measurement and control of electric currents in the wake of femtosecond laser pulses in gases



Measurement and control of longitudinal electric currents in the wake of femtosecond laser pulses in gases

Contents

4.1	A specially designed air-core high speed current monitor	45
4.1.1	Bi-components of B field near a filament	46
4.1.2	A specially designed high speed current monitor	47
4.1.3	Current signal inside a femtosecond filament	50
4.2	Oscillating currents inside femtosecond filaments	53
4.2.1	Oscillating current inside a filament plasma with external static electric field	54
4.2.2	Oscillating currents in nitrogen gas	55
4.2.3	The oscillating currents in Argon gas	61
4.2.4	The oscillating currents in other gases	64
4.3	A homeostasis of two forces inside a filament plasma	66
4.3.1	A classic model for an electron with laser field	66
4.3.2	The homeostasis inside a plasma column	69
4.4	The plasma oscillating currents in dilute air	73
4.4.1	A single plasma channel in dilute air	74
4.4.2	Laser intensity dependence of the currents in a non filament plasma channel	78
4.4.3	Laser polarization and gas pressure dependence of the currents in a non filament plasma channel	79
4.5	Controlled oscillating current with Bi-color laser pulse inside a filament	81
4.6	Conclusion on the oscillating current inside the laser induced plasma channel	83

In the last decade, collimated beams of energetic electrons have been obtained experimentally over short distances by focusing an intense ultrashort laser pulse

in a neutral gas [Tajima 1979, Mangles 2004, Faure 2006]. This is accomplished by first launching the converging pulse in vacuum, so that the laser intensity at the focus can reach a relativistic regime $v/c \sim 1$ with $I > 10^{19} \text{W/cm}^2$ before interacting with the gas. Here v is the velocity of free electrons accelerated by the laser field and c the velocity of light. Differently, for weakly converging beams, when a laser pulse propagates in a continuous neutral gas, the laser peak intensity is unavoidably limited to values around $10^{13} - 10^{14} \text{W/cm}^2$ because of multiphoton absorption and defocusing effect by gas ionization. Moreover, for an initial power $P > P_{cr}$ (For instance the critical power $P_{cr} \sim 5 \text{GW}$ in air at 1bar pressure), the pulse undergoes filamentation, a process in which a dynamic competition between beam self focusing and plasma defocusing leads to the formation of a thin, weakly ionized plasma column in the trail of the self guided laser pulses [Couairon 2003]. Short-lived longitudinal oscillations are initially excited within the short-existed plasma, as evidenced by the pulsed conical THz radiation emitted by filaments in the forward direction [D'Amico 2007, Houard 2007]. It has been speculated that by injecting electrons in the wake of the self focused pulse at the appropriate phase of the plasma oscillation, one could continuously accelerate them over long distances in atmosphere. It is therefore important to understand and control the phase of the plasma waves in the process which excites their longitudinal oscillations. The mastering of these currents is vital for the long term goal of achieving long distance electron acceleration in the atmosphere by intense short laser pulses [Esarey 2009].

In this chapter, we investigate the current circulation that is created in the wake of a short, intense IR femtosecond laser pulse propagating freely in gases. Note that we only measure the longitudinal oscillating currents. Therefore, for simplicity unless otherwise specified, all the currents presented in the following chapter are directed along the laser propagation axis.

Firstly I will present a specially designed high speed current monitor along with its characteristics; this allows us to detect longitudinal currents with good sensitivity. Then I will show the laser polarization dependence and gas pressure dependence of the measured current signals in diverse gases. And then, I will interpret all the experimental results with a physical model, in which we calculate the total laser force acting on the free electrons, and qualitatively evaluate the coulomb force acting on the opposite direction. Moreover, we will also measure and discuss currents in very dilute air (less than 0.01 mbar). As the nonlinearity decreases and the mean free path (**MFP**) of electrons is prolonged, the current that we observed is entirely different; in the end, I will show bi-color laser pulse induced current oscillations: when the focused laser pulse passes through a thin BBO doubling crystal ($100 \mu\text{m}$), by varying the phase between 800 nm and 400 nm, the longitudinal current amplitude can be enhanced, and the initial current phase can be changed. So far we do not have any appropriate explanation of this effect.

4.1 A specially designed air-core high speed current monitor

In Chapter 3, we mentioned two methods to detect the existence of laser induced plasma channel: measuring the fluorescence of gas molecules and the capacitive probing method. Measuring the fluorescence can only be adapted to certain gases, but the spatial resolution is good since it is limited by the optical resolution. The capacitive method has a poor spatial resolution, although it can be improved by reducing the size of the capacitive probe. The determination of the plasma density from this type of measurement is still difficult, since the external static electric field interacts with the plasma. The plasma channel is changed, as a result the signal can only reflect qualitatively the nature of the plasma column. Its big advantage is the high sensitivity, making it a simple practical device to show evidence for the formation of a plasma column.

There is another approach demonstrated by a Canadian group using a small antenna placed in the vicinity of the filament [Proulx 2000]. By using the unshielded antenna, the radiation E field generated by the plasma column has been detected to estimate the distribution of free electrons in the plasma channel. However the E field near the plasma column is so complex that the measured signal is very hard to analyze. To measure the electronic current in the filament we first attempt to use a commercial current monitor based on Rogowski coil. The sensitivity and the bandwidth of this probe were not sufficient to detect clearly the fast current in the filament. Jean Larour from LPP suggested us to use probe that he designed to measure short rising time currents in z pinch experiments [Larour 2003]. This monitor uses a principle discovered by C. Ekdahl in 1980 [Ekdahl 1980] and consist in a hollow copper tore with a circular aperture on the center. Its detection principle is similar to an Idot Rogowski coil [Rogowski 1912] except that the volumic current induced in the coil is here replaced by a metal skin layer current, allowing detection of very high frequencies. Placed around the filament axis, the small circular aperture on the inner side of the tore allows the azimuthal magnetic field induced by the axial current to penetrate the cavity inside the tore. The B field generates a potential difference V between the two sides of the tore, a potential difference, which is picked up by a SMA plus connected to a fast oscilloscope.

I optimized this prototype to obtain a sensitive, non invasive detection probe able to directly measure the longitudinal current oscillation in a filament in the frequency domain between 0 and 6 GHz. The longitudinal spatial resolution is around 3 mm, therefore it is sufficiently precise to analyse centimeter long filaments. Note that for the measurement, the current needs to pass on the axis of the current monitor, otherwise it will induce an aberrant response, which leads to inaccurate current measurement.

4.1.1 Bi-components of B field near a filament

To understand the principle of the current monitor first let us calculate the magnetic field in a plasma column. Supposing that a current exists inside the volume \mathbf{V} , and that the current density is $J(t, \mathbf{x}')$ (shown in Figure 4.1), Eq.(4.1) describes the overall magnetic fields $B(t, \mathbf{x})$:

$$\mathbf{B}(t, \mathbf{x}) = \frac{\mu_0}{4\pi} \int_{\mathbf{V}} \left(\frac{J(t'_{ret}) \times \hat{\mathbf{e}}_{\mathbf{x}-\mathbf{x}'}}{|\mathbf{x}-\mathbf{x}'|^2} + \frac{1}{c} \frac{\dot{J}(t'_{ret}) \times \hat{\mathbf{e}}_{\mathbf{x}-\mathbf{x}'}}{|\mathbf{x}-\mathbf{x}'|} \right) d^3\mathbf{x}', \quad (4.1)$$

$$\dot{J}(t'_{ret}) = \left. \frac{\partial J}{\partial t} \right|_{t=t'_{ret}},$$

where \mathbf{x} represents the position in xyz -coordinates, t_{ret} is the retarded time, $\hat{\mathbf{e}}$ is the unit vector. The first term is the induction field, which is proportional to the current density. The induction field dominates near the plasma channel but dies out rapidly with distance from the channel. This is the electrostatics version of the Biot-Savart law in electrostatics. The second term is the radiation field, which is proportional to the derivative of the current density. The radiation field (or far field) propagates over a large distance and in principle its energy can be transported to infinity. In particular, for a laser induced plasma channel, the longitudinal oscillation of electrons gives rise to these two components of the magnetic field. Figure 4.2 gives a schematic representation of the induction and radiation fields created in a filament plasma.

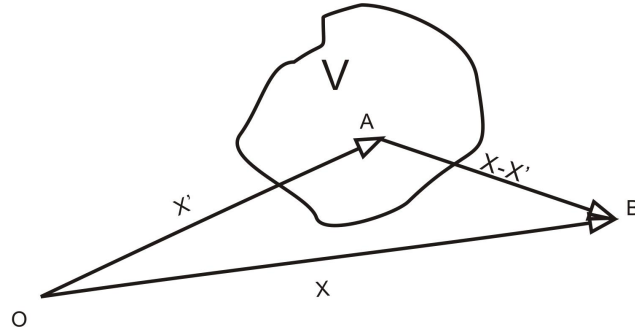


Figure 4.1: \mathbf{O} is the origin, \mathbf{x} is the coordinate vector of \mathbf{B} , which denotes the arbitrary volume element in volume \mathbf{V} ; \mathbf{x}' is the coordinate vector of a point \mathbf{A} inside the volume.

In practice, although it is easier to detect the EM-radiation field traveling in free space, the measurement of this field can hardly be used to retrieve the original current shape and amplitude. Fortunately, because of the special geometry of laser induced plasma channel, which is similar to a linear conductor, the induction magnetic field surrounding the plasma channel can be measured to extract information of the longitudinal current oscillation.

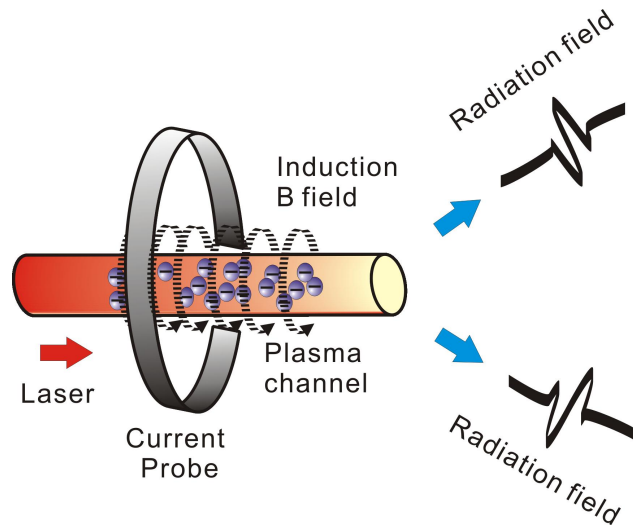


Figure 4.2: Schematic representation of the induction and radiation fields created in a plasma filament.

4.1.2 A specially designed high speed current monitor

Usual current probes are the so-called B-dot monitors: small size pick-up coils and Rogowsky belts.

Pick-up coils are based on small area, few turns, wire loops. Normally, the coils are very sensitive to the azimuthal magnetic field, but their response depends strongly on coil axis orientation, exact area and distance to current axis. Rogowsky belts (RBs) are toroidal solenoids with a large number of turns of insulated wire around a non-magnetic torus. Typically the sensitivity is from 0.1 to 0.01 Volts/Amperes. Since RBs are made from insulated wire, it is hard to measure more than 1 GHz high frequency current.



Figure 4.3: Picture of the fabricated current monitor.

Based on Rogowski coil principle [Rogowski 1912], the inductive groove measure

the derivative of the azimuthal induction B field generated by the longitudinal oscillating current in a filament. The fabricated coil is shown in Figure 4.3. By construction the outer side of the current monitor is grounded and isolated from any noise, while its particular toroidal geometry makes it only sensitive to the axial component of the current.

Figure 4.4 illustrates the inner structure of the coil. The annular cavity is machined between radii R_i and R_e and faces the coaxial central conductor through a spacing of width E allowing the penetration of very high frequency magnetic fields only. That evaluates the limitation of noise immunity. In our case, $E = 1\text{mm}$, therefore the cutoff frequency f_{cutoff} is $c/E \approx 3 \times 10^{11}\text{Hz}$.

4.1.2.1 Calculation of the equivalent RLC circuit

Inductance and capacitance of the annular cavity Consider a wire with a current of intensity I in Figure 4.4. The current induces an azimuthal induction magnetic field \mathbf{B} at a distance r from the current. $B(r) = \frac{\mu_0 I}{2\pi r}$, where μ_0 is the permeability in vacuum. The induced B field fills inside the annular cavity, the flux of the magnetic field is $\varphi = \int_{R_i}^{R_e} B(r) ds + \int_R^{R_e} B(r) ds$, where ds is the element of area of the loop. Based on the cavity geometry, the flux is given by

$$\varphi = \frac{\mu_0}{2\pi} I (H \ln(R_e/R_i) + E \ln(R_e/R_0)). \quad (4.2)$$

When the azimuthal magnetic field flux in the cavity varies with time, according to Faraday's law of induction, the initial induced potential between the Aa and Bb is

$$V_{initial} = -\frac{\mu_0}{2\pi} \left[H \ln \left(\frac{R_e}{R_i} \right) + E \ln \left(\frac{R_e}{R_0} \right) \right] \frac{dI}{dt}. \quad (4.3)$$

From Eq.(4.3) the total inductance of the annular cavity is

$$L = \frac{\mu_0}{2\pi} \left[H \ln \left(\frac{R_e}{R_i} \right) + E \ln \left(\frac{R_e}{R_0} \right) \right].$$

The ratio of the original current signal to the measured voltage signal depends mostly on the inductance of the annular cavity. Thus by changing the inductance, we can optimize the sensitivity of the current detector.

Due to the gap between Aa and Bb, the annular cavity has an internal capacitance. Considering a gap width E , the capacitance can be evaluated to $C = \varepsilon_0 \pi (R_i^2 - R_0^2)/E$. The cavity has then a resonant frequency:

$$f_{re} = \frac{1}{2\pi\sqrt{LC}}. \quad (4.4)$$

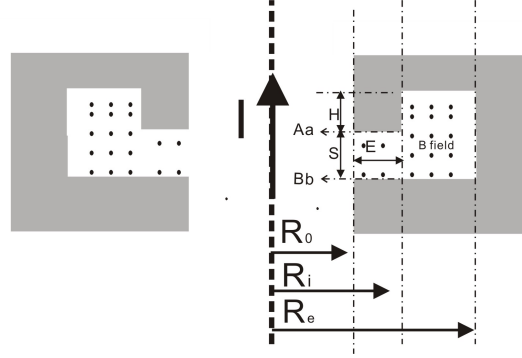


Figure 4.4: Cross section of the annular cavity. I is the detected current.

Skin effect in the annular cavity The induced potential difference $V_{initial}$ in the cavity generates a high frequency current flowing near the inner-surface of the annular cavity. The penetration depth of this current is called skin depth:

$$\delta(f) = \frac{1}{\sqrt{\pi\mu f\sigma}}, \quad (4.5)$$

where σ is the conductivity of the material, μ is its permeability, and f is the current frequency. According to the Laplace equation $\Delta V = 0$ and the Ohm law $J = \sigma\mathcal{E}$ (\mathcal{E} is the electric field), the total resistivity of the annular cavity is

$$R(f) = \frac{1}{2\pi\sigma\delta(f)} \left[\frac{h}{R_e} + \frac{h}{R_i} + 2\frac{R_e}{R_i} \right]. \quad (4.6)$$

From the Eq.(4.6), we can estimate the resistance due to the skin effect. The resistance is related to the signal damping in the cavity. The current probe is then equivalent to a resonant RLC circuit with a resonance frequency $f_{re} = 1/(\pi\sqrt{LC})$ and a quality factor $Q = \frac{1}{R}\sqrt{\frac{L}{C}}$. For the RLC resonant cavity, the frequency selectivity depends on the resistance. Normally, the skin effect induced resistance is low (less than 1Ω), therefore the resonant peak in frequency domain will be more narrow, and the cavity will become more selective in frequency, the non resonant frequencies are highly suppressed; By inserting an appropriate resistance inside the cavity, the resonant peak will be flattened, so it is reliable to monitor the broadband signal with less distortion when it circulates in the cavity.

By choosing the geometrical parameters, one can adjust L , C and R to meet special requirements. Since we are interested in high frequency current (300 kHz-up to 6 GHz), we used a groove with the parameters shown in Table 4.1. Using the formulae above, we calculate the inductance $L = 1.29$ nH, the capacitance $C = 2$ pF and the resistance for $R = 9$ m Ω . Based on the classic theory of RLC circuit, the resonant frequency is then $f_{re} = 3.1$ GHz, and the Q factor is around 2.7×10^3 . To decrease the Q factor down to 5 and flatten the probe response in frequency domain we inserted a 5 Ω resistor inside the cavity.

Table 4.1: The parameter of the home-brewed current monitor

Parameter	Value
H	9 mm
E	1 mm
R	7 mm
R _i	11 mm
R _e	20 mm

4.1.2.2 The coil calibration

The previous calculation gave a good estimation of the current probe response but to retrieve precisely the original current signal an exact calibration of the system (including the SMA connectors and cables) is necessary. We used a network analyzer to measure in amplitude and phase the frequency response of the annular cavity. Figure 4.5 shows the comparison of the calculated and the measured response from 300 kHz up to 6 GHz. The two curves are matching well at high frequencies, while for frequencies below 3.1 GHz the theoretical response presents a smaller amplitude. It may be due to the manufacturing inaccuracy, since the L , C , R values are very sensitive to the geometrical parameters of the annular cavity.

For the experimental processing we will use the measured response function to retrieve the current signal, since for the real annular constructed cavity the measured functions are more accurate than the theoretical simulation. Furthermore, by sending a known signal, we found the correspondence of the measured signal's polarity to the direction of the current, which passes through the current monitor.

Due to its annular structure, the current monitor is not sensitive to the electric radiational components generated by the transient current. In the further measurements, the response time of our detection system is limited by the detection oscilloscope to a time response of 58.3 ps. Additionally, by displacing the coil along the filament, one can obtain a representation of the current amplitude along the filament axis with a nearly 3 mm longitudinal resolution.

4.1.3 Current signal inside a femtosecond filament

To form filaments, we use a 3 mJ, 40 fs, horizontally polarized laser pulse at 800 nm. By focusing the pulse with a 1.5 m focal lens, we generate a nearly 7 cm long plasma column in the atmosphere, as confirmed by an image of the 337 nm luminescence of excited N₂ molecules. The signal measured by the current monitor is shown in Figure 4.6. The measured signal is distorted by the probe's frequency and phase response, therefore deconvoluting the measured signals with the probe response function yields a faithful reconstruction of the electronic current below 6

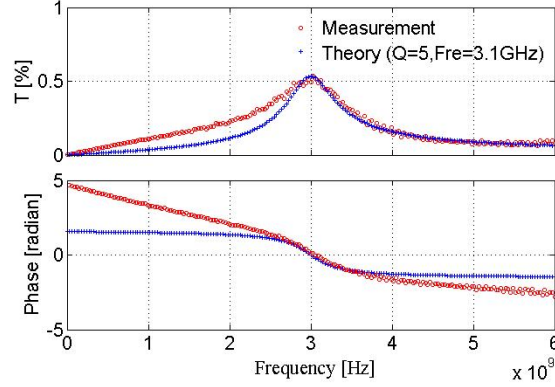


Figure 4.5: Comparison between theory and measurement of the frequency response of the annular cavity between 300 kHz and 6 GHz. On Top: Amplitude. On Bottom: Phase.

GHz. Figure 4.7 shows the reconstruction of the measured signal. Comparing with the measured signal, the reconstructed signal can be considered as an integration of the previous one with a compensation of the dispersion in cables. Considering the heavy positive ions are at rest, a positive signal denotes that the electrons move forward along \mathbf{z} propagation direction (corresponding to increasing z). Unless otherwise mentioned, I will only show processed signals.

The plasma density in atmospheric pressure is 10^{16} cm^{-3} . The plasma oscillating frequency can be expressed as

$$\nu_{ep} = \frac{1}{2\pi} \sqrt{\frac{n_e e^2}{m_e \epsilon_0}}, \quad (4.7)$$

where m_e is the electron mass, n_e is the electron density, e is the charge for a single electron, and ϵ_0 is the permittivity of free space. The numerical application in our case gives $\nu_{ep} \sim 0.5 \text{ THz}$. Comparing with plasma frequency, the frequency range of the current monitor is low, and therefore does not allow to reconstruct the wave profile of the plasma oscillations. But nevertheless it is feasible to extract the initial oscillation direction of the electrons and the current amplitude in the lower frequency range. The current monitor opens a pathway towards a deep comprehension of the laser induced plasma channel.

Normally, to measure the waveform of THz radiation from a plasma filament, one can use THz time-domain spectroscopy [Grishkowsky 1990]. This method makes the assumption that for each laser shot the THz radiation waveform remains unchanged, since the signal has to be averaged over many shots. The ability of the current monitor to perform single shot measurement allows to measure statistically the influence of the laser pulse to pulse fluctuations.

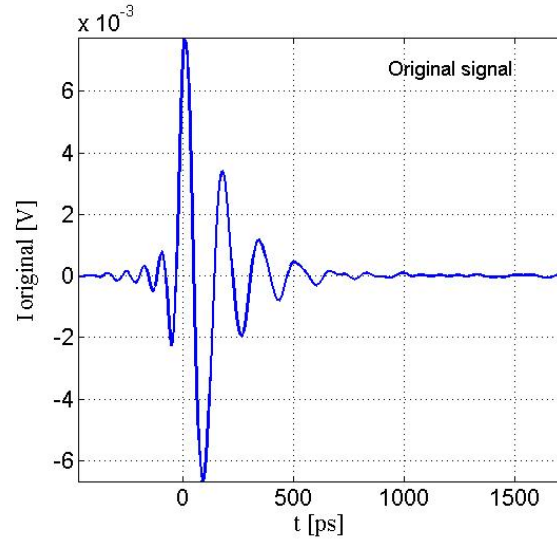


Figure 4.6: Measured signal in air 1 bar with a 3 mJ, 40 fs, horizontally polarized laser pulse at 800 nm. The focal length is 1.5 m.

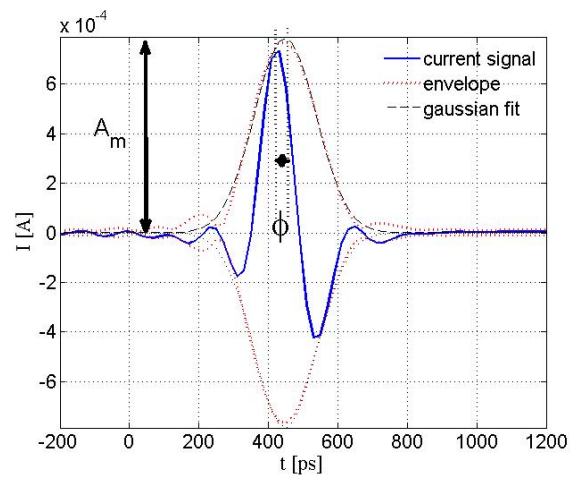


Figure 4.7: Reconstructed current signal (blue circle line), its envelope (red dash line) and gaussian fit of the envelope (black dash line).

as shown in Figure 4.7, to analyze the different current waveforms we fitted the signal with a gaussian envelope pulse formulated as:

$$I_{recon} = A_m e^{-\frac{(t-t_D)^2}{\tau^2}} \cos(\omega t + \phi), \quad (4.8)$$

where A_m is the current amplitude, t_D is the current signal delay, τ is the temporal width, ϕ is the absolute phase, which represents the initial current direction and ω is the current frequency. As an illustration, Figure 4.8 shows ϕ as a function of A_m for 40 laser shots in 1 bar air. The small variations of A_m and ϕ are attributed to the pulse to pulse fluctuation of the laser pulse energy.

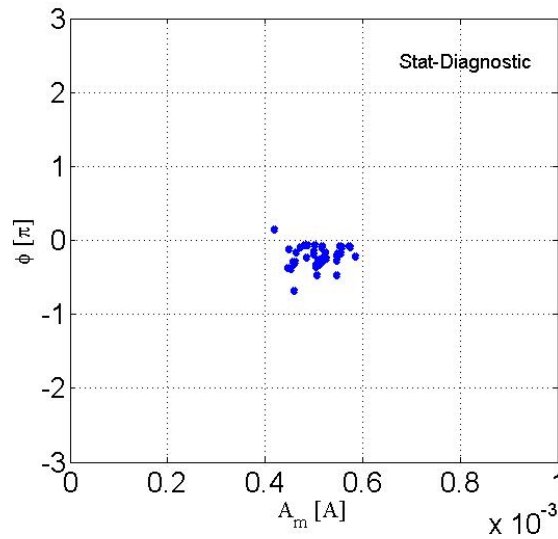


Figure 4.8: Extracted A_m and ϕ from current signals in 1 bar air. Laser pulse: 3 mJ, 35 fs, linearly polarization. The focal length is 1 m.

4.2 Oscillating currents inside femtosecond filaments

The femtosecond laser induced plasma channels in gases can be put into two categories: a filament plasma and a non filament plasma. In most gases, once the propagating laser pulse exceeding a certain power, the laser beam will be focused due to the nonlinear index n_2 [Mizrahi 1985, Shimoji 1989, Ripoche 1997]. When the intensity is high enough to liberate the bounded electrons, a plasma is form and defocus the laser beam. A dynamic competition is established between self focusing and beam defocusing, so that a uniform filament can be formed over long distance. In this case, the plasma channel formed in the wake of the ionization front is very uniform, and the laser intensity is clamped to $\sim 10^{13} \text{ W.cm}^{-2}$. In the weakly ionized plasma only 0.1% of neutral atoms or molecules is ionized.

When a converging laser beam propagates in very dilute gases, due to the weakness of nonlinearity, P_{cr} is strongly increased ($P_{cr} \propto 1/p_{gas}$, where p_{gas} is the gas

pressure). As a result the beam will not be self focused, but with sufficient laser intensity the gas will still be ionized, creating a strongly inhomogeneous plasma channel with an important density gradient. The limitation of the laser intensity by the plasma is much higher, so the gas can be fully ionized if the laser input power is high enough.

The behaviors of the oscillating currents varied in both cases. In this section, we will only present the oscillating current measurements in the filament plasma.

Very often, a filament plasma in gases has varied applications. For instance, it can trigger the lightning and be used in Lidar. Moreover, a filament plasma plays a very important role in THz generation. Such diverse spectrum of the applications ignite a debate about how the electrons initiate the oscillation inside the laser induced plasma channel [Chin 2002, Yu 2004, Couairon 2005b, Akturk 2007]. So far the scenario is still a puzzle, therefore to better understand the electronic oscillation, we will compare the oscillating current in different gases as the base for the further discussion.

4.2.1 Oscillating current inside a filament plasma with external static electric field

To further confirm that the probe can measure the oscillating current inside the filament plasma, we conducted an experiment with an external static electric field, which can push and pull the electrons after their birth. The setup is shown in Figure 4.9. By focusing a 10 mJ, 40 fs linearly polarized laser pulse with 2 m focal lens, a 30 cm long filament is formed. We put the current monitor in the middle of the plasma channel, and a ringlike electrode 8 cm before the current monitor. The inner circle diameter of the electrode is around 3 mm, therefore the filament can pass freely. The cover of the current monitor is connected to the ground.

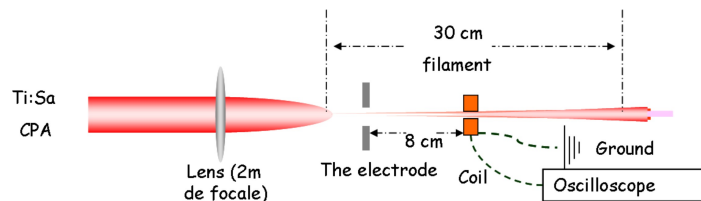


Figure 4.9: Experiment Setup. The electrode is connected to a voltage power supply. The focal length is 2 m, the laser pulse is 40 fs, 12 mJ, and the central wavelength is 800 nm. The current monitor external surface is connected to the ground.

First, we measured the currents in the middle of the plasma channel with 0 V and +20 V (see Figure 4.10A). According to the current signal, without external electric field, electrons initially go forward; when the potential of the electrode is changed to +20 V, the current oscillation is weakened, and a slow decay appears at the tail of the current signal. This results from the fact that the static electric field created by the electrode drives the electrons backward during the lifetime of free electrons (~ 1 ns).

If we further increase the voltage to +40 V, the net momentum of electrons becomes backward, the current oscillation in the plasma channel disappears. Differently, the current decays exponentially in one nanosecond. This slow decay corresponds to the decrease of free electron density due to inelastic collisions with ions and neutral molecules (recombination and attachment). With a voltage of -40 V applied, electrons are further pushed forward, therefore the current signal become positive (see Figure 4.10B).

Figure 4.10C shows the current signals as a function of the applied voltage (note that the voltage is on the ordinate axis). Since the initial momentum of electrons is forward, the current signal first decreases, and then increases, when the electrode potential is varied from 0 V to 40 V. Notably, for each given position along the filament plasma channel, there is an optimum positive voltage for which the electron initial forward momentum is canceled. Similarly, by measuring the forward terahertz emission from a filament in a static field, Liu *et al.* observed the cancelation of this emission at a given value of the external static field [Liu 2008]. The optimum voltage depends on the position along the plasma channel. The initial momentum of electrons p_e can be estimated to $\sim eE_{ex}\tau_{in}$ at given position along the plasma channel. e is the single electron charge, E_{ex} is the the real electric field generated by the optimized voltage and τ_{in} is the inelastic collision time.

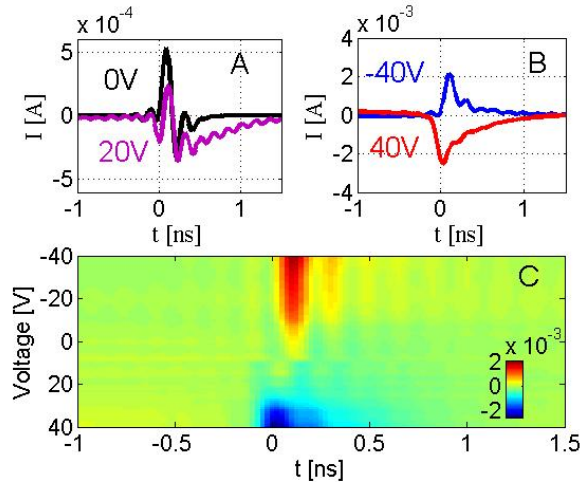


Figure 4.10: A. Current signal with 0 V and 20 V; B. Current signal with -40 V and 40 V applied to the electrode; C. Current signal with various voltages. The blue and red colors denote the negative and positive current value respectively.

4.2.2 Oscillating currents in nitrogen gas

4.2.2.1 Experimental set-up

To measure the oscillating currents in different gases and gas pressures, we fabricated a 60 cm tube to implement the experiments (Figure 4.11). The tube and two 1 mm

thick windows are made of fused silica. The diameter of the tube is 1 cm, so that the current monitor can surround it, and be displaced freely. To confirm that the tube does not distort the current signals, Figure 4.12 shows the comparison of the measured signals with and without the tube in 1 bar air. The laser pulse is 3 mJ, 40 fs duration, and linearly polarized. The current signals are nearly the same, except that with the tube the signal is a little smaller in amplitude due to the energy loss, when the laser pulse passes through the entry window of the tube.

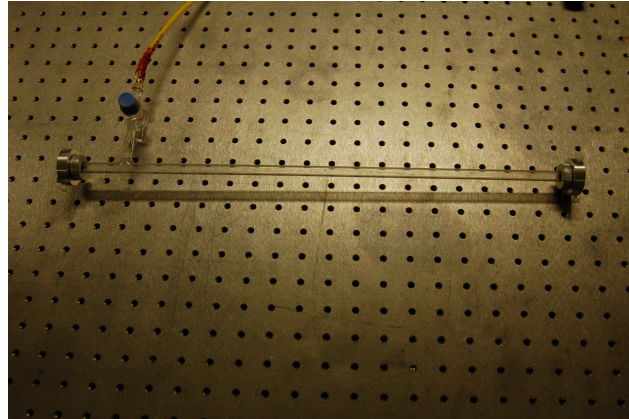


Figure 4.11: The fabricated 60 cm long fused silica tube. The diameter is 1 cm.

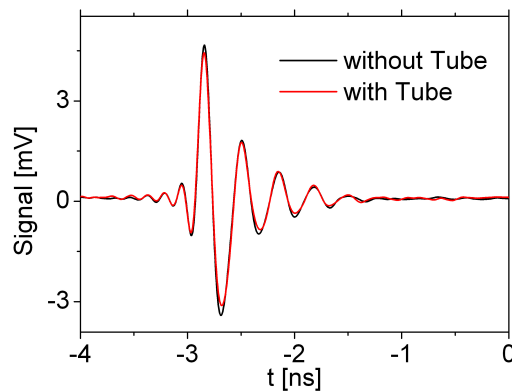


Figure 4.12: Comparison of the measured current signals (100 shots average) with and without the tube in Air at 1 bar. The focal length is 1.5 m. The laser pulse is 3 mJ, 40 fs, and is linearly polarized.

4.2.2.2 Comparison of the currents in air and nitrogen gas

Since nitrogen gas is the major component in air, we compare the current signals in both air and N_2 in Figure 4.13. In both gases, the initial electron movement is forward (the positive signal represents the case where the electrons move with the

same direction as the laser propagation). The current amplitude in air is slightly larger, we attribute this slight increase to the lower ionization potential of oxygen ($U_i = 12.06$ eV) compared to the one of N_2 .

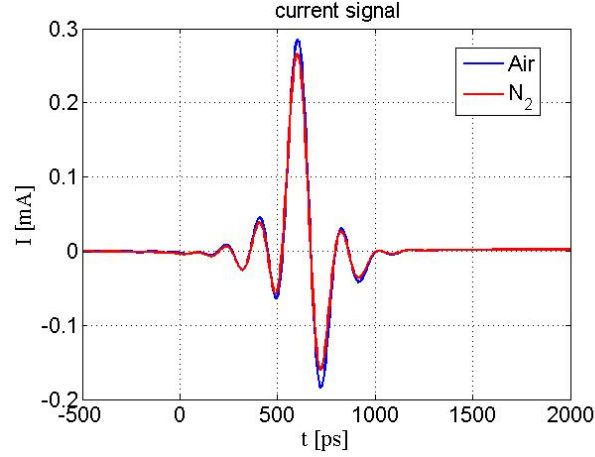


Figure 4.13: Comparison of the measured current signals in air and nitrogen gas at 1 bar pressure. The focal length is 1.5 m. The laser pulse is 3 mJ, 40 fs, and is linearly polarized.

Meanwhile, we displaced the current monitor along the plasma channel in air and nitrogen gas in Figure 4.14. The red color denotes that the electrons are pushed forward, and the blue denotes that the electrons go backward. The charge $Q(t, z_i)$ represents how many charge move back or forward at the given position z_i . The currents existing length is 4 - 5 cm in air and Nitrogen gas, in agreement with numerical results using a classical non linear propagation code. The upward tilt of the oscillatory patterns corresponds to the speed of the ionization front $v \sim c$. It shows that in both cases the plasma oscillation maintains a constant phase velocity $v \sim c$. Besides the current amplitude, the current oscillations are nearly the same, therefore nitrogen gas plays the leading role in air filament plasma.

4.2.2.3 Polarization dependence of the currents in nitrogen gas at the atmospheric pressure

Both the kinetic energy and the trajectory of electrons after their birth depend strongly on the laser polarization, therefore the current oscillation should be sensitive to the laser polarization. This can be seen in Figure 4.15, where we measure the currents in nitrogen gas at 1 bar pressure for both linear and circular polarized light. The initial electron movement is forward in both cases, the current amplitude for the circularly polarized light is more than 3 times larger than for the linearly polarized light. In a filament the laser intensities are comparable for both polarizations ($\sim 10^{13} \text{W/cm}^2$), consequently the electron densities are in the same order of magnitude ($\sim 10^{16}/\text{cm}^3$). Therefore the enhancement of the current with circularly polarized

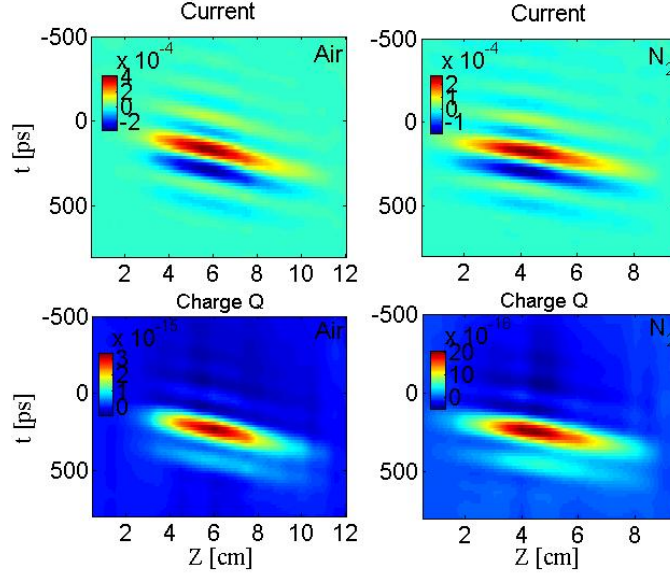


Figure 4.14: Comparison of the Z-scan currents along plasma channel in air (left) and nitrogen (right) gas at 1 bar pressure. The focal length is 1.5 m. The laser pulse is 3 mJ, 40 fs, and is linearly polarized. The charge is $Q(t, z) = \int_{-\infty}^t I(t', z) dt'$.

laser is due to the fact that the electrons gain more kinetic energy in the forward direction.

To further explore the relationship between the currents and the laser polarization, we measured the current as a function of the ellipticity of the laser pulse ($\varepsilon = E_x/E_y$). $\varepsilon = 0$ means the laser pulse is linearly polarized along y axis; $\varepsilon = 1$ means the laser pulse is circularly polarized. To show the evolution of the current waveform as a function of laser ellipticity, we used Eq. (4.8) to fit the current measurement. The current amplitude A_m and absolute phase ϕ of the current signals are mapped in Figure 4.16 with the ellipticity indicated for the circular and linear cases. When the polarization of the laser pulse changes from linearly to circularly polarized light, ϕ remains nearly unchanged, which reflects the fact that the electron initial movement is always forward (see the insert); the growth of the current amplitude A_m points out that for the same energy and duration, the electrons gain more forward momentum with the circularly polarized laser pulse.

4.2.2.4 Pressure dependence of the currents in Nitrogen gas

For different polarizations of the laser pulses, the free electrons can gain various forward kinetic energy in 1 bar nitrogen, consequently the amplitudes of the electron oscillation varies. This dependence would be deepened at lower pressure, since the electron mean free path λ_{MFP} will be prolonged. For ideal gases, λ_{MFP} can be

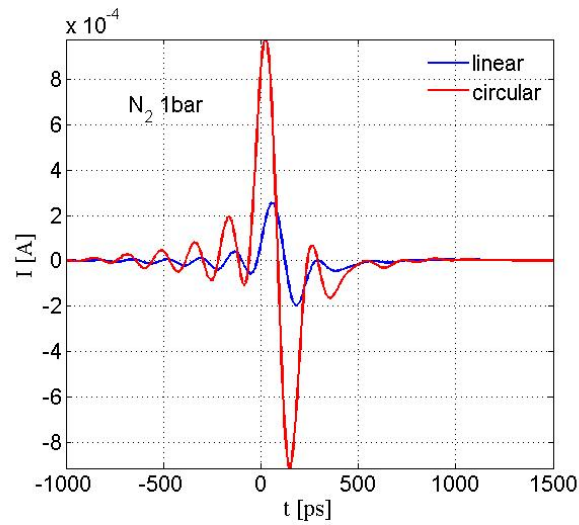


Figure 4.15: Currents in the middle of a filament plasma channel in nitrogen gas at 1bar pressure. The focal length is 1.5 m. The laser beam is 3 mJ, 40 fs. The blue curve is obtained for linear polarization and the red one for circularly polarized light.

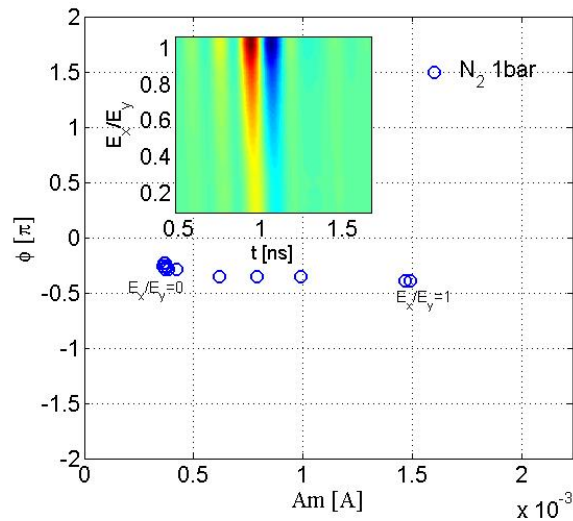


Figure 4.16: Polarization dependence of the currents in Nitrogen gas at 1bar pressure. The focal length is 1 m. The laser beam is 3 mJ, 40 fs. The inserted figure shows current signals as a function of the ellipticity of the laser pulse. The red and blue colors denote that the electrons go forward and backward.

determined from Avogadro's number and the ideal gas law, leading to

$$\lambda_{MFP} = \frac{RT}{\sqrt{2}\pi d^2 N_A P}, \quad (4.9)$$

where R is the universal gas constant, T is the gas temperature, d is the particle diameter, N_A is Avogadro's number, and P is the gas pressure. With longer λ_{MFP} , the electrons with the same kinetic energy will oscillate in the plasma channel with less damping. To verify this scenario, we measured the current as a function of the gas pressure for linearly and circularly polarized laser pulses. Similarly, I mapped $A_m - \phi$ in Figure 4.17 to compare the signal variation.

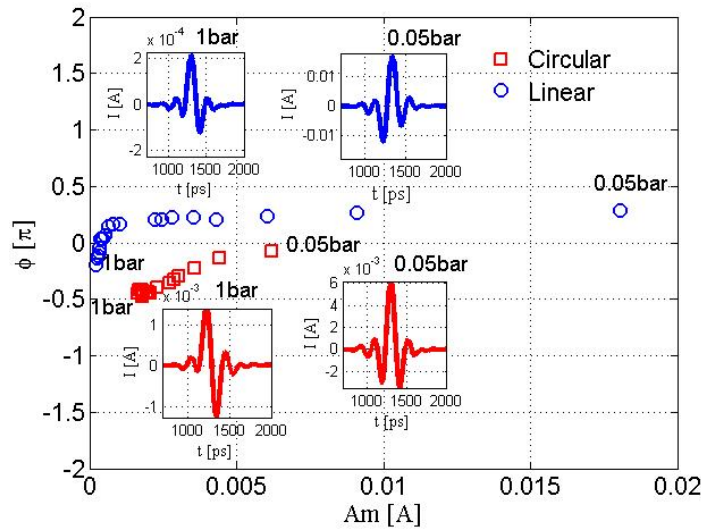


Figure 4.17: Pressure dependence of the currents in Nitrogen gas. The focal length is 1 m. The laser beam is 3 mJ, 40 fs. The inserted figures are current signals at 1 bar and 50 mbar. The interval of the measurement is 0.05 bar.

For the linearly polarized laser pulse, in the gas pressure range from 1 bar to 0.5 bar, the current amplitude A_m increases slightly, while ϕ goes up rapidly from negative to positive values, which reflects the facts that the initial movement of the electrons changes from forward to backward; at pressures below 0.5 bar, the growth of the current amplitude becomes more significant, surprisingly ϕ nearly keeps constant at positive values. For the circularly polarized laser pulse, the current amplitude A_m and phase ϕ are almost unchanged from 1 bar to 0.5 bar. Below 0.5 bar, similarly to the linear case, the phase ϕ grows until zero at 50 mbar, and the current amplitude also has an obvious enhancement. The inserted figures correspond to the current signals at 1 bar and 50 mbar.

The major factors are the laser intensity and the gas density. Due to the intensity clamping, the laser intensity remains unchanged, once a filament is formed.

For both linear and circular laser pulses, when the gas pressure decreases, the initial electron movement altered from forward to the backward direction. It stands

to reason that inside the plasma channel there exists a balance of forces, which drives the electrons initially forward or backward. One of the forces strongly depends on the gas pressure, because of higher ionization probability (the local laser intensity increases) it becomes more effective at lower gas pressure to drive the electrons backward initially. It is notable that if the electron density changes greatly with decreasing gas pressure, the plasma frequency shifts towards the lower frequency. This can also lead to a growth of the measured current amplitude, since the measured current only covers the range from 300 kHz to 6 GHz frequency. In this case, it is hard to distinguish whether the growth of the current amplitude is due to the decrease of the electron density, or to the increase of the pressure dependent force, or both. Fortunately, in the range of change of the pressure, the electron density nearly doesn't vary for the cold plasma. The ionization rate stays around 1%, as a result the growth of current amplitude is due to the pressure dependent force inside the plasma channel.

When the gas pressure decreases, the change of the electron initial moving direction in linear case is more easily from forward to the backward direction, since the initial forward momentum is weaker comparing with the circularly polarized laser pulse. We will discuss the balance of forces more in detail in the following sections.

4.2.3 The oscillating currents in Argon gas

Although the ionization potential U_i for Argon and Nitrogen gas are very nearly the same (for Argon $U_i = 15.759$ eV and for N_2 $U_i = 15.576$ eV), the electrons oscillation can be different due to the fact that the inelastic collision coefficients are greatly different in inert atom gases and molecule gases.

4.2.3.1 Laser Polarization dependence of the currents in 1 bar Argon gas

Similarly, we measured the currents as a function of the ellipticity of laser pulse (Figure 4.18). This time the $A_m - \phi$ map is different from the Nitrogen case. With the change of the ellipticity ε from 0 to 1, differently compared with Nitrogen gas, the electrons change the initial moving direction, and the current amplitude decreases.

Ostensibly, the oscillating currents behave differently in Argon and Nitrogen gas, but through the appearance the variation of the currents follows the same rule: The electrons gain more forward momentum with circularly polarized laser pulse, consequently the backward momentum will be compensated, therefore the current amplitude decreased when the laser pulse change to the circular polarization. Moreover in both gases which have almost the same U_i , the current amplitude A_m and the phase ϕ are nearly identical for the circular polarization. Surprisingly, for linearly polarized laser pulse, in Argon the initial movement of electrons is backward, while in Nitrogen gas the electrons are pushed forward first with much less current absolute amplitude. This persistent puzzle goes to the heart of the electron oscillation within the laser induced plasma.

Table 4.2: The parameters in N₂ and Ar

Parameters	N ₂	Ar
U_i	15.576eV	15.759 eV
n_2	$2.3 \times 10^{-19} \text{ cm}^2/\text{W}$	$1.74 \times 10^{-19} \text{ cm}^2/\text{W}$
K	11	11
σ_K	$6.31 \times 10^{-140} \text{ s}^{-1} \text{ cm}^{22} \text{ W}^{-11}$	$5.06 \times 10^{-140} \text{ s}^{-1} \text{ cm}^{22} \text{ W}^{-11}$
I	$3.7 \times 10^{13} \text{ W/cm}^2$	$3.68 \times 10^{13} \text{ W/cm}^2$
$\rho(I)$	$1.13 \times 10^{16} \text{ cm}^{-3}$	$8.47 \times 10^{15} \text{ cm}^{-3}$

When a filament is formed in gases, the clamping intensity I and the plasma density $\rho(I)$ can be calculated in Eq. (4.10), where $\rho_c = m_e \epsilon_0 \omega_0^2 e^{-2}$; ρ_{at} is the neutral atom or molecule density; τ_p is laser pulse duration (in our case $\tau_p = 40 \text{ fs}$). For 1bar Ar and N₂, typically the central frequency of laser pulse ω_0 is $\frac{2\pi c}{0.8 \times 10^{-6}}$, ρ_{at} and ρ_c are equal to $1.74 \times 10^{21} \text{ cm}^{-3}$ and $2.5 \times 10^{19} \text{ cm}^{-3}$.

$$I = \left(\frac{0.76 n_2 \rho_c}{\sigma_K \tau_p \rho_{at}} \right)^{1/(K-1)} \quad (4.10)$$

$$\rho(I) = \left[\frac{(0.76 n_2 \rho_c)^K}{\sigma_K \tau_p \rho_{at}} \right]^{1/(K-1)}$$

With the parameters in Table 4.2.3.1 [Lehmeier 1985, Shelton 1990, Nurhuda 2004], we calculated the laser clamping intensity and the electron density for the linearly polarized laser pulse. Both the clamping intensity and the electron density at 1 bar N₂ and Ar are comparable, and therefore can not yield a discrepancy of the oscillating currents. Since the variation of currents is not due to the intensities and electron densities, another reason left can be the inelastic collision in various gases. When the electrons oscillates in cold plasma, inevitably the electrons collide with the ions and neutral particles, as a result the oscillation varies with the nature of gases.

4.2.3.2 Pressure dependence of the currents in Argon

Similar to our measurements in Nitrogen gas, Figure 4.19 shows the change of A_m and ϕ with the decrease of the gas pressure in Argon for both linearly and circularly polarized laser pulse. The pressure varies from 1 bar to 0.2bar (there can be still a filament formed in such range).

For the circular case, the behaviors of the A_m and ϕ are quite similar to those in Nitrogen gas. Both A_m and ϕ increase when the Pressure diminishes. For the linear case, the pressure dependent force already dominates at 1bar pressure. When the

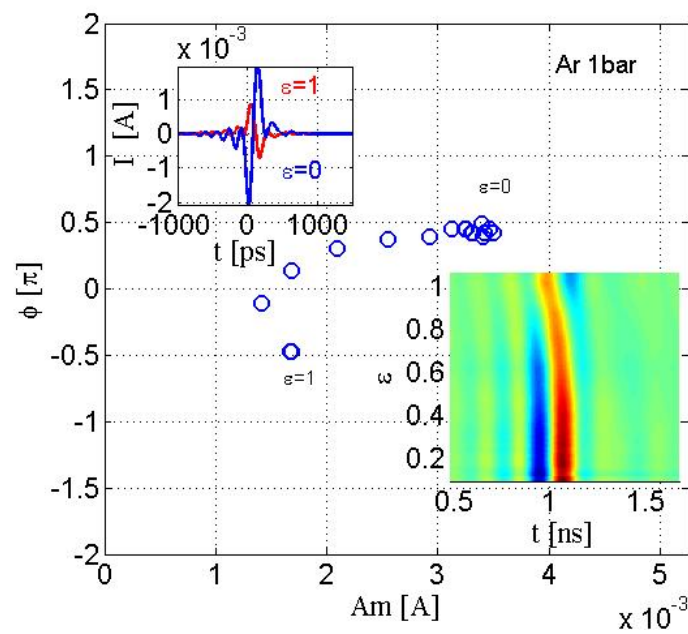


Figure 4.18: Polarization dependence of the currents in argon at 1 bar pressure. The lens' focal length is 1 m. The laser pulse is 3 mJ, 40 fs. The inserted top figure is the current signal with linearly and circularly polarized light. The inserted bottom figure shows current signals as a function of the ellipticity of the laser pulse. The red and blue colors denote that the electrons go forward and backward respectively

pressure decreases further, the electrons only gain more backward initial momentum, so that the current amplitude becomes larger, while the phase ϕ is always at $\pi/2$.

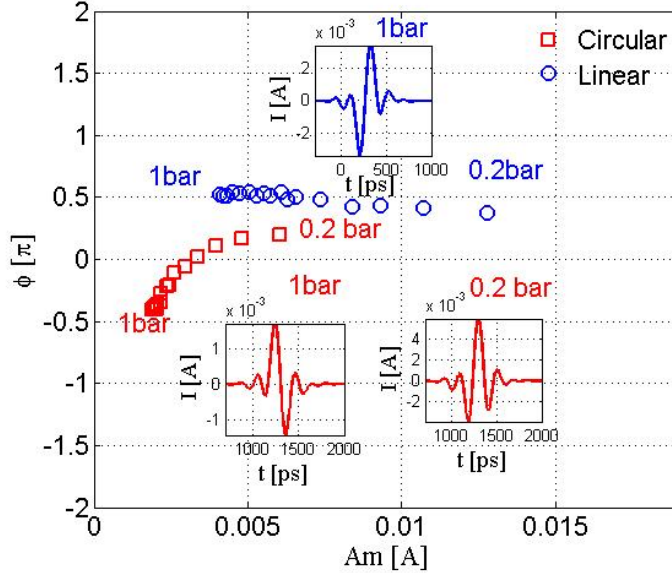


Figure 4.19: Pressure dependence of the currents in Argon. The focal length is 1 m. The laser pulse is 3 mJ, 40 fs. The inserted figures are the current signal with linearly and circularly polarized light. The interval of the measurement is 0.05 bar

4.2.4 The oscillating currents in other gases

So far, we have demonstrated the oscillating current in both N_2 and Ar. We found that the oscillating current does not only depend on the laser polarization, but also varied with the gas and gas pressure. To fully sort out the currents in gases, we also compared the oscillating current signals in other gases.

4.2.4.1 The pressure dependence of the currents with linear and circular polarization

Figure 4.20 shows the pressure dependence of the current amplitude A_m and phase ϕ for both linearly and circularly polarized laser pulses. In Kr, both linear and circular cases behave almost in the same manner as we measured in Ar; in CO_2 , the current signals are similar to that in N_2 ; in O_2 , for both linear and circular cases, the pressure dependent force already dominates and drives electrons moving backward first at 1 bar pressure. At each pressure, the current amplitude is larger in linear case, since the linearly polarized laser pulse favors the domination of the pressure dependent force. This unique behavior of the current in O_2 could be due to the nature of the gas.

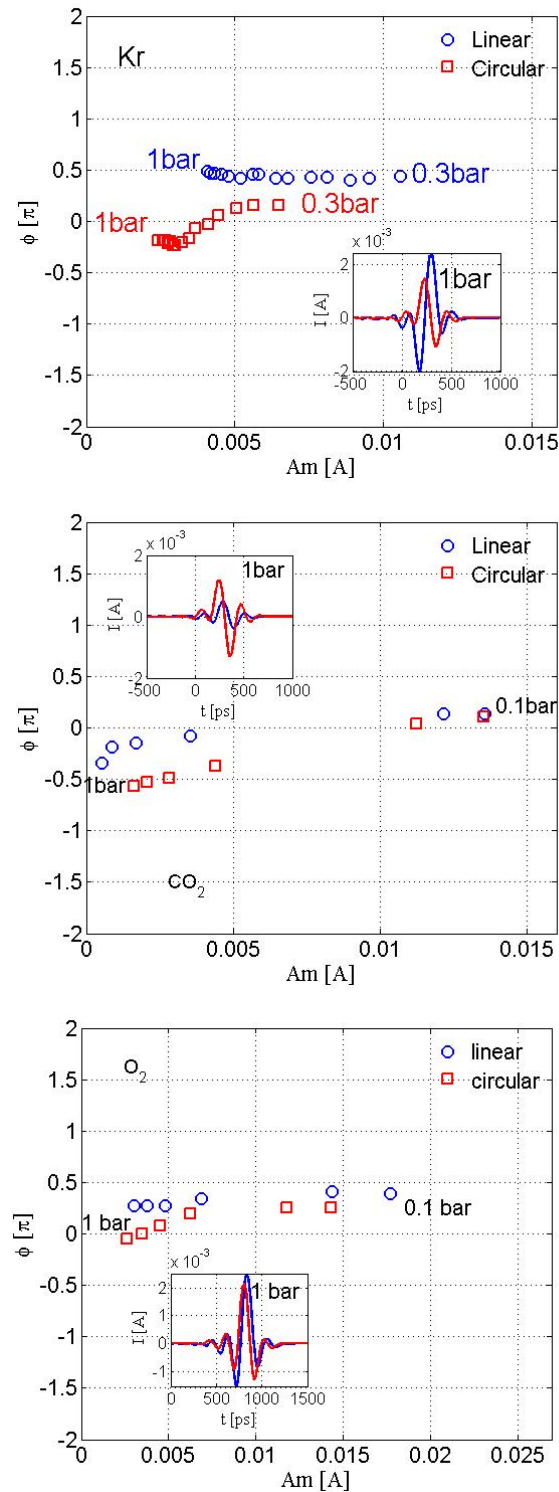


Figure 4.20: Pressure dependence of the currents in Kr, CO_2 , and O_2 . The focal length is 1 m. The laser pulse is 3 mJ, 40 fs. The inserted figures are the current signal with linearly and circularly polarized light at 1 bar. The interval of the measurement is 0.05 bar in Kr, and the pressures are 1 bar, 0.8 bar, 0.4 bar, 0.2 bar, 0.1 bar in CO_2 and O_2 .

4.3 A homeostasis of two forces inside a filament plasma

Previously, we presented the oscillating currents when a filament plasma is formed in the wake of the laser pulse. The current amplitude and the electron initial moving direction depend on the laser polarization, gas pressure, and the type of gases. In this section, we will draw a simple model for the electron oscillation through the varied current signals.

In short, during the presence of a filament plasma, electrons undergo three periods:

(A) Ionization stage: the bonded electrons are liberated; (B) Quiver motion stage: the free electrons gain kinetic energy from laser; (C) oscillation and damping stage: The electrons in the plasma channel oscillate and become at rest.

For the periods (A) and (B), the laser pulse plays a dominant role; in the last period, the oscillation depends on the type of the gas and the gas pressure. For the first period, A.Couairon calculated the electron interaction with the laser pulse.

4.3.1 A classic model for an electron with laser field

When a filament is formed in gases, the laser intensity is clamped around $10^{13}\text{W}/\text{cm}^2$, and is far away from the relativistic regime. We can use the classic model to describe the motion of an electron in the laser field.

Newton equation for an electron undergoing the effect of the Lorentz force is Eq.(4.11), where \mathbf{p} is the momentum of the electron, \mathbf{E} and \mathbf{B} are the electric and magnetic part of the laser field.

$$\frac{d\mathbf{p}}{dt} = -e(\mathbf{E} + \mathbf{v} \times \mathbf{B}) \quad (4.11)$$

The electric and magnetic fields can be expressed with the potential vector \mathbf{A} .

$$\mathbf{E} = -\frac{\partial \mathbf{A}}{\partial t} \quad \mathbf{B} = \nabla \times \mathbf{A} \quad (4.12)$$

The electric and magnetic fields of the laser pulse are orthogonal and transverse(perpendicular to the propagation direction). At first order, the electron is accelerated by the electric field in the transverse direction; At second order, the magnetic component of the Lorentz force coupling the transverse velocity with the transverse magnetic field induces a longitudinal motion of the electron. Transverse motion (First order):

$$\frac{d\mathbf{p}_\perp}{dt} = e\frac{\partial \mathbf{A}}{\partial t} \quad (4.13)$$

Further more, the Eq. (4.13) can be integrated as Eq. (4.14), where $p_{\perp,0}$ is the momentum of the electron at $t = 0$.

$$p_\perp = \mathbf{p}_{\perp,0} + e(\mathbf{A}_\perp - \mathbf{A}_{\perp,0}) \quad (4.14)$$

According to Eq.4.11, the parallel motion (Second order) along the laser propagation is

$$\begin{aligned}\frac{dp_{//}}{dt} &= -e(\mathbf{v} \times (\nabla \times \mathbf{A})) \cdot \mathbf{u}_{//} \\ &= \frac{e}{m} [(\mathbf{p}_{\perp,0} - \mathbf{A}_{\perp,0}) \times (\nabla \times \mathbf{A}_{\perp}) + e\mathbf{A}_{\perp} \times (\nabla \times \mathbf{A}_{\perp})]\end{aligned}\quad (4.15)$$

$\mathbf{u}_{//}$ is the vector unit along the laser propagation.

By means of the identity: $\nabla A^2/2 = (A \cdot \nabla)A + A \times \nabla \times A$ and the expression $\nabla \times A = (-\partial_z A_y, \partial_z A_x, \partial_x A_y - \partial_y A_x)$, Eq.4.15 becomes:

$$\frac{dp_{//}}{dt} = -\frac{e}{m} \frac{\partial}{\partial z} [((\mathbf{p}_{\perp,0} - e\mathbf{A}_{\perp,0}) \cdot \mathbf{A}_{\perp} + eA_{\perp}^2/2)] \quad (4.16)$$

Note that: $\xi = z - ct$, $\tau = t$. Derivatives: $\partial t = \partial \tau - c\partial \xi$, $\partial z = \partial \xi$. Assumption: dependence upon ξ only ($\partial \tau$ is neglected, which amounts to neglecting the difference between phase and group velocity, i.e dispersion: the pulse is luminal). Therefore, Eq.4.16 yields to

$$\frac{dp_{//}}{d\xi} = -\frac{e}{mc} \frac{\partial}{\partial \xi} [((\mathbf{p}_{\perp,0} - e\mathbf{A}_{\perp,0}) \cdot \mathbf{A}_{\perp} + eA_{\perp}^2/2)] \quad (4.17)$$

Through integration:

$$p_{//} = p_{//,0} + \frac{e}{mc} [p_{\perp,0} \cdot (\mathbf{A}_{\perp} - \mathbf{A}_{\perp,0}) + \frac{e}{2} (\mathbf{A}_{\perp} - \mathbf{A}_{\perp,0})^2] \quad (4.18)$$

Eq.(4.18) can also be rewritten as:

$$p_{//} = p_{//,0} - \frac{p_{\perp,0}^2}{2m} + \frac{1}{2mc} [p_{\perp,0} - e(\mathbf{A}_{\perp} - \mathbf{A}_{\perp,0})]^2 \quad (4.19)$$

Eq. 4.18 is valid both for linear and circular polarizations. The quantities $p_{//,0}$ and $\mathbf{p}_{\perp,0}$ denote the longitudinal and transverse components of the momentum, respectively, when the electron is liberated from the Coulomb attraction of the parent ion, i.e, after ionization but before being accelerated by the laser pulse.

These quantities can be estimated by writing conservation of the energy and momentum: N photons are necessary to liberate an electron, which corresponds to an energy $N\hbar\omega_0$ and a momentum $N\hbar\mathbf{k}_0 = N\hbar(\omega_0/c)(\mathbf{k}_0/k_0)$ transferred to newly born electrons:

$$N\hbar(\omega_0/c) = \mathbf{p}_{//,0} \quad (4.20)$$

The transverse component of momentum is preserved, if we consider that the parent ion carries a transverse momentum opposite to that of the electron (yet ions are assumed at rest as they are much heavier than electrons). The conservation of energy allows us to determine $p_{\perp,0}$:

$$N\hbar\omega_0 - I_p = \frac{p_{\perp,0}^2}{2m} + \frac{p_{//,0}^2}{2m} \quad (4.21)$$

where I_p denotes the ionization potential. From Eq.4.21, we obtain $\frac{p_{\perp,0}^2}{2m} = N\hbar\omega_0 - I_p - (N\hbar\omega_0)^2/2mc^2$. For an evaluation of order of magnitudes we can consider argon with ionization potential $I_p = 15.759$ eV(Ar). $N = 11$ photons are required to liberate an electron at 800 nm. This corresponds to an energy $N\hbar\omega_0 \sim 17$ eV. Thus $p_{\perp,0}^2/2m \sim 1.29$ eV and $p_{//,0}^2/2m \sim 2.8 \times 10^{-4}$ eV. The initial longitudinal momentum is negligible compared to the initial transverse momentum. Above threshold ionization is not considered in the above calculation (it would amount to using a higher number of photons $N > 11$). We can now calculate the final longitudinal momentum after the pulse by setting $\mathbf{A}_{\perp} = 0$ in Eq. 4.18:

$$p_{//,\infty} = N\hbar(\omega_0/c) + \frac{e^2}{2mc} \mathbf{A}_{\perp,0}^2 - \frac{e}{mc} \mathbf{p}_{\perp,0} \cdot \mathbf{A}_{\perp,0} \quad (4.22)$$

By introducing $N\hbar\omega_0$ from Eq.4.21 into Eq. 4.22, we find finally:

$$p_{//,\infty} = \frac{I_p}{c} + \frac{p_{//,0}^2}{2mc} + \frac{1}{2mc} (e\mathbf{A}_{\perp,0} - \mathbf{p}_{\perp,0})^2 \quad (4.23)$$

where $\mathbf{p}_{\perp,0} \approx \sqrt{2m(N\hbar\omega_0 - I_p)}$ and $\mathbf{p}_{//,0} = N\hbar\omega_0/c$. Eq. (4.23) is valid for both linear and circular polarizations, and it shows that the electrons are always pushed by the laser fields in the forward direction. In other words, the electrons gain the forward longitudinal net momentum from laser pulse. Even if the ponderomotive force tend to expel electrons from the regions of high fields, an electron born in the trailing edge of the pulse will still have a final momentum in the forward direction. Notably, this calculation does not include the effect of re-collisions when the electrons oscillate inside the plasma channel. Normally, the laser pulse is around 35fs, which is much less than the electron-neutral collision time τ_{en} at 1bar pressure (e.g. $\tau_{en} \sim 1.3$ ps in air)

The momentum of an electron with linearly polarized laser field:

Assuming that the laser pulse propagates along z direction, the electric field polarized in the x direction, this yield to

$$\begin{aligned} E &= E_{0x} [\cos(\frac{\pi\xi}{Tc}) \cos(\frac{\omega_0\xi}{c} + \theta)] \mathbf{u}_x \\ &= \frac{E_{0x}}{2} [\cos(\frac{\pi\xi}{Tc} + \frac{\omega_0\xi}{c} + \theta) + \cos(\frac{\pi\xi}{Tc} - \frac{\omega_0\xi}{c} - \theta)] \mathbf{u}_x \end{aligned} \quad (4.24)$$

where, T is laser pulse duration, and \mathbf{u}_x is the vector unit along x axis. $\mathbf{B} = B_y \mathbf{u}_x$ with $B_y = E_x/c$. This is an exact result due to the specific envelope (cosine shape) and the assumption that $v_g = v_\phi = c$. By rewriting the potential vector Eq.7.4 in terms of amplitude and phase:

$$A_x = \mathbb{A}_x \sin(\phi) \quad (4.25)$$

$$\phi = \frac{\omega_0\xi}{c} + \theta \quad (4.26)$$

$$\mathbb{A}_x = \frac{E_{0x}}{\omega_0} \cos(\frac{\pi\xi}{Tc}) \quad (4.27)$$

With the classic model described above, the momentum of an electron after the passage of the linearly polarized laser pulse is :

$$\overline{p_{//,0}} = p_{//,0} + \frac{U_{p,0}}{c} \quad (4.28)$$

$$\overline{p_{x,0}} = p_{x,0} - e\mathbb{A}_{x,0}\sin(\phi_0) \quad (4.29)$$

Since this quantity is always positive, the final electron momentum is always in the forward direction. The details of the calculation will be presented in Appendix.

The momentum of an electron with circularly polarized laser field

For the circularly polarized laser, the electric field is

$$E_x = E_0 \left[\cos\left(\frac{\pi\xi}{Tc}\right) \cos\left(\frac{\omega_0\xi}{c} + \theta\right) \right] \quad (4.30)$$

$$= \frac{E_0}{2} \left[\cos\left(\frac{\pi\xi}{Tc} + \frac{\omega_0\xi}{c} + \theta\right) + \cos\left(\frac{\pi\xi}{Tc} - \frac{\omega_0\xi}{c} - \theta\right) \right] \quad (4.31)$$

$$E_y = E_0 \left[\cos\left(\frac{\pi\xi}{Tc}\right) \sin\left(\frac{\omega_0\xi}{c} + \theta\right) \right] \quad (4.32)$$

$$= \frac{E_0}{2} \left[\sin\left(\frac{\pi\xi}{Tc} + \frac{\omega_0\xi}{c} + \theta\right) - \sin\left(\frac{\pi\xi}{Tc} - \frac{\omega_0\xi}{c} - \theta\right) \right] \quad (4.33)$$

$$\mathbf{B} = B_x \mathbf{u}_x + B_y \mathbf{u}_y \quad \text{with} \quad B_y = E_x/c \quad \text{and} \quad B_x = -E_y/c$$

By rewriting the potential vector in terms of amplitude and phase:

$$A_x = \mathbb{A}_\perp \sin \phi \quad (4.34)$$

$$A_y = -\mathbb{A}_\perp \cos \phi \quad (4.35)$$

$$\phi = \frac{\omega_0\xi}{c} + \theta \quad (4.36)$$

$$\mathbb{A}_\perp = \frac{E_0}{\omega_0} \cos\left(\frac{\pi\xi}{Tc}\right) \quad (4.37)$$

The electron longitudinal and transverse initial average momentum is :

$$\overline{p}_{//,0} = \frac{I_p}{c} + \frac{e^2}{mc} \mathbb{A}_{x,0}^2 \quad (4.38)$$

$$\overline{p}_{\perp,0} = p_{\perp,0} - e\mathbb{A}_{\perp,0} \quad (4.39)$$

Eq. (4.38) shows that the longitudinal initial momentum is also forward, and is larger than the one obtained with linear polarized laser pulse. The detailed calculation will be presented in Appendix.

4.3.2 The homeostasis inside a plasma column

As the calculation stands, the electrons only gain the forward longitudinal momentum when the laser pulse passes through the gases; surprisingly, the initial direction

of electron flow in Ar can be reverted by changing the laser polarization from linear to circular in Figure 4.18. To resolve the conflict, besides the laser forces, We propose another force which is due to the lateral ponderomotive sideways drift of free electrons born upstream in the filament. As the electrons move laterally, there is a backwards field, or wake field accelerating the electrons in the $-z$ direction. The magnitude of this wake field will depend sensitively on the electron mean free path λ_{MFP} . Ar and N_2 make a good pair of references, since they have comparable ionization potential U_i and nonlinearity n_2 . When a filament is formed, the laser intensity and the electron density are nearly the same in both gases. By comparing the difference and the similarity of the current signals in both gases, we will discuss more in detail the two forces.

4.3.2.1 The kinetic energy of electrons with Laser force

To interpret the homeostasis of forces, we first evaluate the effect of the laser force by considering the classical motion of an electron under the action of the Lorentz force. We assume electrons born at rest at a given instant in the pulse and compute their acceleration by the laser field. This yields the ponderomotive force. We also included collisional damping but found that the resulting light pressure is negligible. The transverse and longitudinal momentum of the electron after the passage of the pulse reads and where denotes the transverse component of the vector potential when the electron is born. The expressions for the kinetic energies along transverse and longitudinal direction and shows that for a pulse undergoing filamentation with peak intensity $I \sim 5 \times 10^{13} \text{W/cm}^2$ ($|\mathbb{A}_{\perp,0}|^2 = I\lambda^2/(2\pi^2\epsilon_0c^3)$), according to the Eq. 4.21 and Eq. 4.20, the electron momentum is mainly found along the transverse direction. For instance, in Argon, the ratio of $E_{\perp}/E_{//}$ is around 2×10^4 for the laser pulse central wavelength at 800nm .

Figure 4.21 shows the kinetic energy of the electrons after the passage of the pulse for linear and circular polarizations. With linearly polarized light, electrons are preferentially born by bursts close to the peaks of the electric field. Thus, they experience a nearly nil net ponderomotive force during the rest of the pulse leaving a large fraction of them with a small kinetic energy. The rest is drifting away almost radially from the filament zone. With circular polarization, electrons are born continually when the intensity exceeds a certain threshold. The fraction of electrons with small kinetic energy is thus insignificant as most of them are left with a final ponderomotive drift. The fraction of electrons with kinetic energy between 2 and 4 eV is much more important for circular than for linear polarization. These simulations are in good agreement with results presented in the more general case of [Corkum 1993].

4.3.2.2 The wake force inside the plasma channel

Since the laser pulse always pushes electrons downstream, the results point out to the necessity of a longitudinal force acting in the opposite direction Figure 4.22.

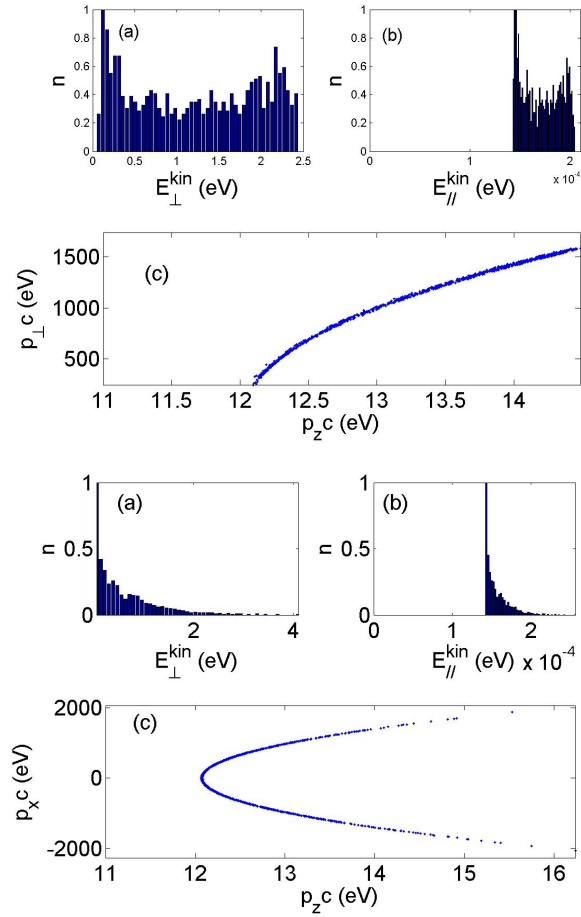


Figure 4.21: Calculated kinetic energies of free electrons born during filamentation in the transverse and longitudinal direction with respect to the filament axis z . Upper curve relates to circularly polarized laser light; lower trace is for linearly polarized light. Also shown are the histograms of (a) the transverse and (b) longitudinal drift energies.

We attribute this second force to the following effect. At birth, the electrons largest momentum is in the field direction. As a consequence, a positive space charge region starts forming behind the pulse due to the radial component of the ponderomotive drift, acting as a backwards oriented Coulomb wake force. Obviously, the mean free path of electrons will be a key factor in determining the strength of the wake force. It will be determined mainly by the collisions of electrons with neutrals, since the degree of ionization in a filament is small ($10^{-3} - 10^{-4}$).

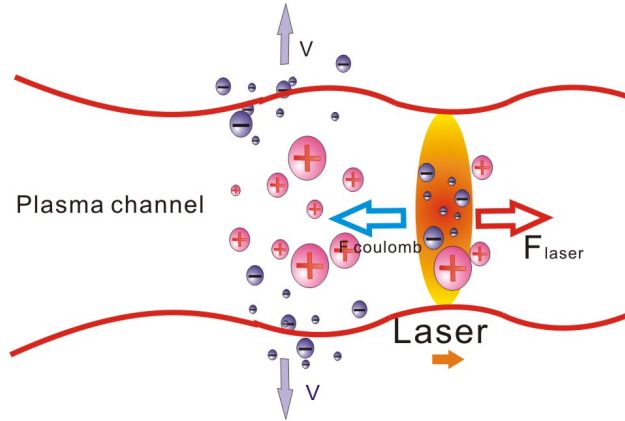


Figure 4.22: The illustration of the two forces inside the plasma channel

The competition between the two forces mentioned above explains naturally the observations. Consider first the results obtained with linearly polarized light at $1bar$, shown in Figure 4.18 and Figure 4.16. The different behavior of both gases shows that the wake force prevails over the laser force in Ar, while the laser force barely prevails in N_2 , as evidenced by the strong reduction of the signal. This can be explained naturally from inspection of the respective total electron scattering cross sections. The total scattering cross section of N_2 raises from 5 \AA^2 at 0.1 eV to 10 \AA^2 at 1 eV, is followed by a large inelastic spike ($\sim 30 \text{ \AA}^2$ at 2 – 3eV) and stays above 10 \AA^2 up to 30 eV [Itikawaa 2006]. The cross section of Argon, on the other hand rises from a small value below 0.5 eV and increases linearly to reach 20 \AA^2 at 10 eV [Subramanian 1987]. The ionization potential of both gases is nearly identical. The lateral drift energy of electrons in both cases computed in the absence of collisions is therefore similar. Taking into account the scattering of electrons in the range 0 – 1eV leads to an important reduction of the electron mean free path, and consequently of the magnitude of the Coulomb wake force, but principally in N_2 .

Results shown in Figure 4.18 and Figure 4.16 are explained along the same lines. As shown in Figure 4.21, with circular light, the electron drift energy (both longitudinal and transverse) is higher than with linear polarization. This favors an initial forward motion of the plasma wave because it simultaneously increases the forward drift energy (the laser force) and decreases the Coulomb wake force by increasing the

scattering cross section in both gases. Finally, the pressure dependence of the signals shown in Figure 4.19 and Figure 4.17 simply translates the increase of electron mean free path at decreasing pressure. With circular polarization, for which the laser force is predominant, the increase of the wake force is insufficient to revert the initial current direction in the plasma. With linearly polarized light, for which the forward electron drift is very small, the increase of the lateral drift is felt sensitively, even altering the initial balance in N_2 . These results show that measurement of the current in a filament can provide a sensitive tool to measure the electron scattering cross section as a function of pressure in different gases or in gas mixtures.

In short, for a filament plasma, we have presented experimental results showing that the phase of plasma oscillations in filaments depends sensitively on several parameters, and meanwhile we calculate the motion of electrons with a classic model. Finally, we converged on a homeostasis of two forces. The first is the Lorentz force which is perceptible although the laser intensity inside filaments is far below the relativistic regime. The second force is due to the lateral expansion of the free electron cloud born earlier in the filament yielding an effective Coulomb wake field. A change of laser polarization can alter the delicate balance between the two forces, forcing the initial plasma oscillation in either direction.

4.4 The plasma oscillating currents in dilute air

When an intensive laser beam propagates in gases, the self-focusing and plasma defocusing alternatively dominate, as a result the laser beam will keep nearly constant radius over longer distance than the Rayleigh length. Consequently, the laser intensity is clamped. With weak nonlinearity in dilute gas, the plasma column will be quite different.

Firstly, the radius of the plasma column, which is equal to the one of the laser beam, depends on the distance away from the geometrical focus of a lens in Eq. 4.40, where w_0 the waist radius, and $z_r = \frac{\pi w_0^2}{\lambda_0}$ is Rayleigh Length. For 1 m focal length, 800 nm laser beam, and beam diameter before lens $D = 1.2$ cm, we calculate and measure $w_0 = 65 \mu\text{m}$, therefore z_r is 1.66 cm.

$$w(z) = w_0 \sqrt{1 + (z/z_r)^2} \quad (4.40)$$

Secondly, with the decrease of the gas pressure, λ_{MFP} will be prolonged with several orders of magnitude. Consequently the kinetic electrons experience less collisions during their lifetime.

Lastly, when a 3 mJ, 40 fs laser pulse is focused, at the beam waist the intensity reaches $5.6 \times 10^{14} \text{W/cm}^2$. With such laser intensity, not only the single ionization exists, but also double ionization (**DI**) will be more weighted at the beam waist in gases [Guo 1998, Wells 2002]. The ratio X^{+2}/X^+ (X can be Ar , N_2 , O_2) depend on the laser intensity, laser polarization and the nature of the gas. (since there is no clear physical process for the second liberated electron, without loss of generality we assumed that the double ionization is non-sequential.) Before and after the beam

waist, the single ionization still dominates. Since the single ionization rate remains unchanged, the electron density is proportional to the gas pressure for the same laser intensity. As a result, plasma frequency will become longer.

4.4.1 A single plasma channel in dilute air

Due to the limitation of the system vacuum, we only conducted experiments in dilute air. In Figure 4.26 I compare the oscillating currents along the plasma channel at 1bar, 100mbar, 10 μ bar, and 0.2 μ bar for the linearly polarized laser pulse. By decreasing the gas pressure, the laser induced plasma column changes from a filament stage to a non-filament stage (see Figure 4.23), as a result the oscillating currents are significantly different.

At a filament stage:

In 1 bar air, due to the inelastic collision, the coulomb wake force is suppressed, as a result electrons move forward initially due to the forward momentum gained from the laser fields. The current phase remains unchanged along the plasma channel (see Figure 4.23 (upper trace)). The downwards tilt of the oscillatory patterns correspond to the speed of the ionization front $v \sim c$.

At a non-filament stage

The bottom trace of Figure 4.23 shows the oscillating currents at 0.4 μ bar. In this case the nonlinearity is too weak to have influences upon the laser beam propagation. Consequently there is no self focusing, and the beam waist corresponds to the focus.

At the beam waist, the intensity reached $5.6 \times 10^{14} \text{W/cm}^2$, and **DI** plays a very important role. At the beam waist, the single and double ionizations are mixed, therefore the electron density $\rho_e = \rho_{X^+} + 2\rho_{X^{+2}}$; the free electrons with the largest kinetic energy (proportional to laser intensity) can easily transversely drift out of the plasma channel at the focal zone, and there is positive pole left after the transverse escape of the electrons. The longitudinal oscillating movement is weak. Consequently due to the coulomb attraction the oscillating currents exhibit different initial phases before and after the beam waist. The oscillation frequency of the currents is significantly diminished to $\sim 0.3 \text{GHz}$. It reflects the average electron density $\sim 10^8 / \text{cm}^3$ at the two ends of the plasma channel (except the beam waist); moreover, according to the ideal gas law, at 0.4 μ bar the neutral density ρ_{at} is around $\sim 10^{12} / \text{cm}^3$, therefore the ionization rate is $10^8 / 10^{12} = 0.1\%$. This makes a sound agreement with the Keldysh theory [Keldysh 1960, Keldysh 1965].

The oscillating current is not tilted compared with the one in the filament plasma. This implies that the current oscillation is mainly initiated by the positive pole at the beam waist. The influences of both laser force and the wake force on the plasma oscillating are weakened.

For the lase force:

1. Although electrons can gain the same level of the forward momentum from the laser field, the smaller electron density can not lead to a measurable forward oscillating current.

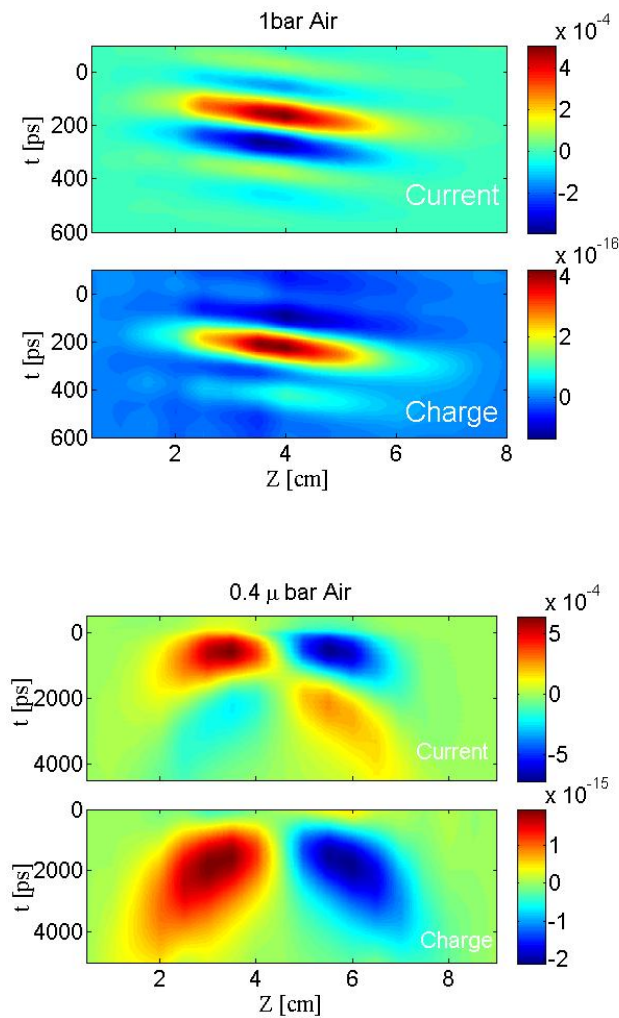


Figure 4.23: The current oscillation inside a filament plasma at 1 bar and 100 mbar Air and inside a non-filament plasma at 10 μ bar and 0.4 μ bar air. The blue and red color denote that electrons go backward and forward respectively. The current unit is A. The Charge unit is C. The laser pulse is 3 mJ , 40 fs. The focal length is 1 m

2. With a nanosecond oscillating period and prolonged λ_{MFP} , the electron motion is mainly transverse before the formation of the positive pole at the beam waist.

For the wake force:

1. The radius of the plasma column strongly depends on the position along the plasma channel. Out of the beam waist, the coulomb attraction in the wake of the laser pulse can seldom be formed due to the increasing radius.
2. The positive pole formed at the beam waist becomes predominant to attract the electrons at both ends of the plasma column (see Figure.4.24).

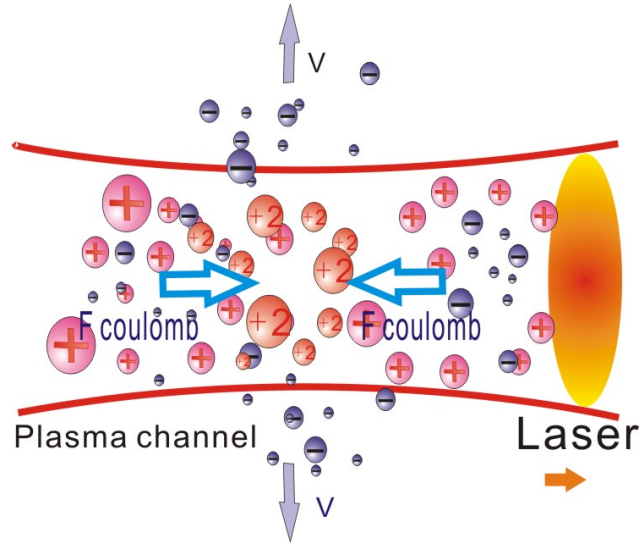


Figure 4.24: The illustration of the two forces inside the plasma channel.

Much differently from the filament plasma, the electron density of the non-filament plasma are highly uniformed in non filament case. To explore this feature, I plot the currents at different positions along the plasma channel in Figure 4.25. With the growth of the distance L_{w_0} between the measuring position and the beam waist, the current oscillating frequency decreases, while the current amplitude increase(see the top traces). This implies that electron density grows strongly with shortening L_{w_0} . The decrease of the current near the beam waist is due to the electron deficit caused by the lateral drift, so that at beam waist (position 4.5 cm) the longitudinal current goes to a minimum (see the bottom trace).

At a transient stage

There is a transient stage which mixes the features of the filament and non-filament plasma. At this stage, the physics of the plasma channel started to change. The weak nonlinearity and collision rate inside the plasma yield a different oscillating current.

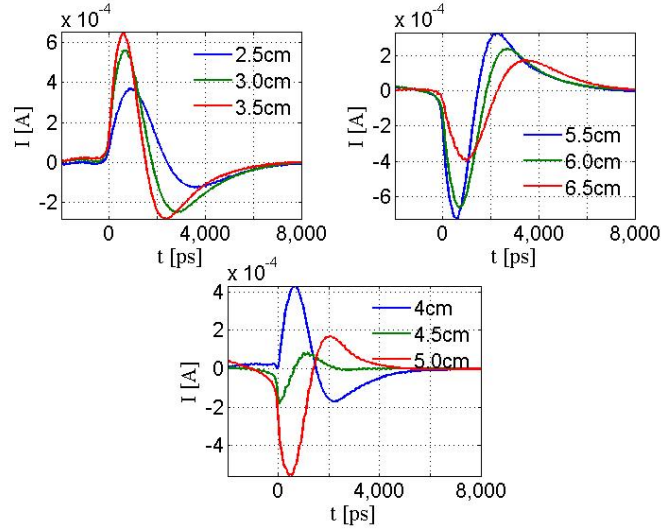


Figure 4.25: The current oscillation at different positions along the plasma channel 0.4 μbar air. The positive and negative value denote that electrons go forward and backward respectively. The laser pulse is 3 mJ, 40 fs, linearly polarized. The focal length is 1 m.

In 100 mbar air, the inelastic collision reduces, the wake force due to the lateral drift of early born electrons dominates inside the filament plasma. The influence of the laser force upon the electron oscillation is canceled. Therefore the initial electron movement is backward, and the current amplitude increases (see Figure 4.26(upper trace)).

By decreasing the gas pressure further down to 10 μbar , the oscillating current exhibits distinct features:

1. Electrons at the beginning of the plasma column are mainly forward after a weak initial backward motion; the backward motion of electrons gradually becomes dominant along the plasma channel, at certain position the electrons become moving backward only.
2. The backward motion of electrons is still delayed along the channel due to the speed of the ionization front $v \sim c$.
3. At certain time after the formation of the plasma channel, electrons at the two ends start to move towards the center of the plasma column.

These imply that at this stage, the coulomb force due to the lateral drift in the wake of the laser pulse, and the positive pole formed in the middle of the plasma column both govern the electron oscillation inside the plasma column. The wake coulomb force plays a leading role at first, subsequently when the positive pole is formed, this pole-induced attraction becomes major. A balance between self focusing and plasma defusing still exists near the geometrical focus zone, but generally the

radius of the plasma column varies along the plasma channel, therefore it is difficult to estimate the laser intensity along the plasma channel and the level of DI.

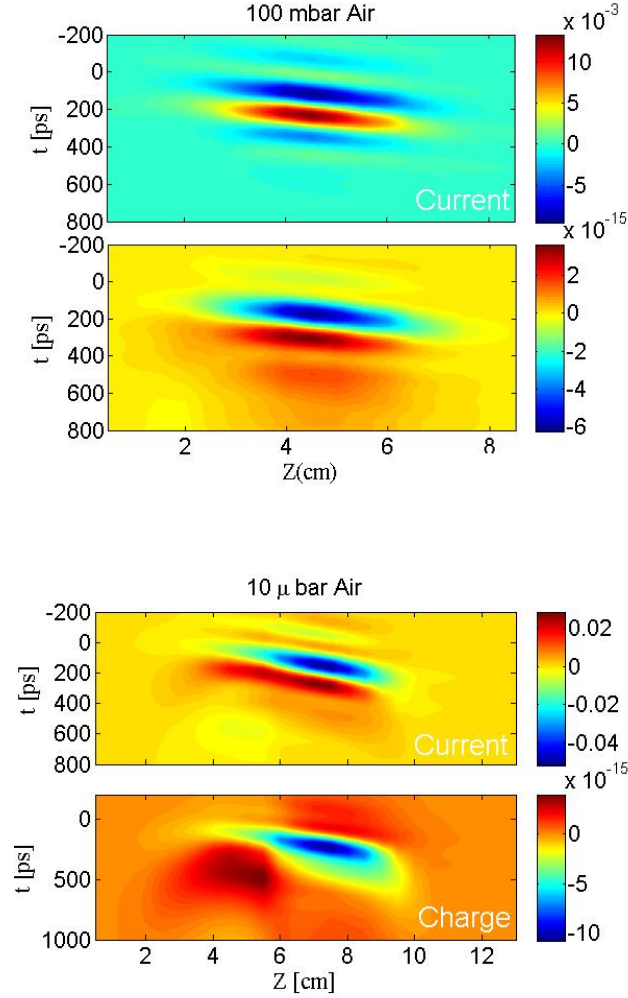


Figure 4.26: The current oscillation inside a plasma at 100 mbar and 10 μ bar air. The blue and red color denote that electrons go backward and forward respectively. The current unit is A. The Charge unit is C. The laser pulse is 3mJ, 40 fs. The focal length is 1 m.

4.4.2 Laser intensity dependence of the currents in a non filament plasma channel

To verify that the nonlinearity doesn't influence on the current oscillation, we compare the currents with various laser pulse energies with the linearly polarized laser pulse in Figure 4.27. The centers of the plasma channel are independent of the laser pulse energy. It implies that the laser beam always propagates in a linear

regime. The comparable plasma frequencies for each laser pulse energy reveal that electrons density doesn't change too much. The current amplitude and the length of the plasma grow with the increase of the pulse energy. There can be three possible factors to induce the growth of the current amplitude:

1. At the beam waist, the ratio X^{+2}/X^+ increases;
2. The ratio X^{+2}/X^+ stays the same, while the single ionization is reenforced;
3. Electrons gain more transverse momentum, which favors the formation of the positive pole.

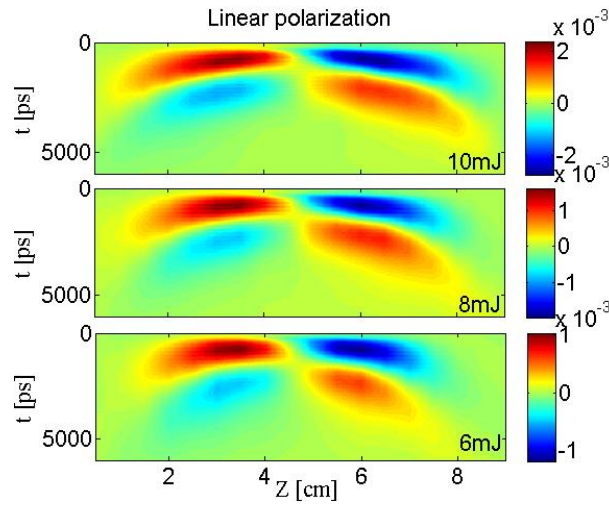


Figure 4.27: The current oscillation inside a filament plasma at $0.4\mu\text{bar}$ Air with different pulse energy. The blue and red color denote that electrons go backward and forward respectively. The current unit is A . The Charge unit is C . The laser pulse is 40 fs. The focal length is 1 m.

4.4.3 Laser polarization and gas pressure dependence of the currents in a non filament plasma channel

To study the laser polarization dependence of the oscillating current in dilute air, first I measure the currents with 10 mJ, 40 fs, circularly polarized laser pulse (see Figure 4.28) . Compared with linearly polarized laser pulse, the circularly polarized laser has a weaker single ionization rate and a smaller ratio of X^{+2}/X^+ ; fortunately, most of electrons gain more transverse momentum with circular polarization, so that it can facilitate the form of the positive pole at beam waist. The measured current amplitude is nearly a half of the one in linear case. This reflects that the single ionization rate and X^{+2}/X^+ are more effective to change the current amplitude, and they are higher with the linear polarized laser than those with circularly polarized laser.

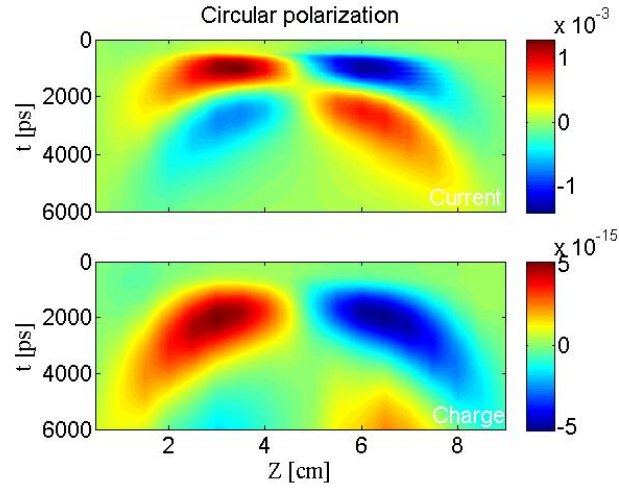


Figure 4.28: The current oscillation inside a filament plasma at $0.4 \mu\text{bar}$ air. The laser pulse is 10 mJ, 40 fs, circularly polarized. The focal length is 1 m

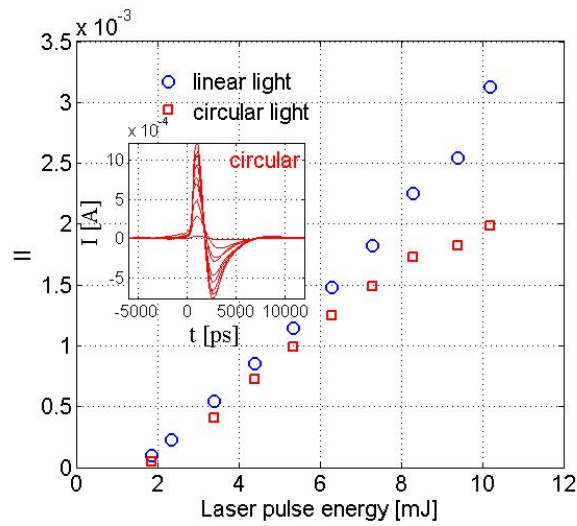


Figure 4.29: Difference between the maximum and minimum of currents as a function of the laser pulse energy at $0.4 \mu\text{bar}$ air. The laser pulse is 40 fs, linearly and circularly polarized. The focal length is 1 m. The insert figure is the currents with circularly polarized light at different pulse energies.

Furthermore, I fix the coil at 3 cm to measure the currents as a function of laser pulse energy for both linearly and circularly polarized light. We plot $II = I_{max} - I_{min}$ in Figure 4.29. For both linear and circular polarization, II goes up linearly with the increase of the laser pulse energy. Since the growth of II is mainly due to the increasing number of electrons, the larger slope of the curve for the linear case implies that the linearly polarized laser favors the electrons generation. Note that there is a threshold of the laser pulse energy for the oscillating current within the plasma channel. In our case, the threshold is around 2 mJ, below such energy there is no measured current signal within the plasma. This can be attributed to the fact that the double ionization only exists above certain laser intensity, without double ionization it is less effective to form a positive pole at the beam waist.

Lastly, at 4 cm (near the beam waist at 4.5 cm), we measure the current as a function of the gas pressure (see Figure 4.30). With the growth of the gas pressure, the current amplitude increases, meanwhile there is a negative current component emerging at the beginning of the oscillating currents (Figure 4.30 Top trace); compared with later current oscillation, this negative component is temporally shorter. The emergence of the initial negative component implies that the plasma shifts from non-filament stage to the transient stage, at which electrons are driven back by the wake force. There exist a turning point. Before the turning point, the plasma oscillation mainly was initiated by the positive pole at the beam waist; after the turning point, the wake force starts to play a dominant part for the plasma oscillation initially, and later on once the positive pole formed, the coulomb attraction towards the pole take over the wake force.

Figure 4.30 (Bottom trace) shows that II goes up linearly with different slopes before and after a turning point at $3\mu\text{bar}$, as we increase the gas pressure.

4.5 Controlled oscillating current with Bi-color laser pulse inside a filament

As we have discussed above, inside a filament there is a balance of forces: a laser force and a wake coulomb force. The coulomb force results from the lateral drift of electrons born at early time. With the Bi-color technique that the 800 nm laser beam passes through the thin BBO crystal, the lateral drift of electrons will be controlled by the superposition of the 400 nm and 800 nm electric field [Kim 2008]. The experiment set-up is shown in Figure 4.31. The $100\mu\text{m}$ thickness BBO is put after the lens, the current probe is fixed in the middle of the filament plasma. By displacing the current probe towards the lens, we measured the current signals.

Figure 4.32 shows the currents as function of displacement distance of BBO. With the changing of the displacement distance, the phase difference between 400 nm and 800 nm varied with 5.7 cm as a cycle. The current amplitude and its initial direction are also changed periodically. We contribute this controlled cycling variation of the currents to the periodical lateral drift caused by the overlapped electric field of the laser pulse. This transverse current model is well described in

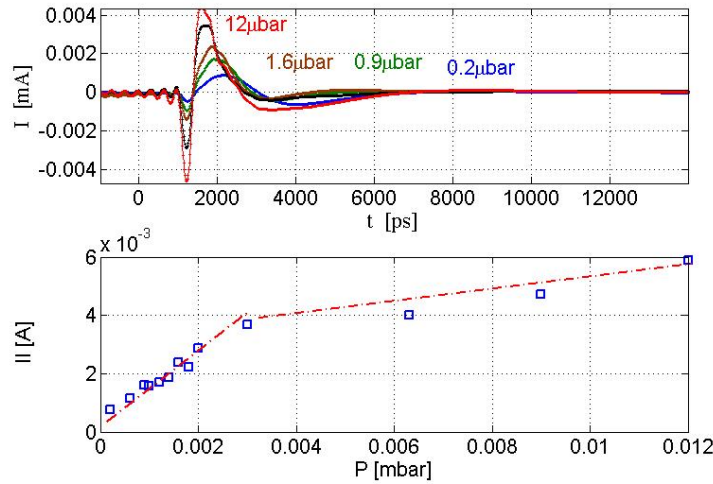


Figure 4.30: The oscillating currents are measured as a function of pressure at 3cm along the filament plasma. The top traces are the current signals, and the bottom trace is II as a function of the gas pressure. The laser pulse is 4 mJ, 40 fs, linearly polarized. The focal length is 1 m.

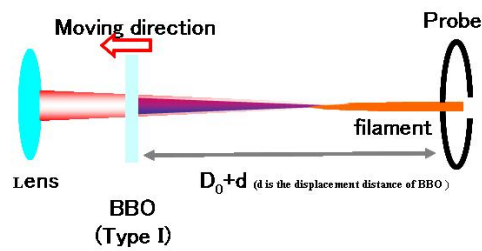


Figure 4.31: Experiment set-up for the control of the oscillating current. The laser pulse is focused by a 1 m focal length lens. The BBO crystal is 100 μm . The current probe is fixed in the middle of the plasma column. D_0 is the original distance between the BBO and the focus. d is the displacement distance.

[Kim 2009].

Note that there is still a puzzle: since the overlapped electric field only controls the coulomb wake force periodically, it is hard to explain that the current amplitude increases when the current initial direction is forward. Although the energy at 400 nm is only 1% of the laser pulse energy, it can be fully absorbed by electrons to gain more forward momentum. Further experiments are required for a complete understanding of this effect.

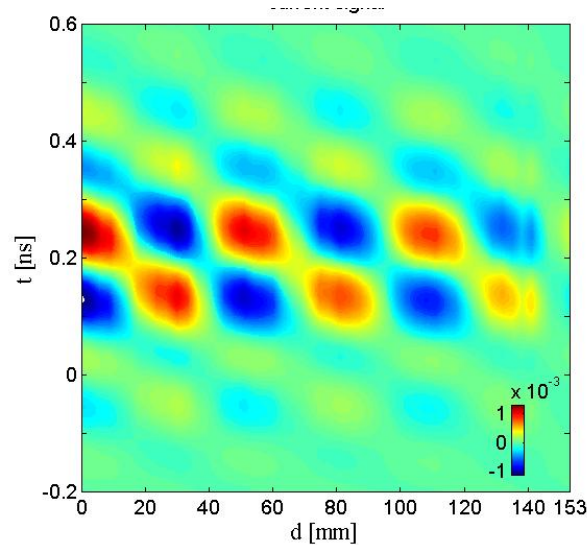


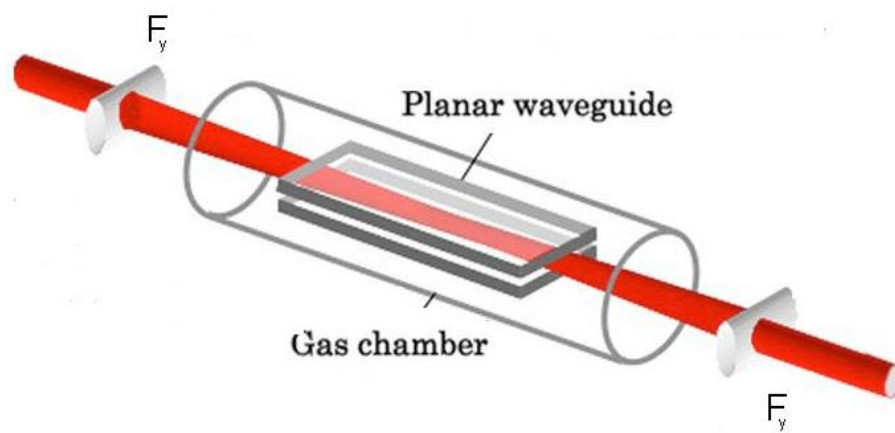
Figure 4.32: The measured current signals in the middle of the plasma column. The laser pulse before the BBO is 40 fs, 1.5 mJ , and linearly polarized. d is the displacement distance.

4.6 Conclusion on the oscillating current inside the laser induced plasma channel

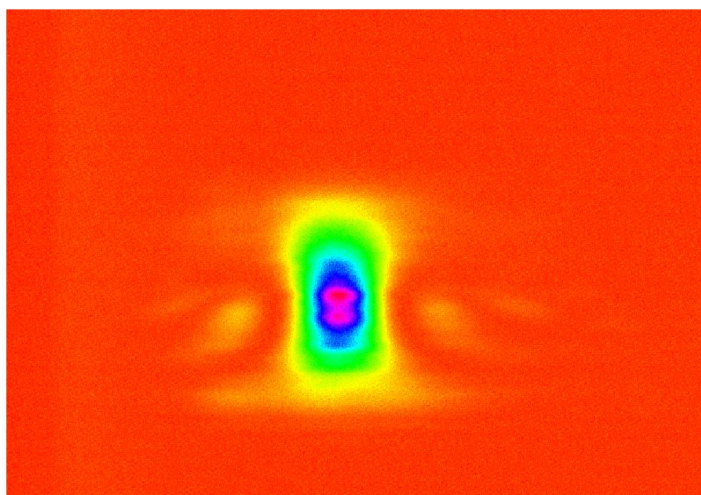
In this chapter, I have presented experimental results showing that the phase of plasma oscillations in filaments depends sensitively on several parameters. This behavior has been explained by a balance between two weak forces acting on the electrons after their birth. The first force is the laser force which is perceptible although the laser intensity inside filaments is far below the relativistic regime. The second force is due to the lateral expansion of the free electron cloud born earlier in the filament yielding an effective Coulomb wake field. A change of laser polarization, gases and gas pressures can alter the delicate balance between the two forces, forcing the initial plasma oscillation in either direction. Secondly, I have studied the laser induced plasma current in very dilute air. The currents do not depend on the laser forces any more. The positive pole formed in the center of the plasma channel dominates the plasma oscillation.

**Chapter 4. Measurement and control of longitudinal electric currents
84 in the wake of femtosecond laser pulses in gases**

Lastly, I have shown preliminary results obtained with Bi-color laser pulses. With the Bi-color laser pulses, we can control the oscillating current more easily. Further experiments will enable us to understand the driven mechanism better.



Chapter 2: Few-Cycle Pulses by External Compression



Few-Cycle Pulses by External Compression

Contents

5.1	Ultra short laser pulse internal and external compression	88
5.1.1	Few cycle laser pulse compression by a gas filled hollow fiber	89
5.1.2	Self-compression of optical laser pulses by filamentation . . .	90
5.2	Compression of ultrashort high energy laser pulses in planar hollow waveguides	93
5.2.1	Basic waveguide theory	94
5.2.2	Nonlinear pulse propagation in planar hollow waveguides . .	96
5.2.3	Simulations of laser pulse propagation in planar waveguide .	99
5.3	Experimental results of laser pulse compression in a planar waveguide	106
5.3.1	Experimental setup	106
5.3.2	Waveguide construction	107
5.3.3	Dependence of pulse compression on gas type and pressure .	109
5.3.4	Variation of pulse duration along the beam transverse dimension	110
5.3.5	Spatial phase and focusability	112
5.3.6	Optimization of input pulse duration	115
5.4	Generation of a filament plasma in helium gas with few-cycle pulses	116
5.5	Conclusion	117

In this chapter, for the laser pulse compression part I will first briefly introduce the history of ultrashort laser pulse development; secondly, I will summarize the methods of external few cycle laser pulse compression; finally I will cover another method: Planar Wave Guide, which has been recently studied in our group. The discussion will consist of two parts: theory and experiments, I try to provide an operational reference to people who might be interested to build such a similar laser compression system in their place.

By using the compressed laser pulse scheme, I have been able to generate a filament in 1 bar Helium. I will present both the calculation and the preliminary experimental results to confirm the filamentation in Helium.

5.1 Ultra short laser pulse internal and external compression

The present laser technology based on Ti:sapphire allows routinely reproducible optical pulses in the near infrared (IR) region to be obtained with a typical duration in the range 10 – 100 fs. After chirped pulse amplification (CPA) [Strickland 1985], the energy per pulse can reach from millijoule to several joules, depending on the repetition rate. There are strong incentives to reduce the pulse duration further, on the brink of the single cycle limit (3 fs at 800 nm). Near single cycle optical pulses are essential ingredients in attosecond physics both for the generation of XUV attosecond pulses [Paul 2001, Shon 2001], and for a short intense streaking pulse in the near IR [Yu 2004]. In addition, they are important in ultra-relativistic nonlinear optics, where the laser field is high enough to impart to protons a velocity close to the speed of light [Brueckne 1974]. The ultra-relativistic nonlinear optical regime requires peak laser intensities in the range of 10^{23}Wcm^{-2} . A shorter pulse could lead to drastic cost and size reduction of the laser facility, since most of the purchasing price of amplifier systems directly scales with the pulse energy.

Compression of ultrashort laser pulses to few and near-single-cycle durations is a crucial effort for certain applications of ultrafast physics and chemistry. Energetic infrared laser pulses of such short durations are important tools for high field physics [Krausz 009], acceleration of particles [Esarey 2009], frequency conversion to UV and XUV wavelengths [L’Huillier 995], as well as the generation of isolated attosecond pulses [Goulielmakis 008]. While the output energy of modern chirped pulse amplification (CPA) based femtosecond lasers can be as high as several joules, the pulse duration is generally above 20 fs. To obtain shorter pulse duration, external compression schemes are employed based on spectral broadening mostly via self-phase modulation (SPM). Two methods for spectral broadening and pulse compression are commonly applied: nonlinear propagation inside hollow capillaries filled with noble gas [Nisoli 1997] and self-guided propagation in noble gases [Hauri 2004]. In both cases spectral broadening is achieved due to strong SPM, either by external guiding through the capillary or by self-guiding in a filament.

As seen in Figure 5.1, until the end of the 1980s, ultrashort pulse generation was dominated by dye lasers, and pulses as short as 27 fs with an average power of 10 mW were achieved at a center wavelength of 630 nm [Valdmanis 1986]. External pulse compression ultimately resulted in pulses as short as 6 fs a world record result by C. V. Shank’s group that was not surpassed for about 10 years [Fork 1987]. This situation changed with the discovery of the Ti:sapphire laser. Today, pulses with only two optical cycles at FWHM (full-width half-maximum) at a center wavelength of 800 nm have been generated with Ti:sapphire lasers with more than 100 mW average output power [Eli 2001]. External compression resulted in pulses as short as 3.8 fs [Schenkel 2003]. The filled symbols indicate results directly achieved from a laser; open symbols indicate results achieved with additional external pulse compression.

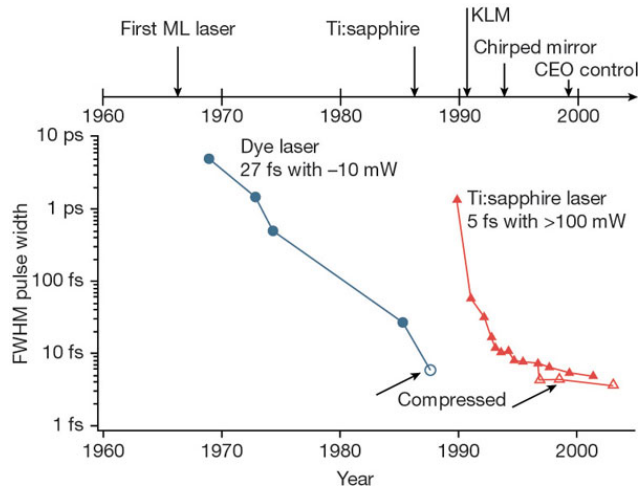


Figure 5.1: Improvements in ultrashort pulse generation since the first demonstration of a laser in 1960 . The figure is cited from [Keller 2003]

5.1.1 Few cycle laser pulse compression by a gas filled hollow fiber

The general scheme of light pulse compression is the following [Couairon 2005a]. The input pulse is first injected into a phase modulator, which broadens the pulse spectrum imposing a frequency sweep (in time). The spectrally broadened and chirped pulse is sent in a dispersive delay line, which rephases all the new frequency components generated by the phase modulation. Ideally, the dispersive delay line would introduce the opposite chirp on the pulse, thus resulting in the compression of the pulse to its minimum width, $1/\Delta\omega$, where $\Delta\omega$ is the frequency sweep imposed on the pulse in the first step. Further, to compress femtosecond pulses, an ultrafast phase modulator has to be used.

A fundamental requirement for pulse compression is that the Kerr effect is provided by a guiding nonlinear medium. The optical Kerr effect in a medium gives rise to an intensity-dependent change in the refractive index $\Delta n = n_2 I(t)$, where n_2 is the nonlinear index coefficient and $I(t)$ is the optical intensity. The self-induced intensity-dependent nonlinear phase shift experienced by an optical field during its propagation in a Kerr medium of length l is given by $\Delta\phi(t) = (\omega_0/c)n_2 I(t)l$ where ω_0 is the pulse central carrier frequency. The induced frequency sweep can be calculated as follows: $\Delta\omega = -d\Delta\phi/dt$. Around the central part of the pulse, where most of the energy is concentrated, the chirp is approximately linear. The region with linear chirp can be enlarged in the presence of dispersion in the Kerr medium of the same sign as $\Delta\phi$. To compress the spectrally broadened and chirped pulse, a dispersive delay line has to be used, characterized by a nearly linear group delay $T_g(\omega)$.

The hollow-fiber compression technique, which is based on propagation of laser pulses in a hollow fiber filled with noble gases, allows generating few-optical-cycle light pulses with energy in the mJ range. This technique is first demonstrated in

1997 [Nisoli 1997]. There are however several disadvantages with this technique. It requires meticulous alignment, is prone to hollow fibre damage, and is limited in the recompressed pulse energy since plasma ionization of the gas in the hollow fibre must be avoided. For the hollow Fiber scheme, the limitation is primarily due to damage of the capillary, especially at high repetition rate, and onset of ionization in the gas, recently the group OCP LOA ensta demonstrated that, with circular polarized laser pulse the energy reached nearly 1 mJ [Chen 2009], but the peak power was still roughly 0.2 TWcm^{-2} , which is still far from the peak power required in high intensity laser experiments. However, by applying a gradient of increasing gas pressure along the capillary the output energy could be increased [Suda 2005, Bohman 2008]. Recently a compression scheme utilizing the spectral blue-shift due to ionization of low pressure He in a hollow capillary was presented, yielding multi millijoule pulse energy at the expense of the efficiency, which is about 20% [Dutin 2010].

Perspectives in the use of the hollow-fiber technique are related to its energy scalability. The technique can be easily employed up to mJ-level laser pulses; the upgrade toward higher energies (tens of mJ) is hindered by gas ionization, thus appearing to be problematic. Furthermore, it is hard to control the laser pulses to keep good coupling with the capillary and avoid damage of the fiber entrance. Therefore to gain the few cycle laser pulse with pulse-energy extending to tens of mJ, a new way to compress the high energy pulse is necessary.

5.1.2 Self-compression of optical laser pulses by filamentation

Compression by filamentation simplifies the procedure above [Mysyrowicz 2008]. It was recognized during the tedious alignment of two successive hollow fibre compression stages that similar or even better results were obtained when the two hollow fibres were simply removed. These results were interpreted as being due to filamentation occurring in the argon inside the chambers containing the hollow chambers when a sufficiently intense ultrashort laser pulse propagates in a transparent medium. Two physical effects play major roles in the formation of a filament: the self-focusing effect due to intensity-dependence of the refractive index of the medium, and defocusing due to the formation of a plasma.

Both effects are schematically illustrated in Fig 5.2. It is important to stress that a filament is not a steady state. It has rich temporal dynamics involving also other effects such as group velocity dispersion, self-phase modulation, pulse self steepening and the Raman effect [Suda 2005]. Despite the complex spatio-temporal coupling that occurs from their combined action, the pulse takes the form of a narrow beam ($100 \mu\text{m}$) surrounded by a reservoir of laser energy. This reservoir feeds the filament core which becomes largely insensitive to initial conditions. It maintains high peak intensity around 10^{13} W/cm^2 [Hauri 2004] over a long distance, exceeding by orders of magnitude the Rayleigh length even if the underlying dynamics is complex and changing rapidly. In addition to the pulse spatial contraction, which is induced by the intensity dependence of the refractive index, broadening of the pulse spectrum arises due to the time variation of the refractive index ($n = n_0 + \Delta n_{\text{Kerr}(I)} =$

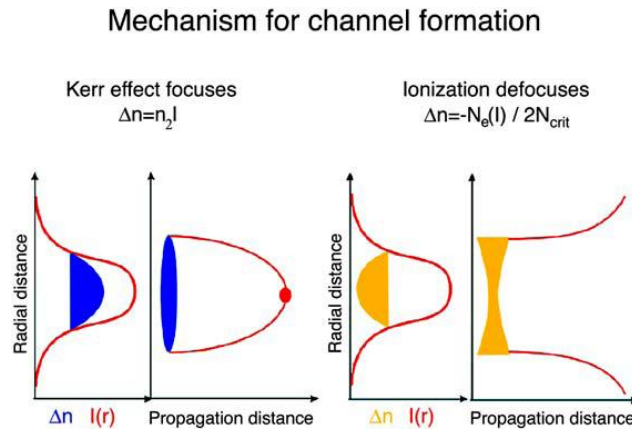


Figure 5.2: Mechanism for channel formation: For a typical beam intensity profile with a maximum on axis, the intensity dependent refractive index ($n = n_0 + \Delta n_{Kerr}(I) = n_0 + n_2 I$) acts like a succession of increasingly converging lenses. On-axis beam collapse is arrested by multi-photon ionization. This occurs typically at intensities around $10^{13} W/cm^2$ in gases, giving rise to a weakly ionized plasma with an electron density typically around $10^{16} cm^{-3}$, and a corresponding reduction of the local refractive index $\Delta n = -N(I)/2N_{cr}$. Here, $N(I)$ denotes the intensity dependent free electron density and N_{cr} , the density above which the plasma becomes opaque. Thus, multi-photon ionization acts as a strong regulating mechanism, limiting the beam intensity on axis and the dissipation of laser energy during propagation

$n_0 + n_2I$). The corresponding phase variation adds new frequency components to the spectrum: red frequency components on its ascending, and blue components on the descending side. This results in a variation of the instantaneous frequency with time (chirp). The addition of new frequencies develops to the point of creating a quasi-continuum extending over the entire visible spectrum and into the infrared. This opens the possibility to obtain shorter pulses, by a suitable retardation of the red components with respect to the blue ones. One additional aspect of femtosecond filamentation, is pulse self-compression. The different nonlinear effects occurring in filamentation lead to an important restructuring of the pulse time profile. Some of these effects, such as self-focusing, pulse self-steepening, and self-phase modulation, act instantaneously.

These effects tend to accumulate laser energy to the ascending part of the pulse, whereas the time-delayed effects, such as photo-ionization and the Raman effect, tend to cut off its trailing part. Their combination eventually leads to the formation of pulses that are significantly shorter than the incident pulse. One important facet, previously overlooked, is the fact that pulse reshaping by filamentation can be effective down to the fundamental limit of nearly one optical cycle.

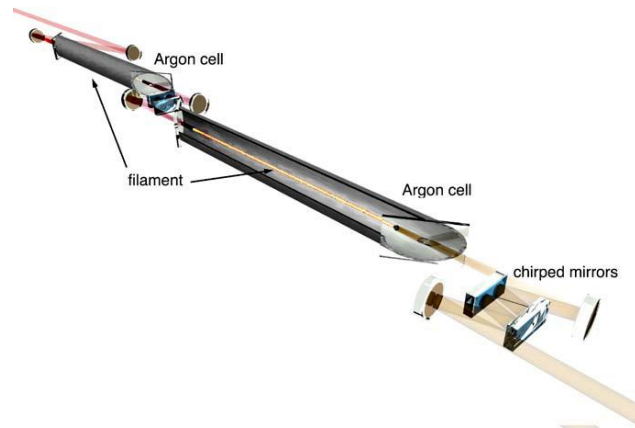


Figure 5.3: Two stages external compression system.

In 2004, Haury et al. found that optimum pulse shortening from 43 fs to 5.7 fs could be achieved by using two successive gas cells at pressures of 840 mbar and 700 mbar of argon [Hauri 2004], as shown in Fig 5.3. The CEO-phase-locked input pulse with an energy of 0.84 mJ was loosely focused into the first cell where it generated a 10–15 cm long filament roughly in the center of the cell, as estimated from the length of the scattered broadband continuum. The emerging spectrum was recompressed with chirped mirrors, resulting in a shortening by a factor four while retaining 94% of the input energy. Sending the 10.5 fs pulse into the second gas cell, another 15 – 20 cm long filament was formed, leading after chirped-mirror recompression, to a 5.7 fs pulse with 45% of the initial pulse energy, i.e. 0.38 mJ. Figure 5.4 shows the temporal intensity profile of compressed pulses as obtained after the second cell. The full width at half maximum (FWHM) pulse duration of 5.7 fs corresponds to

2.1 optical cycles. The associated spectrum and spectral phase are given in (b). Assuming a flat spectral phase in (b), theoretically the pulse duration would reach 1.7 fs.

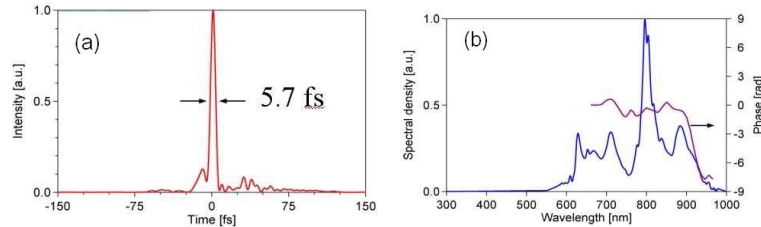


Figure 5.4: Pulse self shortening by filamentation in argon gas cells. (a) Temporal profile (left axis). (b) Spectral intensity and phase (right axis).

By filamentation, few cycle laser pulses can be reliably achieved. This technique presents a robust and simple alternative to hollow fiber pulse compression. The following aspects are unique to this technique: the filamentary propagation has been shown to yield an output pulse with a flat phase front, a feature confirmed by the experiments simulations. Furthermore, because filamentation is arrested by multi-photon ionization, a process scaling as intensity to the eleventh power in argon, a very effective intensity clamping is achieved. However, the shortcoming for filamentation is still obvious: the laser pulses energy can not go up to more than mJ. The high harmonics generation, which requires high pulse energy, is still crippled, therefore there is a need for a more sound way to compress the laser pulse.

5.2 Compression of ultrashort high energy laser pulses in planar hollow waveguides

Nurhuda *et al.* recently proposed the compression of ultrashort laser pulses based on SPM inside a gas-filled planar hollow waveguide [Nurhuda 2006]. In this concept the beam is guided only in one transverse direction. The size of the beam in the perpendicular transverse direction can be freely adapted to adjust the intensity inside the waveguide to a level for efficient SPM but still below excessive nonlinear ionization. This method offers superior energy scalability as compared to hollow capillaries and filamentation [Nurhuda 2006]. The technique was experimentally demonstrated first by Chen *et al.* [Chen 2008]. However, in these experiments, it was realized that, in practice, the energy up-scalability of the planar waveguide scheme requires more attention. Particularly, small-scale self-focusing causes strong modulations in the spatial beam profile along the free waveguide dimension; the beam thus tends to break up into individual filaments along this dimension. Because of this limitation, the early experiments yielded pulse energies of only ≈ 2 mJ with durations of 12 fs [Chen 2008]. In a more recent work it was shown that by carefully choosing experimental parameters, such as waveguide length and gas pressure, a trade-off between

spatial mode degradation due to small-scale self-focusing and spectral broadening can be found, allowing significant temporal compression at focusable output beam quality [Akturk 2009]. In these experiments, output pulse energy of 8.1 mJ and duration of 13.6 fs were obtained. Comprehensive simulations of nonlinear propagation in the waveguide, including the interactions in the spatial profile, indicated good agreement with the experiments and suggested the possibility of extending the method to 100 mJ energy levels [Arnold 2009].

In present results and a detailed discussion of several practical aspects as well as the parameters dependence of the pulse compression scheme based on SPM in a planar hollow waveguide. Note that this planar compression scheme has been realized mainly by the former colleagues S. Akturk and C. Arnold, and subsequently improved by the former colleague S. Chen and me. The discussion includes both experimental and theoretical considerations. In the experimental part we evaluate various options of assembling planar hollow waveguides, characterize the pulse compression for different types of gases and gas pressures, evaluate the uniformity of pulse compression along the transverse direction, and discuss the spatial intensity and phase of the output beams and their effect on the focusability. In the theoretical part we thoroughly present the model employed to simulate nonlinear pulse propagation inside the waveguide. We compare the simulations with the experimental results and discuss possible tuning of experimental parameters for energy up-scalability.

5.2.1 Basic waveguide theory

In this section we shortly recall the basic theory of linear waveguide propagation. A planar hollow waveguide, guiding laser radiation in a gas filled gap between two pieces of glass, is intrinsically leaky. The attenuation depends on the order of the guided mode, the separation of the glass plates, and the laser polarization. The guided modes satisfy the Helmholtz equation and boundary conditions on the glass plates. They can be approximated as sine $V_{p=2m}(x) = \sin(p\pi x/2a)$ and cosine $V_{p=2m-1}(x) = \cos(p\pi x/2a)$ leaky waveguide modes with vanishing field at the glass surface [Laakmann 1976], where p and m are integer numbers. Here x is the transverse coordinate in the guided direction, y is the transverse coordinate in the free dimension, z is the propagation direction along the waveguide, and $2a$ is the separation of the waveguide. See figure 5.5 for a sketch of the coordinate system with respect to the waveguide.

The waveguide modes form an orthogonal basis with:

$$\frac{1}{a} \int_{-a}^a V_p(x) V_{p'}(x) dx = \delta_{pp'} \quad (5.1)$$

The modes can be distinguished in even and odd order depending on the mode index p . The lowest order odd mode with index $p=1$ is also termed fundamental waveguide mode. See figure 5.6(a) for a plot of the lowest order modes. The real part β_p and imaginary part α_p of the mode dependent wave number $k_p = \beta_p + i\alpha_p$

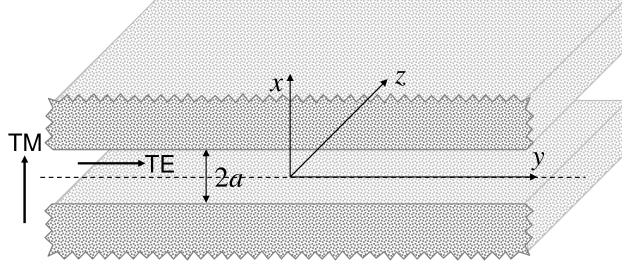


Figure 5.5: Coordinate system for the planar hollow waveguide. The arrows denote the polarization directions for TE and TM guided modes.

can be derived from perturbative analysis [Marcatili 1964, Yariv 1989]:

$$\beta_p(\omega)_{\text{TE, TM}} = k(\omega) \sqrt{1 - \left(\frac{p\pi}{2k(\omega)a} \right)^2} \quad (5.2)$$

$$\alpha_p(\omega)_{\text{TE}} = \left(\frac{p\pi}{2k(\omega)a} \right)^2 \frac{1}{a \sqrt{n_g^2 - 1}}, \quad (5.3)$$

$$\alpha_p(\omega)_{\text{TM}} = \left(\frac{p\pi}{2k(\omega)a} \right)^2 \frac{n_g^2}{a \sqrt{n_g^2 - 1}} \quad (5.4)$$

Here $k(\omega)$ is the frequency dependent free space wave number for a particular gas inside the waveguide. Equations (5.2) define the mode dependent dispersion $\beta_p(\omega)$ and absorption $\alpha_p(\omega)$ relations, respectively. Note that depending on the gas pressure and the waveguide separation, the group velocity and the group velocity dispersion can be significantly different from the free space dispersion relation. The real part of the wave number does not depend on the laser input polarization. It is the same for both TE and TM modes (see figure 5.5). The attenuation however is by a factor of n_g^2 greater for TM modes, where n_g is the refractive index of the glass material [Laakmann 1976]. The attenuation is proportional to the square of the mode index p . Higher order modes are therefore damped much more strongly than the fundamental mode ($p = 1$). See figure 5.6(b) for the relative attenuation of modes of different orders along the waveguide.

We will now analyze the coupling of a laser beam focused with a cylindrical mirror to the entrance of the planar hollow waveguide. The incoming laser field $E(x, y)$ is decomposed into waveguide modes with amplitudes $A_p(y)$ as it enters the waveguide:

$$A_p(y) = \frac{1}{a} \int_{-a}^a V_p(x) E(x, y) dx \quad (5.5)$$

For the sake of simplicity we assume that the focal beam profile is Gaussian in x (guided dimension) and uniform in y (free dimension) $E(x, y) = E_0 \exp\left(-\frac{(x - x_0)^2}{w^2}\right)$ with flat spatial phase. If the focused beam is centered exactly in the middle of the waveguide gap $x_0 = 0$, symmetric (odd order) modes are

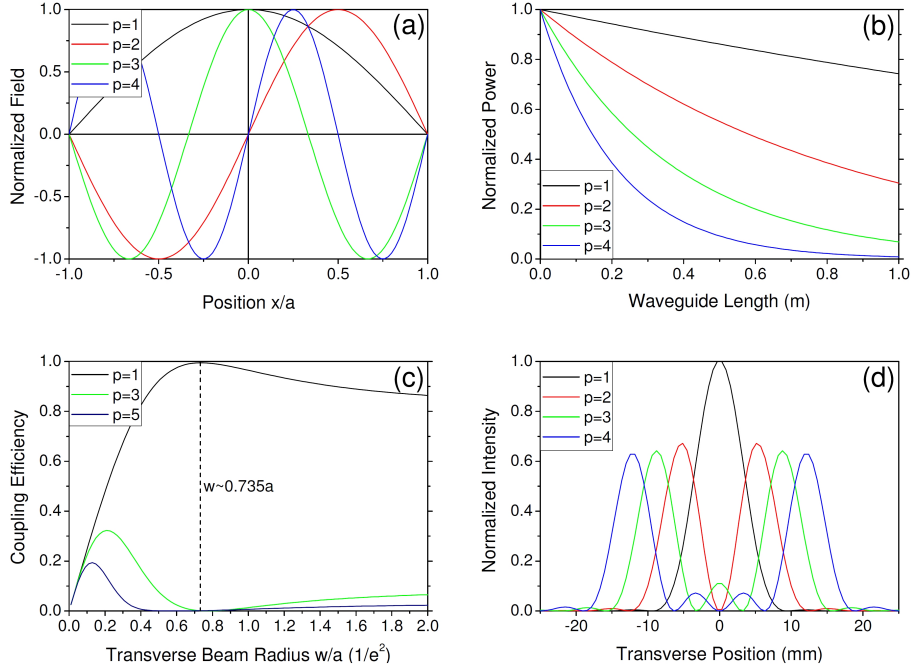


Figure 5.6: (a) Even and odd waveguide modes. (b) Attenuation for different modes. (c) Coupling efficiency for odd order modes. (d) Far field intensity patterns of guided modes (1 m distance).

excited only. The coupling efficiency depends on the Gaussian width w of the beam compared to the half width a of the waveguide. In figure 5.6(c) we plot the coupling efficiency to the first three odd order modes as a function of Gaussian width. Optimized coupling conditions are found for $w \approx 0.735a$. In this case about 99.4% of the power falling inside the waveguide ($-a \leq x \leq a$) and 98.8% of the total power is coupled to the fundamental waveguide mode ($p=1$). Additionally, the first higher order odd mode ($p=3$) is damped nine times stronger than the fundamental mode. Thus higher order mode content is efficiently cleaned in the waveguide. Nonetheless, if the focus is shifted from the center of the waveguide or exhibits asymmetry, also even order modes are excited, whereas the lowest order even mode ($p=2$) is damped only four times stronger than the fundamental mode. Finally, figure 5.6(d) shows the far field (1 m distance) intensity profiles of the lowest order modes for a waveguide separation of $2a = 127 \mu\text{m}$.

5.2.2 Nonlinear pulse propagation in planar hollow waveguides

In the preceding section the linear properties of planar hollow waveguides were discussed. However, as in the experiments the waveguide is applied to nonlinearly broaden the spectrum of injected high energy ultrashort laser pulses, in order to subsequently compress the pulses to shorter duration, the propagation inside the waveguide is intrinsically nonlinear. In the linear regime individual modes, once ex-

cited at the entrance of the waveguide, propagate independently from each other. In contrast, in the nonlinear regime waveguide modes exchange energy due to nonlinear coupling effects, such as Kerr self-focusing and plasma defocusing due to ionization.

In order to numerically describe nonlinear ultrashort pulse propagation inside a gas-filled planar hollow waveguide, a unidirectional nonlinear envelope equation (NEE) (5.6) is applied [Brabec 1997, Couairon 2007, Kolesik 2004]. This type of equation is known to be valid for pulses down to the single cycle regime [Brabec 1997]. Equation (5.6) was derived from the nonlinear Helmholtz equation and the method proposed by Feit and Fleck was used to introduce unidirectional propagation [Feit 1988].

$$\partial_z \tilde{E}(k_T, z, \omega) = i\Delta k_z(k_T, \omega) \tilde{E}(k_T, z, \omega) + \frac{1}{k_z(k_T, \omega)} \mathcal{F}\{N(x, y, z, t)\} \quad (5.6)$$

Here $\tilde{E}(k_T, z, \omega)$ is the 3-dimensional Fourier transform of the electric field envelope $E(x, y, z, t)$, $k_T = \sqrt{k_x^2 + k_y^2}$ is the transverse wave number and $k_z(k_T, \omega) = \sqrt{k^2(\omega) - k_T^2}$ is the wave number in the propagation direction. The linear part of (5.6) describes the effects of diffraction, nonparaxiality and group velocity dispersion via a longitudinal wavenumber shift $\Delta k_z(k_T, \omega) \equiv k_z(k_T, \omega) - k_0 - 1/v_g(\omega - \omega_0)$, originating first from the fact that the carrier wave $\exp(ik_0z)$ is canceled out in the transformation of the unidirectional propagation equation for the electric field into a nonlinear envelope equation, and second from the description of the propagation in the local reference frame moving at group velocity $v_{g,0} = (dk(\omega)/d\omega|_{\omega=\omega_0})^{-1}$ of the propagated pulse, where ω_0 is the center frequency. In the paraxial regime ($k_T \ll k(\omega)$), which is a well satisfied approximation in the context of our work, the explicit consideration of the k_T -dependence of k_z is not essential [Kolesik 2004]. The following approximations were thus made: $k_z \approx k(\omega) - \frac{k_T^2}{2k(\omega)}$ for the linear part and $k_z \approx k(\omega)$ in front of the nonlinear part. The dispersion relation $k(\omega) = \frac{\omega}{c}n(\omega)$ is calculated from the refractive index data of particular gases [Dalgarno 1966]. Therefore no expansion of the dispersion around the center frequency is required. Nonlinear contributions to pulse propagation in (5.6) are gathered in $N(x, y, z, t)$, where \mathcal{F} denotes a 3-dimensional Fourier Transform. We perform the following approximation $\frac{1}{k_z} \mathcal{F}\{N(x, y, z, t)\} \approx \frac{1}{k(\omega)} \mathcal{F}\{N(x, y, z, t)\} = \mathcal{F}\{N'(x, y, z, t)\}$ and write:

$$\begin{aligned} N'(x, y, z, t) = & \frac{i}{2}\varepsilon_0 n_0 n_2 \omega_0 T |E(x, y, z, t)|^2 E(x, y, z, t) - \frac{i}{2}\sigma \tau_c \omega_0 T^{-1} \rho E(x, y, z, t) \\ & - \frac{1}{2} \left(\sigma \rho + U_i \frac{W_{PI}(I)}{I} (\rho_{at} - \rho) \right) E(x, y, z, t) \end{aligned} \quad (5.7)$$

The first term in (5.7) describes self-focusing and self-phase modulation due to the optical Kerr effect. We neglect the retarded Kerr response, since only noble gases will be considered. Here c is the vacuum speed of light, ε_0 is the dielectric permittivity, and $n_2 = 0.98 \times 10^{-19} \text{ cm}^2 \text{ W}^{-1}$ is the nonlinear refractive index for Ar at atmospheric pressure [Tempea 1998]. The second term in (5.7) stands for refraction due to generated free electrons of density $\rho(x, y, z, t)$. Here $\sigma = e^2/m_e c \varepsilon_0 n_0 \tau_c \omega_0^2$

is the cross section for inverse Bremsstrahlung in the well verified limit of a collision frequency much smaller than the laser frequency [Yablonovitch 1972a], m_e is the free electron mass. The collision time $\tau_c = 190$ fs denotes the mean free time between collisions of free electrons with heavy particles (atoms) in Ar at atmospheric pressure [Couairon 2006]. The last term in (5.7) accounts for absorption due to inverse Bremsstrahlung and nonlinear photoionization. Here U_i denotes the ionization potential and $\rho_{\text{at}} = 2.5 \times 10^{25} \text{ m}^{-3}$ is the atomic density at atmospheric pressure and room temperature. The rate of nonlinear photoionization $W_{\text{PI}}(I)$ is calculated from the generalized Keldysh PPT theory [Keldysh 1965, Perelomov 1966], where $I(x, y, z, t)$ is the electric field intensity. The T-operator in (5.7) accounts for self-steepening effects; it is most conveniently applied in its frequency space representation $\tilde{T} = \omega/\omega_0$. In order to calculate the density of generated free electrons $\rho(x, y, z, t)$, the following rate equation is solved in parallel with (5.6):

$$\frac{\partial \rho(x, y, z, t)}{\partial t} = W_{\text{PI}}(I) (\rho_{\text{at}} - \rho) + \frac{\sigma}{U_i} I \rho \quad (5.8)$$

Equation (5.6) describes nonlinear optical pulse propagation in free space. To adapt it to nonlinear propagation inside a planar hollow waveguide, we make use of the two different but equivalent representations of the laser pulse inside the waveguide, either as the electric field envelope itself or as the sum of the guided modes $A_p(y, z, t)$.

$$E(x, y, z, t) = \sum_{p=1}^{\infty} V_p(x) A_p(y, z, t) \quad (5.9)$$

where for convenience, we chose the carrier of the fundamental mode $\exp(i\beta_0 z)$ with $\beta_0 = \beta_{p=1}(\omega)|_{\omega=\omega_0}$ as the reference carrier wave to define the mode envelopes. The electric field envelope defined in (5.9) thus differs from that of (5.6) by a factor $\exp(i(\beta_0 - k_0)z)$ and each mode envelope implicitly includes a longitudinal phase shift $\beta_p - \beta_0$ responsible for mode beatings. We can move from one representation to the other by either projecting the electric field to the modes via (5.5) or by reconstructing the field from the modes using (5.9). If we insert the 2-dimensional Fourier transform $\tilde{A}_p(k_y, z, \omega)$ of the guided mode representation with wave number $\beta_p(\omega)$ and absorption $\alpha_p(\omega)$ in (5.6), the following propagation equation is obtained:

$$\partial_z \sum_{p=1}^P \tilde{A}_p(k_y, z, \omega) V_p(x) = i \sum_{p=1}^P (\Delta\beta_p(k_y, \omega) + i\alpha_p(\omega)) A_p(k_y, z, \omega) V_p(x) + \mathcal{F}\{N'(x, y, z, t)\} \quad (5.10)$$

In this context \mathcal{F} denotes just a 2-dimensional Fourier transform, since decomposition in transverse wave numbers for the guided dimension (x) is not necessary and $\Delta\beta_p(k_y, \omega) \equiv \sqrt{\beta_p^2(\omega) - k_y^2} - \beta_0 - 1/v_{g,0}(\omega - \omega_0)$. The frequency dependence of the wave number $\beta_p(\omega)$ and absorption coefficient $\alpha_p(\omega)$ is fully known and can be directly applied for each mode without approximation. The reference frame now moves at the group velocity $v_{g,0} = (d\beta_{p=1}(\omega)/d\omega|_{\omega=\omega_0})^{-1}$ of the fundamental mode,

since it propagates fastest. Higher order modes fall behind along propagation inside the waveguide.

We numerically solve (5.10) in a split-step scheme, where the linear and nonlinear parts are propagated alternately. The linear step can be exactly performed by propagating the 2-dimensional Fourier Transform of each mode $\tilde{A}_p(k_y, z, \omega)$ in mode space as $\tilde{A}_p(k_y, z + \Delta z, \omega) = \tilde{A}_p(k_y, z, \omega) \exp(i(\Delta\beta_p(k_y, \omega) + i\alpha_p(\omega))\Delta z)$. The nonlinear step is evaluated in normal space except for T-operators, which are applied in frequency space. $N'(x, y, z, t)$ was not rederived using $\beta_{p=1}(\omega)$ instead of $k(\omega)$. This is consistent with the range of approximations made before, preserving the lowest order frequency dependence. Between a linear and a nonlinear step the electric field $E(x, y, z, t)$ is reconstructed from the modes, then a nonlinear step is performed, and subsequently the field is projected back on the modes to perform the next linear step. Note that this approach of continuously going back and forth between normal space and mode space representation is strictly different from traditional coupled mode theory [Tempea 1998, Courtois 2001], where the propagation equation is integrated in mode space only. In coupled mode theory usually only the coupling between the fundamental and higher order modes is considered, but not the coupling between individual higher order modes. In contrast, this scheme intrinsically includes the coupling between all modes involved. Additionally, it is much more convenient to numerically implement than coupled mode theory. In order to properly describe beatings between different guided coupled modes with different wave numbers and group velocities, the maximum possible step-size is limited to $\Delta z \ll 2\pi/(\beta_1 - \beta_P)$. Here P is the index of the highest mode excited with significant amplitude and $(\beta_1 - \beta_P)^{-1}$ is the beating length between the fundamental mode and the mode of order P .

5.2.3 Simulations of laser pulse propagation in planar waveguide

In latter experiments, an almost fourfold compression of energetic ultrashort laser pulses to 10.1 fs at 80% energy throughput focusable to relativistic intensity was presented, based on the planar hollow waveguide compression scheme. The energy level is superior compared to the use of filamentation or hollow capillaries for compression. Two main aspects of the planar hollow waveguide compression scheme were identified, which have to be carefully considered in applications. First, the deterioration of the transverse output mode in the free waveguide dimension, limiting the shortest possible pulse duration, and second a reduced focusability due to nonuniform spectrum and duration as well as a retarded spatial phase also in the free dimension. Both aspects can be addressed using the waveguide propagation model based on equation (5.10) presented in the previous section.

Numerical simulations of pulse compression in planar hollow waveguides were published in an earlier paper (Arnold *et al.* [Arnold 2009]), showing convincing general agreement between experimental compression results and simulations based on (5.10). This was illustrated in terms of comparing three different quantities for measured and simulated compressed pulses (see figure 2 in [Arnold 2009]): the temporal

compressed pulse profiles, the spectrograms for SHG FROG, as well as the output mode. The experimental results used in this comparison can be found in Akturk *et al.* [Akturk 2009], where we reported a compressed pulse duration of 13.6 fs at an output pulse energy of 8.1 mJ. These results were obtained with the same experimental setup, as described in figure 5.12, with a waveguide made from fused silica (see section 5.3.2), at 1.5 atm of Ar, and 127 μm separation. In [Arnold 2009] we used these parameters to carefully adapt the numerical model to the experimental results. In order to obtain good agreement between simulations and experiments, the initial conditions for the model were chosen to match the experimental conditions as closely as possible. In particular, instead of using a perfect Gaussian initial pulse, a measured temporal profile (Grenouille, Swamp Optics) was implemented. Furthermore the transverse structure of the output mode, observed along the free waveguide dimension (see *e. g.* figure 5.16(a)), was well reproduced numerically, when a measured transverse beam profile was used as an initial condition. The difference between applying an ideal transverse beam profile and a measured profile is illustrated in figure 5.7, where we compare the fluence in the free waveguide dimension for a perfect Gaussian initial profile (a) and the actual measured beam profile (b). For the sake of simplicity we choose the same parameters as in [Arnold 2009] for the simulations throughout this paper, although the output pulse energy was increased and the compressed duration decreased simultaneously (see section 5.3) as compared to [Akturk 2009]. It is evident that the distinct transverse structure in figure 5.7(b) emerges from small-scale self-focusing of initial beam imperfections and noise. The dotted line in both plots indicates the length of the waveguide (21 cm) used in the experiments. For the case in figure 5.7B the waveguide length is obviously close to the maximum permissible propagation distance at this level of nonlinearity. Shortly after the beam finally breaks up into individual filaments, not usable for applications. For figure 5.7(a) however the distance of stable transverse propagation is greatly overestimated. The beam indeed breaks up into transverse filaments after about 80 cm due to modulational instability emerging from numerical noise. Any real laser beam would of course break up before.

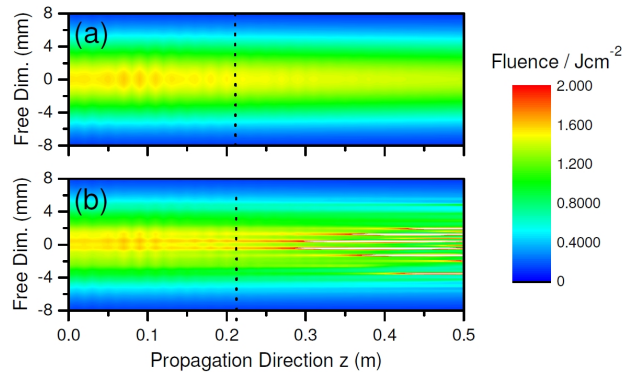


Figure 5.7: Fluence along the free waveguide dimension with an ideal Gaussian transverse input beam profile (a) and a measured beam profile (b).

Having identified that the transverse instability due to small-scale self-focusing limits the maximum propagation distance in the waveguide at a given level of nonlinearity, a numerical stability analysis was performed in order to investigate possible scalability to higher pulse energy. Since the scalability to high pulse energy is the striking advantage of the hollow planar waveguide compression scheme compared to hollow capillaries and filamentation, we will recall this aspect here. In order to identify a regime of stable transverse propagation inside the waveguide, which can be utilized for pulse compression, we evaluate the length scales for instabilities to be avoided, such as self-focusing of the entire beam and disintegration of the transverse profile due to small-scale self-focusing and modulational instability, respectively. The regime of stable propagation is illustrated in figure 5.8. Propagation in the waveguide is stable, when the length for self-focusing of the entire beam (blue dotted line) is much longer than the length of the waveguide and when the length for transverse disintegration of the mode due to modulational instability is also longer than the waveguide. A derivation of an analytic formula for the 1-dimensional self-focusing length is given in [Arnold 2009]. Along the y -direction in figure 5.8 the distance after which instabilities were numerically observed is plotted, either for a perfect input transverse beam profile (black triangles) or for the measured beam profile of our laser (red circles). The length of the experimental waveguide is indicated as dotted line. To scale to higher pulse energy we gradually increase the beam size w_y in the free waveguide dimension (bottom x -axis) at constant intensity. The pulse energy (top x -axis) and total power in the waveguide scale linearly with the beam size. The measured transverse beam input profile is simply scaled with the transverse beam size w_y . The other numerical parameters, such as intensity, pulse duration, waveguide separation, choice of gas (Ar), and pressure remain unchanged, since it was experimentally confirmed that this set of parameters corresponds to a good compression regime with well-behaved mode dynamics. It is evident from figure 5.8 that the maximum distance of stable propagation is much shorter, when a measured transverse beam profile is considered instead of a perfect beam. Indeed, the quality of the input beam to the waveguide determines the maximum distance of stable propagation. The shaded area indicates the regime of stable propagation, determined by our experimental beam profile. For small transverse beam size w_y the stability region is limited by self-focusing of either the whole beam or individual structures in the beam profile. For larger beam size the maximum propagation distance is limited by modulational instability emerging from small inhomogeneities and noise in the beam profile [Bespalov 1966]. The solid star in the stability region indicates the position of the experimental compression published in [Akturk 2009] and numerically simulated. This combination of parameters is located very close to the boundary of the stable region. For slightly longer propagation distance the beam breaks up into individual filaments (also see figure 5.7), unusable for compression.

When modulational instability determines the stability regime ($w_y \gtrsim 20$ mm), the maximum propagation distance can be associated with a specific value of the B-integral $B \approx k_0 I_0 n_2 p_g z$, where I_0 is the intensity in the waveguide, p_g is the pressure in atm, and z is the waveguide length. While for the experimental conditions (solid

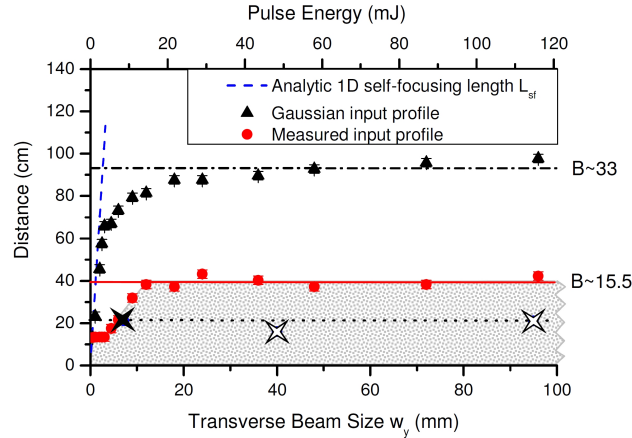


Figure 5.8: Maximum distance of stable waveguide propagation vs. transverse beam size (free dimension) and pulse energy, respectively. The shaded area indicates the stability region for the measured input profile of our laser.

star) a value of $B \approx 8$ could not be exceeded, for larger beam size a B-value of about 15.5 defines the boundary of the stable region, allowing for larger compression ratios.

The stability analysis for figure 5.8 has been performed for a constant level of nonlinearity, keeping the nonlinear refractive index n_2 (fixed by the choice of the gas), the pressure p_g , and the intensity I_0 constant. In principle, a specific value of the B-integral can also be obtained with different combinations of parameters. Note that the stability region illustrated in figure 5.8 remains valid, if $I_0 n_2 p_g = \text{const}$, as long as the intensity level remains below excessive ionization. If however a different pulse duration is considered, only the bottom x -axis (beam size w_y) remains valid.

Applying the above considerations we indicated two additional points in the stability diagram (open stars): one corresponding to the compression of pulses at the 100 mJ energy level to few-cycle duration below 10 fs and the other corresponding to the compression of pulses, which already are at few-cycle duration. Specific parameters and a detailed description of the two cases can be found in [Arnold 2009]. The first scenario particularly emphasizes the suitability of the planar hollow waveguide concept to energy regimes unlikely to be accessible with filamentation or hollow capillaries. Additionally, the compressible energy could be further enhanced by using noble gases with higher ionization potentials (Ne and He). With a proper choice of the gas pressure to adjust the nonlinearity, the energy level compared to the 100 mJ case suggested in [Arnold 2009] could be increased by roughly a factor of ≈ 3 for Ne and ≈ 5 for He. The low nonlinearity, in particular for Ne, requires a specific design of the gas cell, able to withstand pressures much above the atmospheric pressure [Goulielmakis 2008]. The peak intensity (about $2 \times 10^{14} \text{ Wcm}^{-2}$ for He) should not be critical for the waveguide provided that the coupling conditions are good. It has been shown that peak intensities higher than 10^{15} Wcm^{-2} can be propagated inside hollow capillaries without wall damage [Dorchies 1999, Wagner 2004]. Furthermore, the waveguide separation can be increased to lower the intensity in the waveguide.

Following the experimental results, we now also address the transverse homogeneity and the focusability of the compressed output mode numerically. Figure 5.9 shows the spatio-temporal intensity profile of the compressed pulse (a), the transverse pulse duration (FWHM) (b), and the transverse spectrum (c) in the free waveguide dimension. For the sake of simplicity a clean Gaussian transverse beam profile was considered here. It is evident that pulse duration and spectral broadening strongly depend on the transverse position. The two dotted lines indicate the interval of pulse duration shorter than 1.5 times the on-axis duration. As performed in section 5.3 for the experimental case, we can again calculate the percentage of total pulse energy contained in this interval. The value of about 71 % is in well agreement with the value of 67.6 % obtained experimentally. Spectral splitting due to SPM is numerically more pronounced as compared to the experiments. It can however also be observed experimentally in figure 5.16(b). Note that pulse duration, spectral broadening, and spatial phase vary only along the free waveguide dimension; the guided dimension features homogeneous beam characteristics.

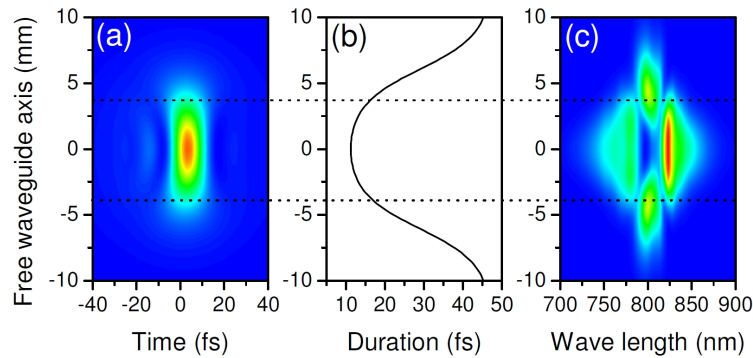


Figure 5.9: Temporal intensity (a), transverse pulse duration (FWHM) (b), and spectral intensity (c) versus the free waveguide dimension.

Having in mind that high power ultrashort pulse lasers typically have a more square-like or top-hat transverse beam profile, different from the Gaussian profile considered here, we also calculated the transverse homogeneity for super-Gaussian beam profiles. For a super-Gaussian pulse of order four, 85.6 % of the total pulse energy fall within the interval of 1.5 times the on-axis duration, for a super-Gaussian profile of order ten it is 93.5 %. Consequently, a compressed pulse at the 100 mJ energy level would feature significantly more homogeneous transverse spectrum and duration as compared to figure 5.9.

Finally, we also numerically investigate the focusability of the compressed pulse. As the guided waveguide dimension features homogeneous spectrum and duration, as well as flat spatial phase, it focuses intrinsically well ($M^2 < 1.1$). The discussion of focusability therefore concentrates on the free waveguide dimension. As discussed in section 5.3, there are three factors in the planar hollow waveguide compression scheme which potentially limit the focusability of the output pulse:

1. the transverse structure in the beam
2. the retarded phase along the output beam profile
3. the transversely inhomogeneous spectrum and duration

We will evaluate the impact of each factor and point out possible improvements. In order to study the focusability, we use frequency dependent diffraction theory as required for broadband pulses [Gu 2000]. First the electric field on the collimating cylindrical mirror (see figure 5.12) is calculated. As the beam expands rapidly after the end of the waveguide, we neglect nonlinear propagation in the gas medium and the output thin window of the gas cell. We numerically study the refocusing of the free waveguide axis with a focusing mirror. For the sake of simplicity we chose the same focal length ($f = 1$ m) as in the experiments. Figure 5.10(a-h) show on-axis spatio-temporal intensity profiles at different positions z along the optical axis in the vicinity of the focus (95–102 cm); the fluence along the optical axis is plotted in Figure 5.10(i). Several features can be extracted from Figure 5.10; first the pulse focuses at $z \approx 98$ cm, 2 cm before the actual focal length ($f = 100$ cm), indicating an astigmatism. Second the transverse size of the smallest focal spot (Figure 5.10(d)) is larger as compared to optimum focusing. Both effects, the focal shift and the reduction in focusability, were also experimentally recognized, as discussed in section 5.3. The shifts of the focal position towards the laser about 2 cm both experimentally (see figure 5.18) and numerically are in well agreement. This is an additional valuable verification of the appropriateness and accuracy of the numerical modeling.

Another interesting feature observable from figure 5.10 is that the long pulse durations located in the wings of the transverse profile, where almost no phase retardation occurs, focus close to the actual geometric focal position ($z = 100$ cm). The split intensity distribution at the focal position (figure 5.10F) is due to on-axis interference of the "long" wings with the "short" center of the beam. The focal shift can also be understood as a time gate, separating the short part from the long part of the beam. This can however also be achieved by cutting the "long" wings of the profile with an appropriate aperture.

While the astigmatism resulting in the focal shift can clearly be associated with the phase retardation along the transverse beam profile, the reduction in focusability is due to the transverse structure, the retarded phase, and the nonuniform duration and spectrum. To evaluate the impact of each effect, we compare focal intensities with the different effects numerically switched on and off. The impact of the transverse mode structure can easily be estimated by using an ideal Gaussian beam instead of the measured profile. The influence on the focusability is found to be small; the maximum focal intensity is reduced by less than 2%, if the measured input beam profile is used.

The influence of the retarded phase can be studied by artificially flattening the transverse spatial phase. Experimentally this can be performed with an appropriate adaptive mirror. If we compare the focal intensity for the pulse with the corrected spatial phase with the uncorrected one, an increase of the peak intensity of about

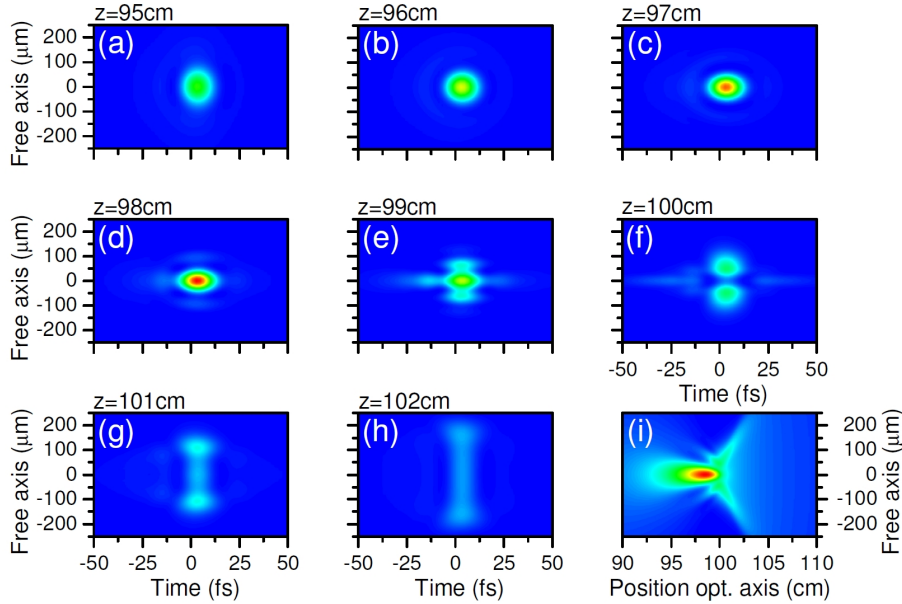


Figure 5.10: Focusing of the free waveguide dimension of the compressed output pulse with a ($f = 1\text{ m}$) focal length: (a-h) spatio-temporal intensity profiles at various positions on the optical axis in the vicinity of the geometrical focus, (i) fluence vs. position.

33% is observed. The spatio-temporal focal intensities with correction of the spatial phase are plotted in figure 5.11(a-h) at the same positions along the optical axis as in figure 5.10. Correction of the spatial phase reduces the focal spot size, increases the focal intensity, and removes the astigmatism simultaneously. Note that the fluence figure 5.11(i) is almost symmetric around the geometrical focus. The remaining discrepancy is due to higher order spatial phase, which cannot easily be corrected.

We evaluated that the focal intensity can be increased by about 33%, if the spatial phase is corrected by adaptive optics. However, the strongest impact on the focusability is due to the transverse temporal and spectral inhomogeneity. An ultrashort laser pulse with an inhomogeneous spatial duration as shown in figure 5.9 intrinsically focuses to a larger spot as compared to a pulse with homogeneous spectrum and duration. If we compare the focal intensity with a pulse of the same energy, which was artificially homogenized to the on-axis spectrum and duration, a 56% higher focal intensity is observed. This accounts to a Strehl ratio of about 64% for the case of corrected spatial phase by means of adaptive optics and about 48% for the uncorrected pulse. However the reduced focusability appears only for the free waveguide axis, whereas the guided axis focuses almost perfectly. Again we also investigated the focusability for more square-like, super-Gaussian transverse beam profiles. As discussed above, the transverse spectrum, duration, and phase are more homogeneous along the free waveguide axis for super-Gaussian beams. Thus the impact of these features on the focusability is less pronounced as compared to a

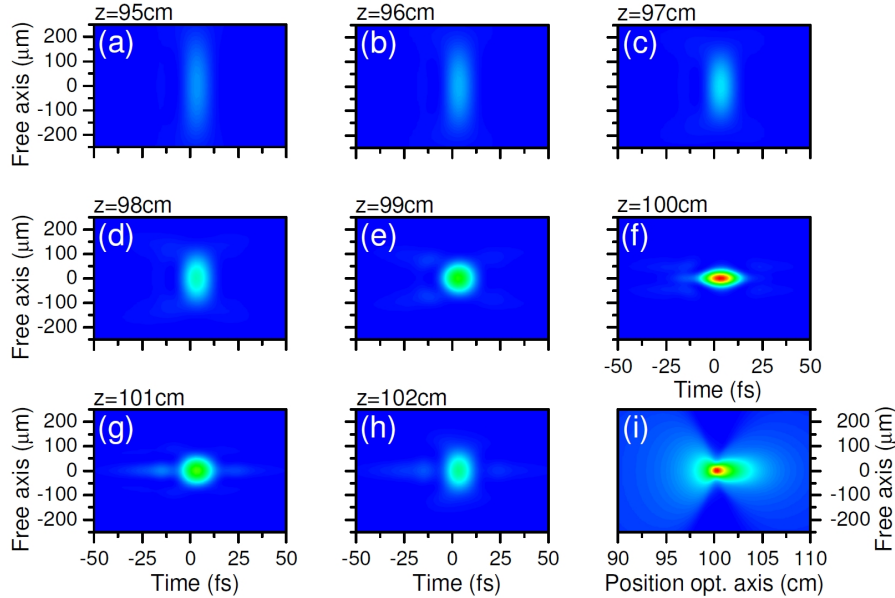


Figure 5.11: Same plot as figure 5.10, but for a pulse with corrected spatial phase.

Gaussian beam profile. For all super-Gaussian profiles (order 4 to 10) investigated, the focal intensity is reduced by less than 30% for an uncorrected pulse (without adaptive optics) as compared to a pulse with flattened phase and artificially homogenized spectrum and duration. Hence, adaptive optics is not obligatory.

5.3 Experimental results of laser pulse compression in a planar waveguide

5.3.1 Experimental setup

The experimental setup of the planar hollow waveguide pulse compression scheme is illustrated in figure 5.12. Today's CPA femtosecond lasers can emit pulse energies up to the Joule level, but pulse durations of typically longer than 20 fs. In our case the laser (Thales Alpha 100) delivers pulses of energy up to 15 mJ at less than 50 fs duration, 100 Hz repetition rate, and about 15 mm beam diameter ($1/e^2$). The planar hollow waveguide is placed inside a gas cell, which can be filled with various noble gases (Ar, Kr, and Xe) at adjustable pressure. The input and output windows of the cell are made of thin (1 mm) antireflection coated fused silica, to minimize dispersion and additional SPM. A cylindrical mirror is used to focus the laser beam to a line at the input of the planar hollow waveguide. The cylindrical axis of the focusing mirror needs to exactly coincide with the free transverse axis of the waveguide (where no guiding occurs).

To facilitate the alignment, all cylindrical optics are mounted on precision rotation and translation stages. To obtain the best coupling and throughput, the

longitudinal waveguide axis must be exactly parallel to the propagation direction of the incoming light and the line focus of the beam should be centered along the short transverse axis of the waveguide. In order to perform the required adjustments, the gas cell is held by xyz-stages at both ends. The polarization of the incoming light is chosen to be along the free waveguide axis, corresponding to TE (Transverse Electric) guided modes, which feature lower losses than TM (Transverse Magnetic) modes (see section 5.2.1). At the output of the cell the beam is re-collimated by using a second cylindrical mirror, placed one focal distance away from the end of the waveguide. Also the cylindrical axis of the collimating mirror must be exactly aligned with the focusing cylindrical mirror and the long waveguide axis in order to avoid aberrations. We use broadband dielectric cylindrical mirrors (Eksma, CVI) of focal length $f = 1.3\text{ m}$ both for coupling the beam to the waveguide and for collimation. After collimation, the beam bounces off a series of chirped mirrors (Femtolasers, Layertec) for spectral phase compensation.

Furthermore, different types of diagnostics are performed. The temporal pulse intensity and phase are measured using a frequency-resolved optical gating (FROG) device, capable of measuring pulses in the single-cycle regime [Akturk 2008c]. The spectrum and the pulse energy are monitored with a fiber spectrometer (Ocean Optics HR4000) and an energy-meter (GenTec), respectively. A Shack-Hartmann sensor (Imagine Optics HASO 32) is used to measure wave front distortions. Finally, a CCD camera (μEye) monitors the laser transverse spatial mode on a white screen placed close to the collimating cylindrical mirror.

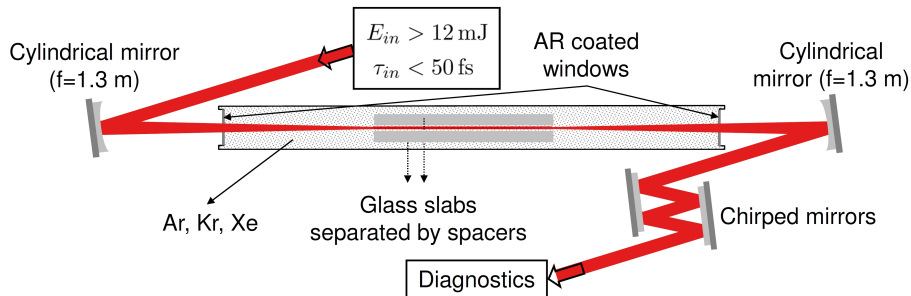


Figure 5.12: Sketch of the experimental setup for the planar hollow waveguide compression scheme.

5.3.2 Waveguide construction

The construction of the waveguide constitutes an important practical aspect of the method. In hollow dielectric waveguides the light is guided due to high reflection coefficients at grazing angle of incidence. As a result, the supported modes are intrinsically leaky (see section 5.2.1). However, if the waveguide separation is sufficiently large, the losses can be kept small, allowing high throughput. We assemble our planar hollow waveguides by using two slabs of glass of rectangular shape, separated by thin spacers cut as narrow stripes out of a polycarbonate foil (Precision

Brand) of homogeneous thickness. We place the spacers along the long edges of the slabs in order to provide as wide transverse aperture as possible. The inner glass surfaces need to be clean and completely free of dust, in order to prevent spatial mode deterioration. The assembly is favorably performed in a clean room environment.

Three different kinds of glass were used to fabricate waveguides. The experimental results published in [Akturk 2009] were obtained with a waveguide made from fused silica of dimensions $19 \times 6 \times 210$ mm with all six surfaces polished for each of the two slabs (WZW Optics); the thickness of the spacers used was $127 \mu\text{m}$. Waveguides of larger dimension still made from fused silica can be quite expensive. We therefore also tested cheaper float glass materials available in larger size, in particular Borofloat33 (Schott) and soda lime glass (PGO). For the waveguide made from Borofloat33 only the long surfaces constituting the waveguide were polished, the front and side surfaces were cut and the edges grinded. In case of the soda lime glass none of the surfaces was treated. The slabs were simply scribe-cut out of a plate of thin (3 mm) soda lime float glass. We first compared the attenuation for the three different kinds of waveguides (with same slab separation). No significant difference was observed. Since there was no gas cell available to house all three waveguides, the experiments were performed in air. The waveguide made from Borofloat33 has the dimensions $40 \times 10 \times 500$ mm, whereas the one made from soda lime glass is of dimensions $40 \times 3 \times 250$ mm. Next we compared the output spatial modes and spectral broadening for the three waveguides. Since the lengths of the individual waveguides were different, we adjusted the input pulse energy to have comparable spectral broadening. Figure 5.13 shows the broadened spectra and the associated output spatial modes for the waveguide constructions mentioned above. Spectral broadening is significant in all cases. The distinct red-shift of the broadened spectra can be associated with the delayed Kerr response of air [Nibbering 1997b]. For the waveguide made from soda lime glass more pulse energy is required in order to obtain comparable broadening. This can be roughly quantified by comparing the values of the B-integral (see section 5.2.3), which depends on the input pulse energy, the waveguide length and separation, as well as the gas pressure. For soda lime glass the B-integral value to obtain comparable spectral broadening is about 20% higher as compared to the two other options.

In terms of output spatial mode quality the waveguide made from all-way polished fused silica glass plates exhibits the best mode quality; slightly stronger structure is observed for the two other options (see figure 2). The sharp edges of the spatial output mode profile for the fused silica waveguide are due to beam clipping from the spacers, since the 19 mm width of the waveguide minus the width required for the spacers (about 1 mm on each side), was slightly too narrow for the beam.

For the waveguide made from soda lime glass, we observe dark staining of the glass material at the entrance of the waveguide, after coupling high power femtosecond pulses into the waveguide. This modification is known to be color center formation due to multiphoton absorption in this type of glass [Dickinson 2004]. For Borofloat33 and fused silica no alterations of the material were observed.

In summary, the best spatial mode quality is obtained with all-way polished fused

silica slabs. The float-glass alternatives are significantly lower-cost and easier to fabricate with large dimensions, while slightly compromising the spatial mode quality. The experiments were performed using all-way polished fused silica waveguides.

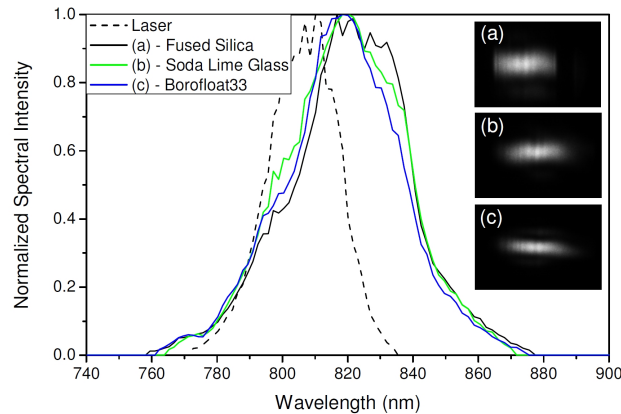


Figure 5.13: Comparison of spectral broadening and output mode quality for the three different waveguide materials; (a) Fused Silica, (b) Soda Lime Glass, (c) Borofloat33.

5.3.3 Dependence of pulse compression on gas type and pressure

The planar waveguide pulse compression scheme requires strong SPM in order to obtain sufficient spectral broadening. The strength of SPM in the waveguides can be adjusted by using different gases and pressures. On the other hand, as mentioned above, small-scale self-focusing along the free waveguide dimension causes spatial mode deterioration [Chen 2008]. Since SPM and small-scale self-focusing both result from the same physical effect (Kerr nonlinearity) in the gas medium, spectral broadening and transverse mode deterioration are closely connected. We compare the hollow planar waveguide compression scheme for the gas cell filled with Ar, Kr, and Xe at 1 atm pressure each. The nonlinear refractive index n_2 is the highest for Xe and the lowest for Ar [Shelton 1990]. Fig. 5.14 shows the measured temporal output pulse intensity and phase after compression as well as the spatial mode profiles for the three noble gases. As indicated in the figure caption, the duration becomes shorter as the nonlinear index of refraction increases. The shortest pulses were thus obtained in Xe. However, the spatial mode deterioration due to small-scale self-focusing is also the strongest in this case. The input pulse energy for Ar and Kr was ≈ 12.5 mJ (limited by the laser system), while for Xe the input pulse energy had to be reduced below 6.7 mJ to avoid beam breakup. The output pulse energies were 7.6 mJ and 8.5 mJ for Kr and Ar respectively and 3.7 mJ for Xe. As a result, Ar and Kr provide favorable conditions, while Xe exhibits excessive nonlinearity. Additionally, it should be noted that the ionization potential for Xe is lower (12.13 eV) as compared to Kr (13.99 eV) and Ar (15.76 eV). In order to have SPM dominated spectral broadening, plasma formation should be minimized by choosing

a gas with high ionization potential. Ar seems to be a preferable choice since the nonlinearity can be adjusted sufficiently high within the pressure range of our cell and the high ionization potential simultaneously minimizes nonlinear ionization.

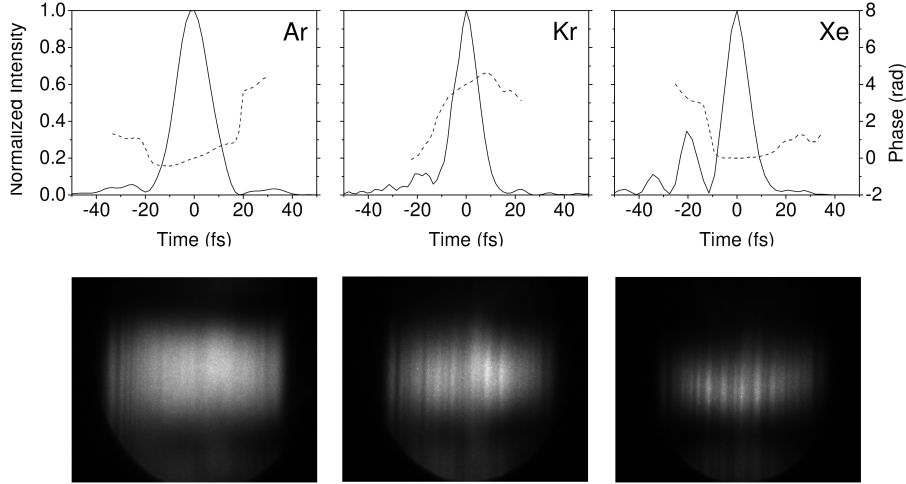


Figure 5.14: Measured temporal intensity and phase (upper row) and output mode (lower row) for Ar, Kr, and Xe (from left to right). Output Pulse durations: 16.1 fs, 11.5 fs, 11.4 fs. Output Energies: 8.5 mJ, 7.6 mJ, 3.7 mJ.

We also studied pulse compression as a function of gas pressure for an Ar filled waveguide. Increasing the pressure, increases the nonlinear refractive index and thus both the impact of SPM and small-scale self-focusing. As the deterioration of the spatial output mode compromises the possible compression, a trade-off between the target pulse duration and an acceptable mode quality needs to be found. Here pressures up to 1.6 atm of Ar were studied, which provide significant shortening at still acceptable output mode quality. Figure 5.15(a) shows the measured pulse durations after compression as a function of Ar pressure. As expected, the pulse duration becomes shorter with increasing pressure. The energy throughput does not significantly depend on the gas pressure. We observe pulse energies of ≈ 11 mJ at the output of the gas cell, corresponding to a throughput larger than 75 % within the whole pressure range. This confirms that the intensity inside the waveguide remains below the level of excessive ionization for Ar. Spectral broadening is thus dominated by SPM and the compressed pulse duration depends linearly on the Ar pressure. At a pressure of 1.6 atm a mean duration of 12.9 fs (FWHM) is measured. The temporal profile is very clean with a prepulse of less than 8 % of the peak intensity of the main pulse. Figure 5.15(b) shows a typical measured temporal intensity profile.

5.3.4 Variation of pulse duration along the beam transverse dimension

Since SPM and consequently spectral broadening is determined by the light intensity in the waveguide, the compressed pulse duration may vary along the non-guided

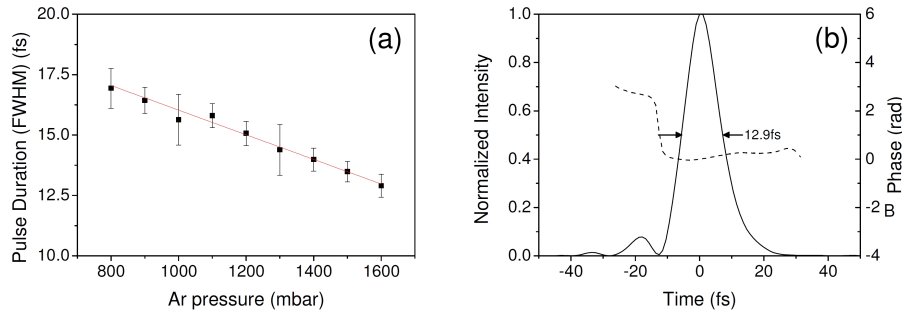


Figure 5.15: Measured pulse duration after compression versus Ar pressure (left). A typical measured temporal pulse profile after compression at 1.6 atm (right).

dimension, at least if the transverse beam profile is different from a top-hat. The laser beam profile in our experiments was nearly Gaussian, we hence expect a significant variation of spectral broadening and compressed pulse duration along the free waveguide axis. In order to characterize this effect, a 1 mm wide slit was used, which we moved through the non-guided dimension of the beam in 0.5 mm steps. The broadened output spectrum and the compressed pulse duration were measured as a function of position along the free waveguide dimension. The chirped mirror compression was optimized to obtain the shortest pulse duration in the beam center and kept constant for all other positions. The pressure in the cell containing the waveguide was adjusted to 1.6 atm of Ar and the input pulse energy was slightly above 14 mJ. At the output of the cell 10.8 mJ were measured and the shortest duration in the beam center was around 10.6 fs (FWHM). Figure 5.16 shows the output spatial mode (a), the spectrum (b), and the measured pulse duration (c) along the free waveguide dimension. The output spatial mode features significant structure in this experiment, indicating that the Ar pressure is close to the maximum permissible value at this input pulse energy. The spectral broadening clearly follows the transverse beam profile with the broadest spectra generated in the beam center, where the intensity is the highest. The shortest duration is measured close to the beam center as well.

Figure 5.16(d) shows a typical temporal pulse profile measured at the beam center. Due to slightly different experimental conditions and in particular a different combination of chirped mirrors for compression, the pulses are shorter here as compared to figure 5.15, but also exhibit a more pronounced prepulse. Due to limitations in terms of power level and pulse duration for the FROG setup, reliable measurements of the pulse duration were only possible within a 6 mm wide range around the beam center. Although the compressed pulse duration becomes longer towards the edges of the transverse beam profile, the well compressible beam center contains a significant portion of the total beam energy. Within our measurement interval the pulse duration varies from 10.6 fs to about 13 fs (figure 5.16(c)). This interval of relatively homogeneous pulse duration contains about 67.6% of the total output pulse energy. In terms of possible scalability of the hollow planar waveguide compres-

sion scheme to higher pulse energy, it should be mentioned that higher energy laser systems typically yield beam profiles closer to top-hat, in order to avoid diffraction effects in the medium [Siegman 1986]. Considering such a beam profile, the pulse duration would be even more uniform along the beam. The transverse homogeneity in terms of spectrum and duration as well as the influence of more square-like super-Gaussian beam profiles was discussed in detail in the numerical part.

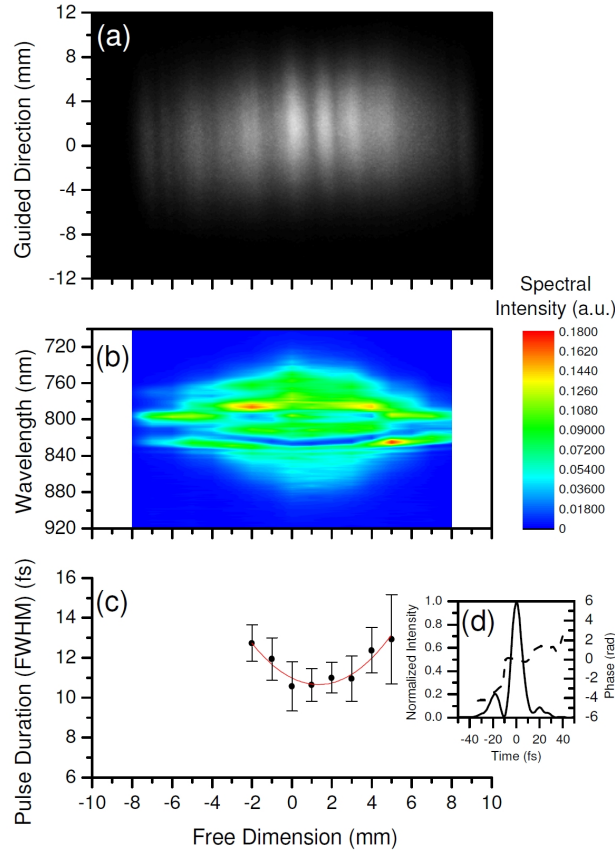


Figure 5.16: Transverse output profile (a), Spectrum (b), and measured pulse duration (c) along the non-guided direction. Typical measured temporal pulse profile in the beam center (d).

5.3.5 Spatial phase and focusability

As discussed above, the critical constraint in the planar hollow waveguide compression scheme is the beam characteristics in the free waveguide dimension. To prove that the scheme is indeed useful for applications in high-field physics, we will show that the compressed pulses are focusable to nearly diffraction limited spot size. Here we discuss the experimentally accessible focusability; a detailed numerical analysis follows in section 5.2.3. While the guided dimension should focus intrinsically well, the focusability of the free waveguide dimension is compromised. If the light inten-

sity in the free dimension is not uniform, the strength of SPM will vary along the beam, resulting in inhomogeneous spectral broadening and duration after compression. Similarly, because of the intensity dependent refractive index, high intensity portions of the transverse profile are retarded, resulting in a spatial phase front and pulse front delay. The transverse phase retardation directly follows the reversed intensity profile in the free waveguide dimension. For a simple Gaussian beam a parabolic phase delay will be most prominent. This should have two distinct effects. First, the parabolic phase induces an astigmatism, which if the beam is focused, results in a shift of the focal position towards the laser for the free dimension, whereas the guided dimension focuses further down. Second, the beam focuses to a larger (not diffraction limited) spot for the free dimension. In order to study the impact of the spatial phase on the focusability, the spatial phase profile was measured with a Shack-Hartmann wave front sensor. Since this experiment was performed in air, the input pulse energy was varied instead of the gas pressure, in order to increase or decrease the level of nonlinearity in the waveguide.

Figure 5.17 compares the measured spatial phase profiles (spatial tilt subtracted) for various pulse energies. It is evident that with increasing pulse energy the beam develops a strong astigmatism. The high intensity beam center lags behind and the wave front bends along the free dimension, whereas the wave front in the guided dimension remains flat.

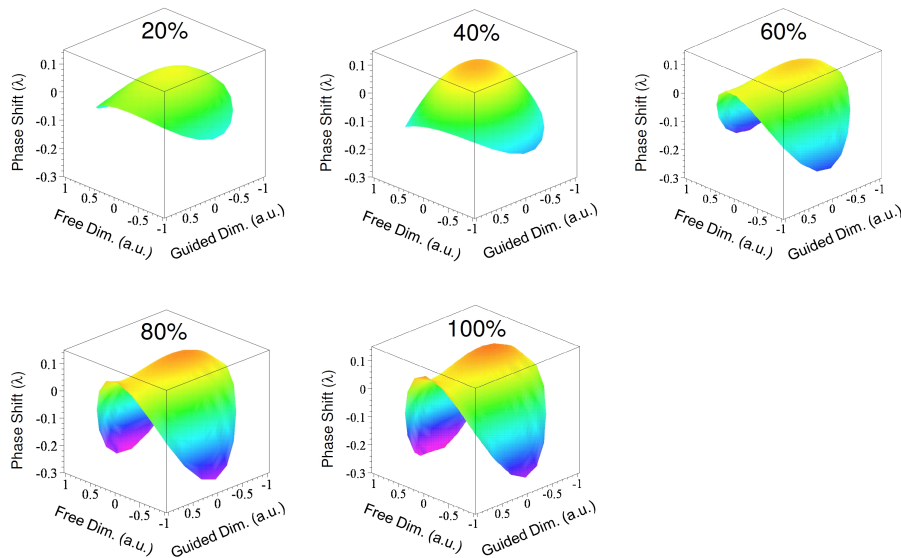


Figure 5.17: Measured spatial phase profiles (spatial tilt subtracted) at different pulse energy levels.

In a second measurement the focusability of the output beam was directly investigated. After carefully attenuating the beam by using the reflections from two consecutive fused silica wedges, the beam was focused with a 1 m focal length lens directly on a CCD camera chip, which could be moved through the focus along

the optical axis. Spatio-temporal aberrations due to the thin lens are negligible. Figure 5.18 compares the focal spot size as function of position along the optical axis for the guided and the free waveguide dimensions at various Ar pressures. As expected from the above discussion, the focal spot size of the guided dimension does not significantly change, as the gas pressure and thus the nonlinearity in the waveguide is increased. However, for the non-guided dimension we observe a significant shift of the focal position towards the laser as well as a larger focal spot size, as the gas pressure is increased. The focal spot radius $2\sigma(z)$ (plotted in figure 5.18) was

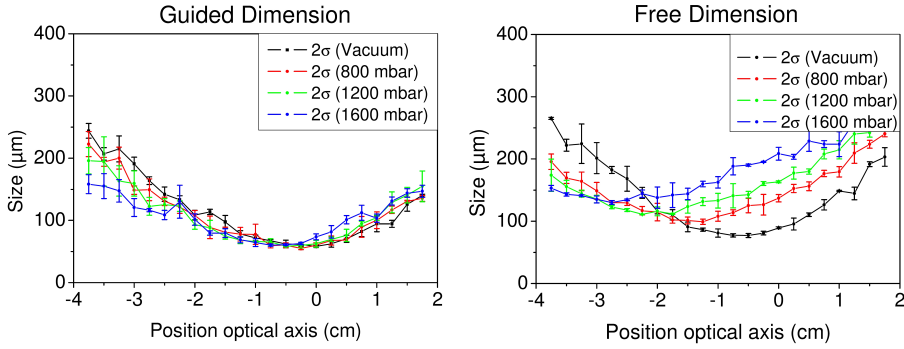


Figure 5.18: Focal spot radius (second order moments) versus position on the optical axis for different Ar pressures. Guided waveguide dimension (left). Free Dimension (right).

measured by calculating the second order moments for the guided and the free dimension directly from the CCD images. Moment theory provides a reliable measure of the beam size even for non-Gaussian transverse profiles. For a Gaussian beam the quantity 2σ is equivalent to the Gaussian beam radius w ($1/e^2$). For the focal spot sizes presented in figure 5.18 the quantities 2σ and w were about the same value, indicating that the focal profile was single-peaked and close to Gaussian. It must be noted that this method measures the focal spot size of the fluence (intensity integrated over time), whereas the temporal intensity focal beam profile could in principle be different. By performing a parabolic fit for $\sigma^2(z)$, we can estimate the focusability in terms of M^2 -values. For the guided dimension values between 1.3 and 1.5 are found for all pressures, what is reasonable. However, the non-guided dimension exhibits a higher value of $M^2 = 2.33$ already at vacuum. For higher Ar pressures a reliable M^2 -fit was not possible. However, we verified that the quite high M^2 -value for the free dimension was mostly due to the laser ($M^2 = 2.1$ without waveguide) and not induced by the waveguide. As the pressure is increased from vacuum to 1.6 atm of Ar, the focal spot size in the free dimension increases by a factor of 1.85. Simultaneously the focus position shifts about 2 cm towards the laser.

To sum up the above discussion, the nonlinear effects inside the waveguide, essential for pulse compression, simultaneously induce a finite astigmatism and reduce the focusability in the free waveguide dimension. However, both limitations can in principle be addressed by means of adaptive optics. Note however that the focus-

ability constraints due to spectral and temporal inhomogeneity can not be corrected by adaptive optics (see section 5.2.3). The astigmatism itself can be corrected, even without adaptive optics, simply by moving the collimating cylindrical mirror (see figure 5.12) towards the waveguide until the focal positions of both dimensions coincide. Thus the focal spot size at a pressure of 1600 mbar is less than a factor of two larger as compared to vacuum. Furthermore, as mentioned above, higher energy systems deliver transverse beam profiles closer to top-hat, significantly reducing the problems of spatial phase and transverse inhomogeneity.

5.3.6 Optimization of input pulse duration

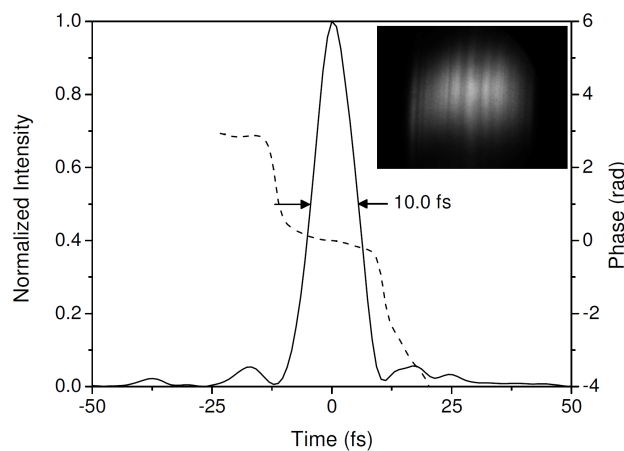


Figure 5.19: Temporal profile after compression at 1.5 atm of Ar and 37 fs input duration. The inset shows the output mode profile.

In order to optimize the input pulses for the compression, a programmable spectral amplitude and phase filter (DAZZLER, Fastlite) was installed in the laser chain before the regenerative amplifier. With this device the spectral phase of the laser output pulses could be significantly flattened and the duration of the driving pulses for the planar hollow waveguide compression was reduced to 37 fs (FWHM). Additionally, a slightly shorter focal length ($f = 110$ cm, CVI) cylindrical mirror was used to focus the beam onto the waveguide entrance, improving the coupling to the fundamental waveguide mode. While the input laser pulse energy slightly decreased due to the implementation of the spectral filter, the waveguide throughput increased to about 80% and 10.6 mJ pulse energy were obtained at the output of the cell. Simultaneously, due to the shorter input pulse duration and the precise control of the input chirp, the pulse duration after compression was reduced to 10.13 ± 0.33 fs at 1.5 atm of Ar in the gas cell. Figure 5.19 shows a typical measured temporal intensity profile and phase as well as the output mode. The temporal profile is very clean with two prepulses of less than 5% of the peak power. Note that the shorter pulse duration after compression obtained here is mostly due to the optimization of the input pulse. The total level of nonlinearity, which determines the output mode

quality and the focusability, remains unchanged.

5.4 Generation of a filament plasma in helium gas with few-cycle pulses

In helium, the ionization potential $I_p \sim 24.587$ eV, and the nonlinear refraction index $n_2 = 3.6 \times 10^{21}$ cm²/W, therefore the critical power $P_{cr} \sim 0.263$ TW, which is around two order of magnitude larger than the one in air. With our laser system, P_{cr} is only reached after external compression of the pulse through the planar waveguide. The simulation of the filament in helium gas has been performed by B. Forestier and A. Couaïron (see Figure 5.20). Although the electron density in Helium is comparable to the one in air, the laser intensity reaches 5×10^{14} W/cm², with which electrons can gain more forward momentum. The electron would be accelerated over longer distance in helium filamentation.

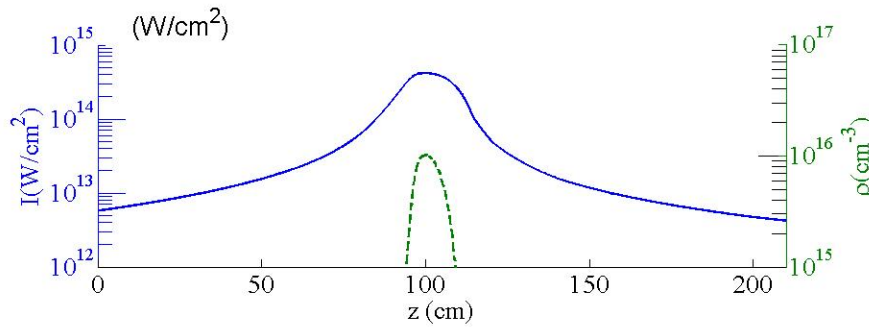


Figure 5.20: The simulated laser intensity and electron density of a filament in Helium at 1bar.

With nearly 1 TW compressed laser pulse, we have used this compressed laser pulse to perform filamentation experiments in Helium gas. These are preliminary results, and the experiments are still in progress. Figure 5.21 shows the experimental set-up. The 11 mJ, uncompressed laser pulse after the Argon filled planar waveguide is sent to the Helium chamber. Inside the chamber, first the laser pulse is compressed through the chirp mirror pairs down to 10 fs. Next the 10 mJ, 10 fs, linearly polarized laser pulse is focused by a spherical mirror into a glass tube to generate a filament.

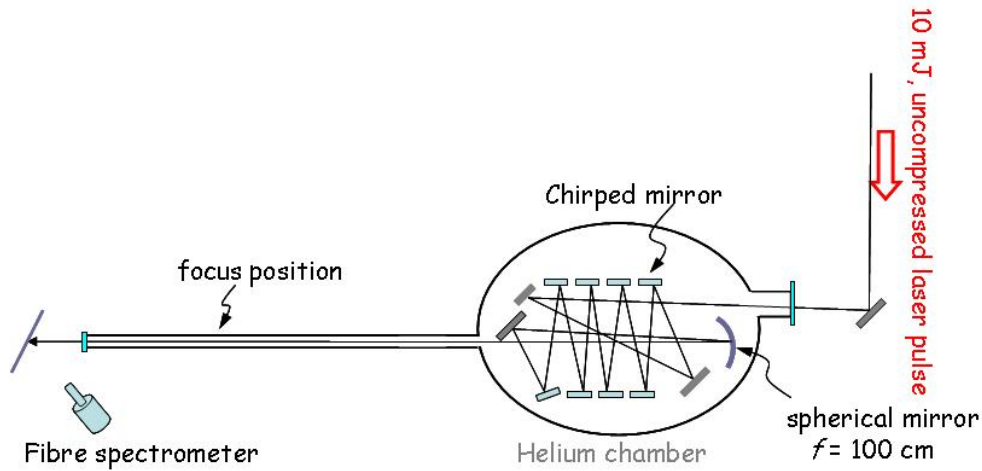


Figure 5.21: Experimental set-up for the generation of a filament in Helium. The 11 mJ, uncompressed laser pulse after the Argon filled planar waveguide is sent to the Helium chamber. The focal length of the spherical mirror is 1 m. The pressure of Helium gas is 1 bar.

Figure 5.22 shows a comparison of the filament photos obtained with 10 fs and 40 fs. In the upper photo, the laser power $P \sim 4P_{cr}$. In the lower photo $P \sim 0.15P_{cr}$. One can see two major differences:

1. The length of the plasma is longer with 10 fs laser pulse. With 6 mJ, 40 fs laser pulse, the plasma length is $\sim L_{DF} = 3.9$ cm; with 10 mJ, 10 fs laser pulse, the plasam is $\sim 3L_{DF}$.
2. There is a spatial shift if the ionized region.

The spectra in vacuum and with 1 bar Helium gas were taken at the exit window of the tube (see Figure 5.23). The spectra broadening and blue-shifted imply that there are nonlinear processes and plasma column, when the 10 fs laser pulse passes through 1 bar Helium gas. These give solid evidences for the filamentation in Helium. In order to obtain additional confirmation, I used the technique described in Chapter 4 to measure currents at the beginning, the middle, and the end of the ionized channel (shown in Figure 5.24). Similar to the filament in Argon with linearly polarized laser pulse, the initial current direction remains unchanged. This also brings an evidence for the existence of a filament plasma channel.

5.5 Conclusion

We presented, by using the planar hollow waveguide, a comprehensive overview which covered both experimental results from hollow wave guide fabrication to optimization of output and simulations for the compression of ultrashort laser pulses to the few-cycle regime. The key benefit of the planar hollow waveguide, as compared

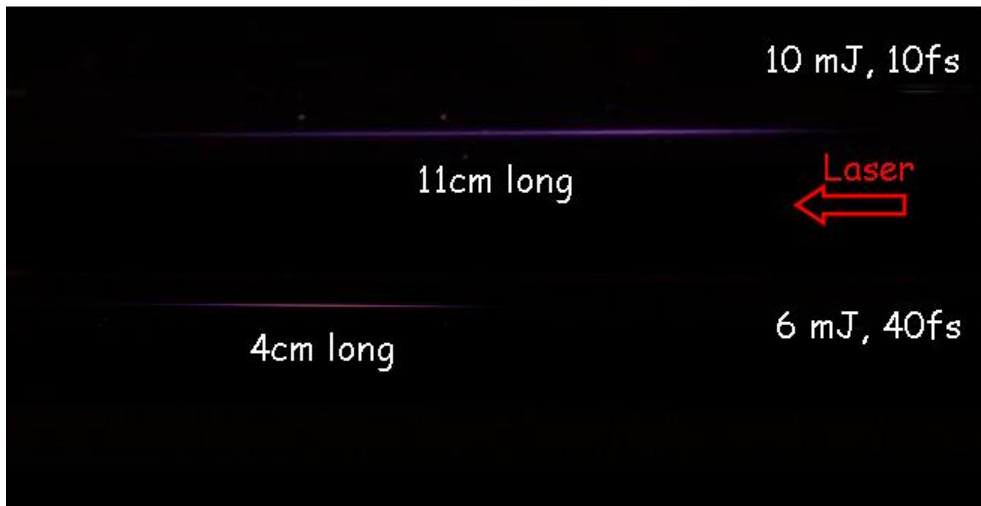


Figure 5.22: Photos obtained. Upper: with 10 mJ and 10 fs, linearly polarized laser pulse. Bottom: with 6mJ and 40 fs, circularly polarized laser pulse.

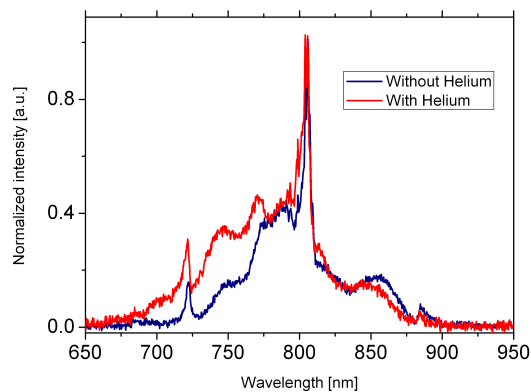


Figure 5.23: Normalized spectra, The blue: Without Helium gas. The red: with 1 bar Helium gas. The laser pulse is 10 mJ, 10 fs.

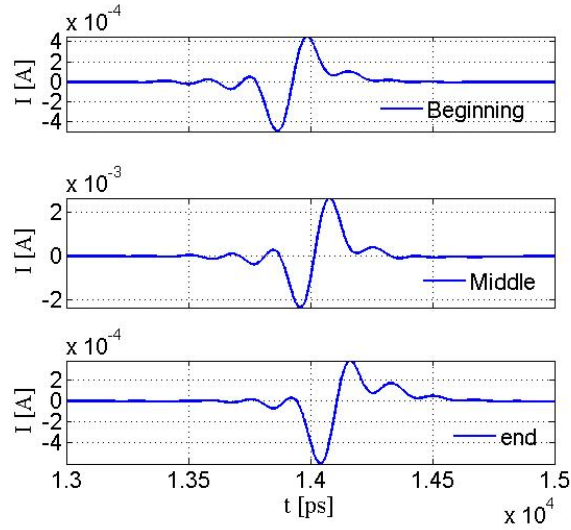


Figure 5.24: Oscillating currents at the beginning, the middle, and the end of the ionized channel. Helium gas pressure is 1 bar.

with the hollow capillaries and filamentation, is the superior scalability to high laser pulse energy, when the laser pulse was compressed down to few cycle regime. The energy level of 100 mJ for the compression of ultrashort pulses to the few-cycle regime could in principle be further increased by the choice of noble gases with higher ionization potential (Ne and He) as well as by increasing the waveguide separation. Furthermore, the transverse nonlinear dynamics in the free waveguide dimension influence the output mode quality, the pulse duration, and the focusability of the output pulse. These aspects were in detail addressed both experimentally and numerically, and furthermore the possible improvements were highlighted. Based on the theoretical model and simulation, the region of stable waveguide propagation and its impact on energy scalability were investigated, which are in excellent agreement with experimental results.

Experimentally, We achieved 10.6 mJ output pulse energy at 80% energy throughput and shortest pulse duration of 10.1 fs (FWHM) after compression. The output pulses were characterized in detail in terms of transverse homogeneity, spatial phase, and focusability. A simulation reveals that the compressed pulses at few-cycle duration can be focusable into Helium gas to yield intensity 10^{14} Wcm^{-2} , which is one order of magnitude larger than the one in air. At such intensity, the light matter interactions take place in the strong field regime, and I have experimentally confirmed that there exists filamentation in Helium gas. This has opened the way to important applications of intense few cycle laser pulses in the field of high order harmonic generation in noble gases. Since the ground state depletion is shifted to higher intensities, the cutoff of the harmonic generation is shifted to higher harmonics; few cycle laser pulses can drive the emission of coherent radiation down to the soft X ray region of the electromagnetic spectrum. In short, more systematic

experiments will reveal new features of the filamentation with the few cycle laser pulses.

Conclusion

Laser sources nowadays deliver ultrashort light pulses reaching high peak powers. When such pulses propagate through gases, there is a dynamic competition between the Kerr focusing process and plasma defocusing, leading to a filament formed. During three years of my thesis, I have studied some new aspects of filamentation and its applications.

In chapter 1, I have briefly introduced the filamentation, its history, and its properties.

In Chapter 2, I have discussed the generation of Bessel beam with an axicon (a conical lens). First, I have presented the properties of an axicon in the linear regime. Different from a conventional lens, the laser beam after an axicon can generate a long focal line. Secondly, I have compared the properties of an axicon lens and a conventional lens in the nonlinear regime. Compared with a conventional lens, by using an axicon, a more uniform and longer filament plasma channel can be generated but with much less electron density (for instance in 1 bar air $\rho \sim 10^{14}/\text{cm}^3$).

In Chapter 3, I have demonstrated that a short-lived fs laser induced filament plasma channel can be revived milliseconds after it has disappeared by a delayed ns laser pulse. Normally, free electrons will attach to neutral molecules with low affinity energy. These electrons can be easily detached and multiplied through impact ionization by the ns laser pulse. As a result by using an axicon to focus a ns laser pulse the filament plasma can be revived over a distance exceeding 50 cm long. We have first observed revivals of a filament plasma at a delay as large as several milliseconds. Furthermore with a sufficient intensity ns laser pulse, the avalanche process could be pushed up to a dielectric breakdown. These results are important for the development of applications, such as triggering lightning, in which the short lifetime of the plasma has posed a limitation.

In chapter 4, I have directly measured longitudinal oscillating currents inside plasma channels in the wake of a short, intense IR femtosecond laser pulse. First, I have presented a specially designed high speed Rogowski coil and its characteristics; secondly, I have shown the laser polarization dependence and gas pressure dependence of measured currents in gases; lastly, based on experimental results I have proposed a physical model: the oscillating current depends on the balance of the two forces in a plasma channel. The first force, laser force, always pushes free electrons forward; the second force, a Coulomb wake force pulls free electrons backward, and its magnitude depends on the nature of the gas, and gas pressures.

Finally, with the current probe I have measured the oscillating currents in very dilute air ($\sim 0.4\mu\text{bar}$), the currents are very different from those in a filament plasma. In this case, at the focus more electrons are generated by the double ionization and laterally drift out of the plasma, consequently oscillating currents are governed by a positive pole at the focus.

In chapter 5, in order to form a filament in 1bar Helium gas, first I have presented a scheme for the laser pulse compression with a planar wave guide. With such a scheme, a $35fs$ laser pulse with $14mJ$ energy has been compressed down to a $10fs$ laser pulse with $10mJ$ output. Furthermore, I have shown preliminary results of the filamentation in 1Bar Helium. Lastly, the presence of a filament plasma channel in 1bar *He* has been verified by the current detection. According to the simulation, the intensity in *He* reaches $10^{14}\text{W}/\text{cm}^{-2}$.

In short, after the three years's study, I have found that filamentation, a light-matter interaction, involved many subjects such as nonlinear optics, plasma physics, radiology, chemistry, quantum mechanics. However, I continue to improve the understanding in some aspects. For instance, in chapter 3 with double pulse technique, the plasma can be revived after several milliseconds, is there any limitation for the revival time. The plasma lifetime has been increased to microsecond, is it possible to increase the life time further; in Chapter 4 concerning the oscillating currents with bi-color laser pulses (800 nm and 400 nm), the energy of 400 nm laser pulse is only $\sim 3\%$ of the energy of 800 nm laser pulse, but the bi-color laser pulse can generate the current with an amplitude five times larger than the one generated by 800 nm laser pulse alone, and we have no explanation yet for this effect; in chapter 5, since the laser intensity can reach $10^{14}\text{W}/\text{cm}^{-2}$, with such intensity, can we accelerate free electrons in a filament plasma over several centimeters? These questions inspire me to continue filamentation experiments in the future.

Appendix

7.1 Ponderomotive energy and electron kinetic energy in a strong laser field

When an electron is exposed in the orthogonal electric and magnetic laser field, without considering the collision, the electron gain further kinetic energy. Generally the energy absorbed by the electron upon ionization can be divided into 3 parts: **(1)** Ionization energy I_p **(2)** Drift energy **(3)** Oscillation energy

Here we introduce Ponderomotive Energy U_p , which refers to the cycle averaged quiver energy of a free electron in an E field as given by,

$$U_p = \frac{e^2 E^2}{4m\omega_0^2} \quad (7.1)$$

Where e is the electron charge, E is the linearly polarized electric field amplitude, ω_0^2 is the laser carrier frequency and m is the electron mass. In terms of the laser intensity I , using $I = c\epsilon_0 E^2/2$, it reads less simply $U_p = e^2 I / 2c\epsilon_0 m\omega_0^2 = 2e^2 / c\epsilon_0 m \times I / 4\omega_0^2$. If the laser light is linearly polarized, The electron drift energy depends on the phase of the field at the instant of ionization, while for the circularly polarized laser field, all the electrons have the same drift energy, which is equal to U_p .

When the circularly polarized laser acts on an electron. It oscillates with average energy U_p , the energy absorbed by an electron is $(1) + (2) + (3) = I_p + 2U_p$. The forward momentum is $P_{//} = +(I_p + 2U_p)/c$. If the laser field slowly is turned off. The oscillatory energy **(3)** disappears, since it is returned to the laser field as a small blue-shift in the photon energy. The electron is left with net energy absorbed $I_p + U_p$. Finally, the electron has forward momentum $P_{//} = +(I_p + U_p)/c$. This is the simple case, and I will present more detail in the following section.

7.2 The motion of an electron with linearly polarized laser field

This section has been calculated by A. Couairon and P. Mora.

7.2.1 Electric field and the vector potential

Assuming that the laser pulse propagates along z direction, the electric field polarized in the x direction, this yields

$$\begin{aligned}
\mathbf{E} &= E_{0x} \left[\cos\left(\frac{\pi\xi}{Tc}\right) \cos\left(\frac{\omega_0\xi}{c} + \theta\right) \right] \mathbf{u}_x \\
&= \frac{E_{0x}}{2} \left[\cos\left(\frac{\pi\xi}{Tc} + \frac{\omega_0\xi}{c} + \theta\right) + \cos\left(\frac{\pi\xi}{Tc} - \frac{\omega_0\xi}{c} - \theta\right) \right] \mathbf{u}_x, \quad (7.2)
\end{aligned}$$

where, T is laser pulse duration, and \mathbf{u}_x is the vector unit along x axis. $\mathbf{B} = B_y \mathbf{u}_x$ with $B_y = E_x/c$. This is an exact result due to the specific envelope (cosine shape) and the assumption that $v_g = v_\phi = c$. The vector potential is:

$$\mathbf{A} = \frac{E_{0x}}{\omega_0} \frac{1}{1 - \pi^2/\omega_0^2 T^2} \left[\cos\left(\frac{\pi\xi}{Tc}\right) \sin\left(\frac{\omega_0\xi}{c} + \theta\right) + \frac{\pi}{T\omega_0} \sin\left(\frac{\pi\xi}{Tc}\right) \cos\left(\frac{\omega_0\xi}{c} + \theta\right) \right] \mathbf{u}_x \quad (7.3)$$

The second term may be neglected for multicycle pulses with $T\omega_0 \gg 1$.

$$A = \frac{E_{0x}}{\omega_0} \cos\left(\frac{\pi\xi}{Tc}\right) \sin\left(\frac{\omega_0\xi}{c} + \theta\right) \quad (7.4)$$

By rewriting the potential vector Eq.7.4 in terms of amplitude and phase:

$$A_x = \mathbb{A}_x \sin(\phi) \quad (7.5)$$

$$\phi = \frac{\omega_0\xi}{c} + \theta \quad (7.6)$$

$$\mathbb{A}_x = \frac{E_{0x}}{\omega_0} \cos\left(\frac{\pi\xi}{Tc}\right) \quad (7.7)$$

7.2.2 Longitudinal Electron momentum

According to the equations above, the longitudinal electron momentum reads as:

$$p_{//} = \frac{I_p}{c} + \frac{(N\hbar\omega_0)^2}{2mc^3} + \frac{1}{2mc} [p_{x,0} - e(\mathbb{A}_{x,0} \sin(\phi_0) - \mathbb{A}_x \sin(\phi))]^2 \quad (7.8)$$

Finally, for $\mathbb{A}_x \equiv 0$:

$$p_{//,\infty} = \frac{I_p}{c} + \frac{(N\hbar\omega_0)^2}{2mc^3} + \frac{1}{2mc} [e\mathbb{A}_{x,0} \sin(\phi_0) - p_{x,0}]^2 \quad (7.9)$$

In Eq. 7.9, $p_{x,0} \sim \sqrt{2m(N\hbar\omega_0 - I_p) - (N\hbar\omega_0)^2/c^2}$. The second term on the right hand side of the equation can be neglected compare to the first term.

7.2.3 The ponderomotive force

The time-averaged electron momentum (over an optical cycle) is governed by an evolution equation expressed in terms of the ponderomotive force $\mathbf{F}_p \equiv -\nabla U_p$. This force derives from the ponderomotive potential $U_p \equiv e^2 \mathbb{A}_\perp^2 / 4m$, where \mathbb{A}_\perp denotes the transverse component of the envelope of the vector potential.

$$\frac{\partial p_{//}}{\partial \xi} = \frac{e^2}{4mc} \frac{\mathbb{A}_{\perp}^2}{\partial \xi} \quad (7.10)$$

Note: there is no minus sign in Eq.7.10, because it cancels out in the change of variable $\xi = z - ct$, $d/dt \sim -c\partial/\partial\xi$. By integration (assuming $p_{//,0} \neq 0$, to be determined):

$$\begin{aligned} p_{//} &= p_{//,0} + \frac{e^2}{4mc} (\mathbb{A}_{\perp}^2 + \mathbb{A}_{\perp,0}^2) \\ &= p_{//,0} + (U_p - U_{p,0})/c \end{aligned} \quad (7.11)$$

The final value for the longitudinal momentum obtained from Eq.7.11 is

$$\begin{aligned} p_{//} &= p_{//,0} - \frac{e^2}{4mc} \mathbb{A}_{\perp,0}^2 \\ &= p_{//,0} - U_{p,0}/c \end{aligned} \quad (7.12)$$

Eq. 7.12 shows that the effect of the ponderomotive force is to decrease the initial averaged electron momentum $p_{//,0}$ by a quantity that corresponds to the initial ponderomotive potential. In this respect, it can be interpreted as a radiation pressure.

7.2.4 Determination of $p_{//,0}$

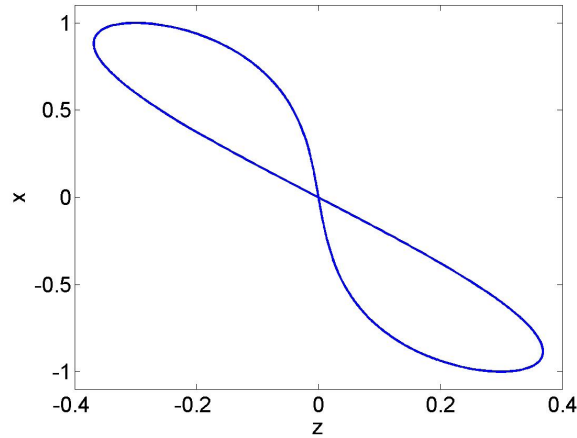


Figure 7.1: Motion of an electron injected at a given time in the pulse, in the reference frame that is at rest on the average (linear polarization). Only one cycle is shown and the effect of the envelope is neglected (i.e plane wave). $z \equiv p_{//} - \bar{p}_{//}$; $x \equiv p_{\perp} - \bar{p}_{\perp}$; from Eq.7.14

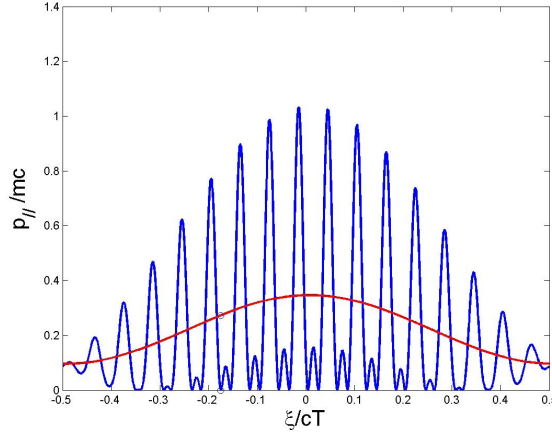


Figure 7.2: Parallel momentum (blue curve) and averaged parallel momentum (red curve) of an electron injected at a given time (marked by the small circle) in a linearly polarized laser pulse

The time averaged electron momentum is obtained for $\langle \sin^2(\phi) \rangle = 1/2$ and $\langle \sin(\phi) \rangle = 0$ in Eq.7.8. This yields:

$$\begin{aligned} \overline{p_{//}} &= p_{//,\infty} + \frac{e^2}{4mc} \mathbb{A}_x^2 \\ &= p_{//,\infty} + U_p/c \end{aligned} \quad (7.13)$$

The motion in the reference frame that is at rest on the average (see Figure.7.1) is obtained by:

$$p_{//} - \overline{p_{//}} = -\frac{e^2}{4mc} \mathbb{A}_x^2 \cos(2\phi) + \frac{e}{mc} (p_{x,0} - e\mathbb{A}_{x,0}^2 \sin(\phi_0)) \mathbb{A}_x \sin(\phi) \quad (7.14)$$

$$p_{\perp} - \overline{p_{\perp}} = \mathbb{A}_x \sin(\phi) \quad (7.15)$$

The description in terms of the ponderomotive force (Eq.7.11) is equivalent to that with the oscillating term in Eq.4.18 provided the initial averaged momentum satisfy the conditions:

$$\overline{p_{//,0}} = p_{//,0} + \frac{U_{p,0}}{c} \quad (7.16)$$

$$\overline{p_{x,0}} = p_{x,0} - e\mathbb{A}_{x,0} \sin(\phi_0) \quad (7.17)$$

The first equation in the above system ensures that $\overline{p_{//,\infty}} = p_{//,\infty}$. Since this quantity is always positive, the final electron momentum is always in the forward direction.

7.3 The motion of an electron with circularly polarized laser field

For the circularly polarized laser, the electric field is

$$E_x = E_0 \left[\cos\left(\frac{\pi\xi}{Tc}\right) \cos\left(\frac{\omega_0\xi}{c} + \theta\right) \right] \quad (7.18)$$

$$= \frac{E_0}{2} \left[\cos\left(\frac{\pi\xi}{Tc} + \frac{\omega_0\xi}{c} + \theta\right) + \cos\left(\frac{\pi\xi}{Tc} - \frac{\omega_0\xi}{c} - \theta\right) \right] \quad (7.19)$$

$$E_y = E_0 \left[\cos\left(\frac{\pi\xi}{Tc}\right) \sin\left(\frac{\omega_0\xi}{c} + \theta\right) \right] \quad (7.20)$$

$$= \frac{E_0}{2} \left[\sin\left(\frac{\pi\xi}{Tc} + \frac{\omega_0\xi}{c} + \theta\right) - \sin\left(\frac{\pi\xi}{Tc} - \frac{\omega_0\xi}{c} - \theta\right) \right] \quad (7.21)$$

$$\mathbf{B} = B_x \mathbf{u}_x + B_y \mathbf{u}_y \quad \text{with} \quad B_y = E_x/c \quad \text{and} \quad B_x = -E_y/c$$

This is still an exact result, again due to the specific envelope (cosine shape) and the fact that $v_g = v_\phi = c$. Similar to the linearly polarized laser pulse, for the circular polarization, the vector potential in terms of amplitude and phase (for multicycle pulses with $T\omega_0 \gg 1$) :

$$A_x = \frac{E_0}{\omega_0} \cos\left(\frac{\pi\xi}{Tc}\right) \sin\left(\frac{\omega_0\xi}{c} + \theta\right) \quad (7.22)$$

$$A_y = -\frac{E_0}{\omega_0} \cos\left(\frac{\pi\xi}{Tc}\right) \cos\left(\frac{\omega_0\xi}{c} + \theta\right) \quad (7.23)$$

By rewriting the potential vector in terms of amplitude and phase:

$$A_x = \mathbb{A}_\perp \sin \phi \quad (7.24)$$

$$A_y = -\mathbb{A}_\perp \cos \phi \quad (7.25)$$

$$\phi = \frac{\omega_0\xi}{c} + \theta \quad (7.26)$$

$$\mathbb{A}_\perp = \frac{E_0}{\omega_0} \cos\left(\frac{\pi\xi}{Tc}\right) \quad (7.27)$$

The final parallel momentum reads as:

$$p_{//}(\infty) = \frac{e}{mc} \left(\frac{e}{2} \mathbb{A}_{\perp,0}^2 + \mathbf{p}_{\perp,0} \cdot \mathbf{u}_{\phi_0} \mathbb{A}_{\perp,0} \right) \quad (7.28)$$

where $\mathbf{u}_\phi \equiv -\sin \phi \mathbf{u}_x + \cos \phi \mathbf{u}_y$. Average:

$$\bar{p}_{//} = \frac{e^2}{2mc} \mathbb{A}_\perp^2 + \frac{e}{mc} \mathbb{A}_{\perp,0} \left(\frac{e}{2} \mathbb{A}_{\perp,0} + \mathbf{p}_{\perp,0} \cdot \mathbf{u}_{\phi_0} \right) \quad (7.29)$$

Motion in the reference frame that is at rest on the average:

$$p_{//} - \bar{p}_{//} = \frac{e}{mc} \left(-\mathbf{p}_{\perp,0} \cdot \mathbf{u}_\phi - e \mathbb{A}_{\perp,0} \cos(\phi - \phi_0) \right) \mathbb{A}_\perp \quad (7.30)$$

$$\mathbf{p}_\perp - \bar{\mathbf{p}}_\perp = -e \mathbb{A}_\perp \mathbf{u}_\phi \quad (7.31)$$

The average momentum is governed by an evolution equation expressed in terms of the ponderomotive force:

$$\frac{\partial \bar{p}_{//}}{\partial \xi} = \frac{e^2}{2mc} \frac{\partial \mathbb{A}_{\perp}^2}{\partial \xi} \quad (7.32)$$

By integration (assuming $\bar{p}_{//,0} \neq 0$, to be determined):

$$\bar{p}_{//} = \bar{p}_{//,0} + \frac{e^2}{2mc} (\mathbb{A}_{\perp}^2 - \mathbb{A}_{\perp,0}^2) \quad (7.33)$$

The final value for the longitudinal momentum must be equal in both descriptions:

$$\bar{p}_{//}(\infty) = \bar{p}_{//,0} - \frac{e^2}{2mc} \mathbb{A}_{\perp,0}^2 = \frac{e^2}{2mc} \mathbb{A}_{\perp,0}^2 \quad (7.34)$$

The circular polarization can then be described by the ponderomotive force provided the injection time is mimicked by a longitudinal and transverse initial average momentum:

$$\bar{p}_{//,0} = I_p/c + \frac{e^2}{mc} \mathbb{A}_{x,0}^2 \quad (7.35)$$

$$\bar{p}_{\perp,0} = p_{\perp,0} - e\mathbb{A}_{\perp,0} \quad (7.36)$$

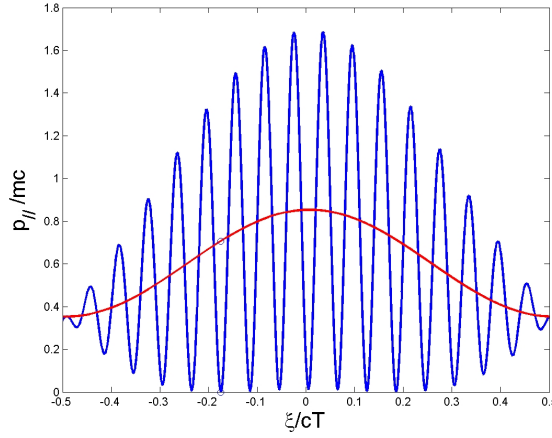


Figure 7.3: Parallel momentum of an electron injected at a given time in a circularly polarized laser pulse

7.4 Several optical devices and optical elements

7.4.1 Dispersive Chirped Mirrors

A chirped mirror is a kind of dielectric mirror which is usually used for dispersion compensation in mode-locked lasers. Another interesting feature of chirped mirrors

is that they make it possible to achieve a broader reflection bandwidth than ordinary Bragg mirrors.

The basic idea of chirped mirror designs is that the Bragg wavelength is not constant but varies within the structure, so that light at different wavelengths penetrates to a different extent into the mirror structure and thus experiences a different group delay.

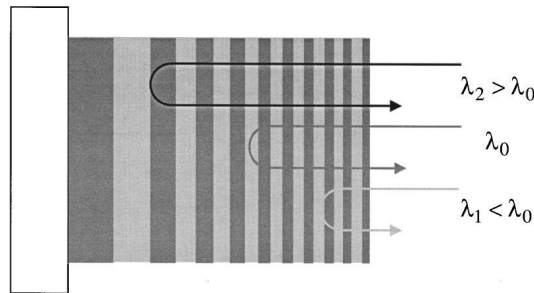


Figure 7.4: Operation principle of a chirped mirror.

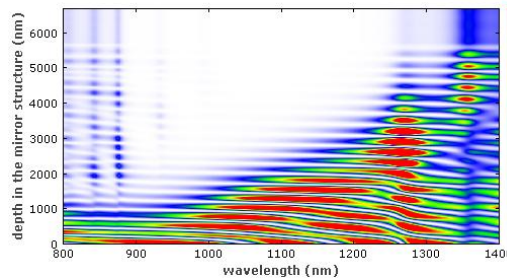


Figure 7.5: Field penetration into the chirped mirror (800 – 1400 nm). It is apparent that within the wavelength range 1000 – 1200 nm, the field penetrates more deeply into the structure for longer wavelengths. The larger group delay for longer wavelengths corresponds to anomalous dispersion. This picture is from Physics encyclopedia web.

Figure 7.4 shows the general principle of chirped mirrors, light with a long wavelength penetrates deeper into the mirror structure and thus experiences a larger group delay. This leads to anomalous chromatic dispersion. However, a naive design directly based on this idea would not work: first, there is a Fresnel reflection at the front face (the interface to air), which leads to strong additional dispersion as in a Gires Tournois interferometer. Secondly, the sudden "switching" of the coupling of counter propagating waves from zero in air to a finite value in the structure causes a kind of impedance mismatch.

However, both problems can be eliminated with a double-chirped design, which has two additional features: the Fresnel reflection is removed with an additional anti-

reflection structure on top of the double-chirped section. The coupling of counter-propagating waves is turned on smoothly by also varying the duty cycle (i.e. the ratio of optical thickness of high and low index layers). For instance, a chirp mirror is well designed for 800 – 1400 nm in Figure 7.5

Double-chirped mirrors (DCMs) are often used for dispersion compensation in mode-locked lasers, particularly for those with pulse durations below 20 fs. They are typically designed not only to compensate a constant group delay dispersion, but also to correct higher-order dispersion. However, there are limits concerning how much dispersion (and in particular higher-order dispersion) can be compensated with a double-chirped mirror. Possible solutions are to use a suitable combination of several mirrors. Another challenge arises from the tight fabrication tolerances; at least some of the layers typically have to be fabricated with a precision of the thickness of a few nanometers. The remaining wiggles in the group delay versus wavelength can be further reduced by using appropriate combinations of mirrors where the wiggles at least partially cancel each other

7.4.2 Dazzler: Acousto-Optic Modulators for Dispersion Compensation

Dazzler is an acousto-optic programmable dispersive filter (AOPDF), providing for large dispersion-compensation ranges, which does not have to be positioned in the Fourier plane of a dispersion line. The Dazzler crystal is driven by a radio-frequency (rf) voltage signal, which is converted into a traveling wave by a piezoelectric transducer. The acoustic wave traveling in the modulator induces a refractive index grating through a photoelastic effect. Such a grating can be phase, amplitude, or frequency modulated by using a suitably modulated rf signal. The optical spectrum of the input light pulse is modified according to the grating spatial modulation function.

The device is based on a collinear acousto-optic interaction in a birefringent uniaxial crystal. The acoustic frequency is a variable function of time and provides control over the group delay of the diffracted optical pulse. At the same time, the spectral amplitude of the diffracted pulse is driven by the intensity of the acoustic signal.

As demonstrated in [36], the optical output $E_{out}(t)$ of the Dazzler is proportional to the convolution of the optical input, $E_{in}(t)$, and the scaled acoustic signal: $E_{out}(t) \propto E_{in}(t) \otimes S(t/\alpha)$, where the scaling factor $\alpha = \Delta n(V/c)$ is the ratio of the speed of sound to the speed of light times the index difference between the ordinary and the extraordinary waves. Therefore, by generating the proper function $S(t)$, it is possible to generate any arbitrary convolution with a temporal resolution given by the inverse of the filter bandwidth. Such a device has been used in a kilohertz chirped-pulse amplification laser chain: compensating for gain narrowing and residual phase errors with the Dazzler.

Proper characterization of the pulse intensity and phase is a crucial part of near single cycle pulse generation. Regardless of the compression method, it is always

necessary to have feedback to be able to perform the required corrections of the phase distortions and to verify the final pulse duration. As for the generation, the measurement of the near single cycle pulses poses certain difficulties. As a result, it is necessary to make improvements and modifications in the existing pulse measurement techniques to adapt to this extreme regime. We will briefly discuss some of these methods below. Note that we will not be concentrating on the measurement of the carrier envelope offset of the pulse electric field, which requires a different approach and for which there are well established techniques.

7.4.3 SPIDER

Proper characterization of the pulse intensity and phase is a crucial part of near single cycle pulse generation. Regardless of the compression method, it is always necessary to have feedback to be able to perform the required corrections of the phase distortions and to verify the final pulse duration. As for the generation, the measurement of the near single cycle pulses poses certain difficulties. As a result, it is necessary to make improvements and modifications in the existing pulse measurement techniques to adapt to this extreme regime. We will briefly discuss some of these methods below. Note that we will not be concentrating on the measurement of the carrier envelope offset of the pulse electric field, which requires a different approach and for which there are well established techniques.

One of the commonly used methods for ultrashort pulse characterization is spectral interferometry for direct electric field reconstruction (**SPIDER**) [Iaconis 1998]. The conventional setup requires modifications to eliminate the additional dispersion of the unknown pulse, before the nonlinearity, to accommodate the pulse bandwidth, and also to improve the sensitivity in the weaker spectral components [Kornelis 2003]. A more important issue with **SPIDER** measurements, arising particularly in the single cycle regime, is the requirement of precise calibration and stability of the temporal delay between the two pulses [Gallmann 1999]. Normally, **SPIDER** needs the stringent alignment and careful calibration, which now can be relaxed by two dimensional shearing interferometry, requiring multishot measurements and significantly increases the experimental complexity.

Generally, the implementation of **SPIDER** always relies on the elements summarized on the following figure.

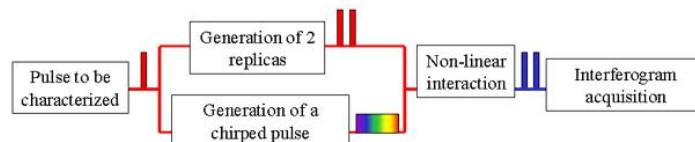


Figure 7.6: Main elements in a SPIDER setup. The picture is from Physics Department, Oxford University 2003

First, the unknown laser pulse is split into two pulses, which generate a chirped

pulse and two replicas of the initial pulse respectively. Then secondly, by using a non collinear setup with a type II crystal, the two branches interacted nonlinearly, finally by measuring the interferogram, the electric field of the initial laser pulse and its phase can be reconstructed.

Spectral interferometry provides a simple and robust way to characterize ultrashort optical pulses. There are a number of important features that make **SPIDER** suitable for such applications. First, the rapidity of the data acquisition and inversion mean that the reconstruction is not compromised by the source stability. Moreover, the inversion algorithm returns the mean spectral phase when the signal is averaged over small random fluctuations in the pulse shape. Second, accurate measurement of the spectral phase does not require the recorded trace to be "corrected" for the phase matching function of the nonlinear process or the detector sensitivity. The key to this remarkable robustness is that the phase information is contained in the fringe spacing rather than the visibility, and this is not compromised by wavelength-dependent response in the apparatus, provided the sensitivity does not vary across one fringe. Moreover, systematic errors in SPIDER measurements can be easily identified by measuring a pulse before and after propagation through a material with known dispersion. Third, the redundancy of data in a single SPIDER interferogram allows determining the precision of the measurement and also provides a built-in consistency check. Fourth, the inevitable presence of space time coupling when using pulses of such extreme bandwidth means in many cases that measurements of the spatio temporal field are warranted.

There are no fundamental limitations to the measurement of even shorter pulses using **SPIDER**. The major technical limitation lies in the nonlinear frequency conversion, which for all techniques, demands shorter crystals as the pulse bandwidth increases. This gives rise to noise in the form of non phase matched contributions to the signal. Nonetheless, in SPIDER, background signals from the fundamental of the test pulse and the upconverted pulse can be removed using filters, geometric multiplexing, or numerical filtering during inversion, and the apparatus measurement bandwidth is limited only by the transparency of the nonlinear materials used.

7.4.4 FROG

Another well-established method for ultrashort pulse intensity and phase measurements is frequency-resolved optical gating (**FROG**) [Kane 1993]. Since its invention, **FROG** has been demonstrated successfully for various pulse lengths and wavelengths [Akturk 2004]. Baltuska et al. have shown that **FROG** also works well in the few-cycle regime, provided that various spectral and temporal weighting factors are taken into account. The spectral factors result from the conversion efficiency of the second-harmonic-generation (SHG) crystal and responses of the optical elements. These effects constitute an overall spectral filter, and by carefully calculating this filter, and dividing the experimental **FROG** trace by it, the standard **FROG** algorithm yields the correct pulse electric field. In the multishot configuration, the fact that the beams must cross at a finite angle causes a time domain weighting

called geometrical time smearing [Baltuska 1998]. It causes the pulse to appear longer than it actually is, and the shorter the pulse, the more significant this effect becomes. Like the spectral effects, this effect can also be calculated and extracted from the trace. By performing all these corrections, Baltuska et al. demonstrated **FROG** measurements of 4.6 fs pulses, generated by spectral broadening in fiber, and compression with a combination of a prism pulse compressor and chirped mirrors [Akturk 2008c].

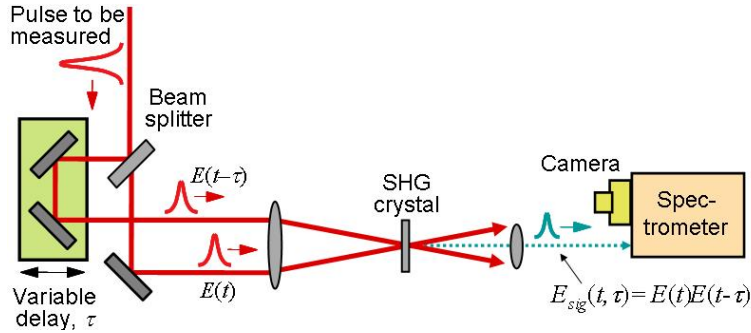


Figure 7.7: Second-harmonic-generation FROG.

Among the **FROG** family, Second-harmonic-generation FROG (**SHGFROG**) is the most sensitive device, and is most appropriate for low energy pulses, because the signal is second order, rather than third order ($I_{Frog}(\omega, \tau) = |\int_{-\infty}^{\infty} E_{sig}(t, \tau) \exp(-i\omega t) dt|^2$, $E_{sig}(t, \tau) = E(t)E(t - \tau)$). The signal pulses for different color and polarization allow effective suppression of scattering input light, adding to the suppression provided by the geometry. These lend credibility for the (**SHGFROG**) to measure down to single cycle unknown laser pulse.

In our experiment set up, we use a home made single-shot **FROG** configuration designed and built by the former colleague S. Akturk, which is capable of measuring pulses down to single cycle durations. Spectral correction schemes similar to the ones mentioned above, but different approaches are adapted to increase the device response in the short wavelength, where spectral intensity is relatively low. A special spectrometer, UV-enhanced, and broadband components are used to address the extreme bandwidth issues. Most importantly, since the setup is single shot, the temporal delay is generated by crossing two beams at an angle in a line focus; hence, it is essentially free of the geometrical time-smearing effects. The configuration is practically straightforward to build and relatively easy to align.

The layout of the **FROG** is shown in the Fig. 7.8 below. The system is built on a $2. \times 2.$ breadboard. Note that not all of the components on the breadboard are parts of the actual **FROG**. The components of FROG start from the *input iris*. The direction of the input beam should be from the *iris* towards the *bi-mirrors*. The system is built such that when the input beam is aligned (using the procedure described below) on the *input iris* and the *crosshair* on the *bi-mirror*, the trace should appear properly on the camera. Adjustment of the components may require re-calibration. For proper measurements the input beam diameter should be

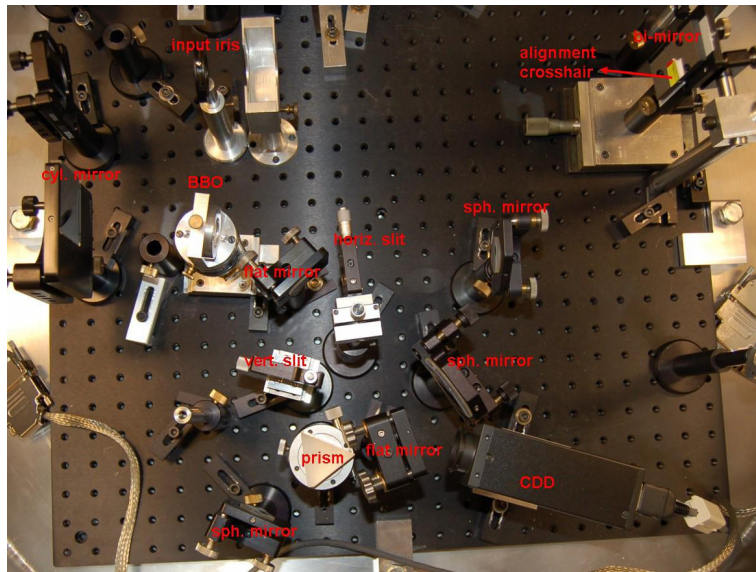


Figure 7.8: The FROG setup. Picture is the FROG Set-up in ILM Group, LOA, Polytechnique 2009

10 mm. In the configuration, after bouncing off the chirped mirrors, the beam goes through a small pinhole and is expanded by a $10x$ telescope. This configuration also allows measurement of the pulse duration as a function of the position on the beam. These steps, however, can be bypassed, realigned, modified or replaced by others if needed. As mentioned above, the real **FROG** components start with the iris. In our experiments, we measure all the pulses with the made **SHG-FROG**, which brings us reliable results and tolerant errors.

7.5 Several processes in a plasma

7.5.1 Ionization

When a intensive a strong laser field acts on an atom or an molecule, the bonding electrons outside the nuclei gains the kinetic energy, if the kinetic energy is sufficient for the electrons to break the Bond, the electrons will be liberated, the physical process is defined as single ionization.

In general, there are three qualitatively different single ionization mechanisms of atoms in strong external fields: *1* Multiphoton Ionization; *2* Tunneling; *3* Over Barrier Ionization (See Figure.7.9). All three mechanisms are just different aspects of the same universal process: nonlinear ionization. While apparently the multiphoton ionization (MPI) is appropriately treated in perturbation theory, the tunneling requires a classical treatment of the field. To distinguish between both regimes Keldysh examined the time t_f , which the electron would need to freely pass a distance comparable to the potential barrier.

$$t_f = \frac{\sqrt{2m_e U_i}}{eE} = 2\pi\omega_t^{-1} \quad (7.37)$$

where U_i is the ionization potential and E the laser electric field strength. To sets t_f in relation to the frequency of the external electric field, Keldysh defined $\gamma = \omega/\omega_t$ as Keldysh parameter.

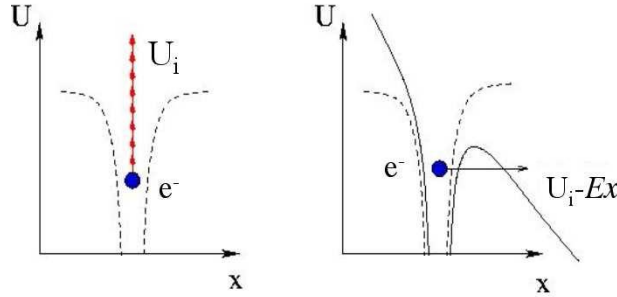


Figure 7.9: Schematic diagram: **Left** multiphoton ionization. **Right** tunnel ionization.

For $\gamma \ll 1$: the oscillation period $2\pi/\omega$ of the external electric field is large compared to the tunneling time, then tunneling can occur. For $\gamma \gg 1$: the oscillation period is small compared to the tunneling time then this mechanism does not apply and ionization would have to be treated perturbatively in the multiphoton.

7.5.1.1 Multiphoton ionization

At intensities ($\sim 10^{13}\text{W/cm}^2$) lowest order perturbation theory can model the experimental ionization rates via absorption of n photons very closely [86]. The ionization rate obeys the power law:

$$W_{MPI} = \sigma_K I^K \quad (7.38)$$

where, σ_K denotes the coefficient of the multiphoton ionization (MPI) rate involving K photons, ($K \equiv \langle U_i/\hbar\omega_0 + 1 \rangle$), U_i denotes the ionization potential of the medium and ρ_{at} , the density of neutral atoms.

7.5.1.2 Above Threshold Ionization

Agostini et al. [Agostini 1979] in 1979 reported the first observations of a discrete photoelectron spectrum produced by MPI where the spacing between the electron energies was just the photon energy. It seems that Above Threshold Ionization (ATI)

contradicts the physicists intuition: an ionized electron absorbs more photons than required energy to jump over the potential well. However, as long as the electron is still in the vicinity of the parent ion some coupling to the parent ion by their coulomb fields still exists, allowing for the absorption of more photons from the laser field and hence giving rise to discrete peaks in the photoelectron energy spectrum.

Application of perturbation theory to ATI yields the simple extension of the power law $W_{ATI} \propto \sigma_{K+S} I^{K+S}$ to the absorption of additional S photons above the ionization threshold.

7.5.2 Electron collision inside the plasma

When an electron is liberated with certain kinetic energy, it is unavoidable to collide with other particles, including ions, atoms, molecules. There are many kinds of collisions for an electron, therefore it is complicated to sort out all the collisions. However, there are three kinds of electron collisions, which are very important for Chapters following.

(1) Ionization



Where e denote an electron, and M denote an atom or a molecule. This process is the base element of the electrons avalanche process in which a number of free electrons in a medium collide with atoms to generate new electrons (called impact ionization), and the forming "new" electrons undergo the same process in successive cycles. Electron avalanches are essential to the dielectric breakdown process within gases. The process extends to huge sparks streamers in lightning discharges propagate by formation of electron avalanches created in the high potential gradient ahead of the streamers' advancing tips. Once begun, avalanches are often intensified by the creation of photoelectrons as a result of ultraviolet radiation emitted by the excited medium's atoms or molecules.

(2) Vibrational transition



where v is the vibrational quantum number of the initial (final) state of the molecule. This process only exist in molecule gases. During the process, electrons lose energy to excite the molecules up to higher vibrational level, as a results electron become less dynamic, this can change the electron oscillation inside the plasma channel. Moreover the electrons, processing the same level kinetic energies, can exhibit distinguishable behaviors in atom gases and in molecule gases. For instance, Figure 7.10 shows the total scattering cross section of an electron with a N2 molecule in the resonance region [Itikawaa 2006]. Due to the resonance of the Nitrogen molecule, the cross section is much larger than the one shown in Figure 7.11 [Subramanian 1987], when the incident energy of an electron is in the range from 2 to 4 eV.

(3) Recombination

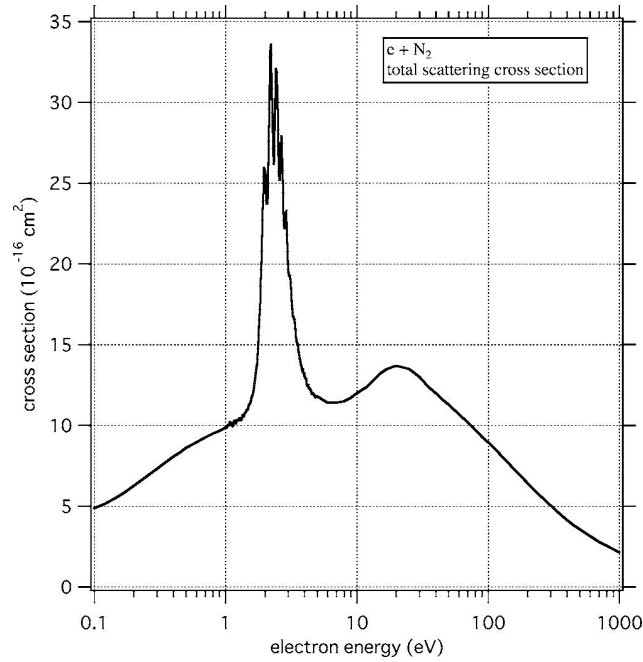


Figure 7.10: The total scattering cross section of an electron with a N2 molecule in the resonance region as a function of incident electron energy from 1 to 5 eV.



where λ is the photon wavelength emitted through the process. This process also behaves differently in atom gases and in molecule gases. Normally, in molecule gases the recombination is faster than in atom gases. Meanwhile, through the process, there always emits photon. By measuring the photon, one can deduce that there are free electrons before.

(4) Electron attachment



This process normally prefers polyatomic molecule. Differently from recombination, although the free electrons were trapped by molecules, comparing with photon energy, the affinity bonding energy is very low, as a result, the attached electrons can be easily detached by Photon. By taking advantage of this process, the short lived laser induced plasma channel can prolonged, we will give more detail in Chapter 3.

There are many papers reporting cross-sections for electron collisions. It is not easy to select one for presentation. As far as possible, the cross-sections are selected from those recommended or suggested in the reviews or data compilations published recently. It should be noted, however, that because of constant development of experimental techniques and theoretical methods, the quality of the cross-sections

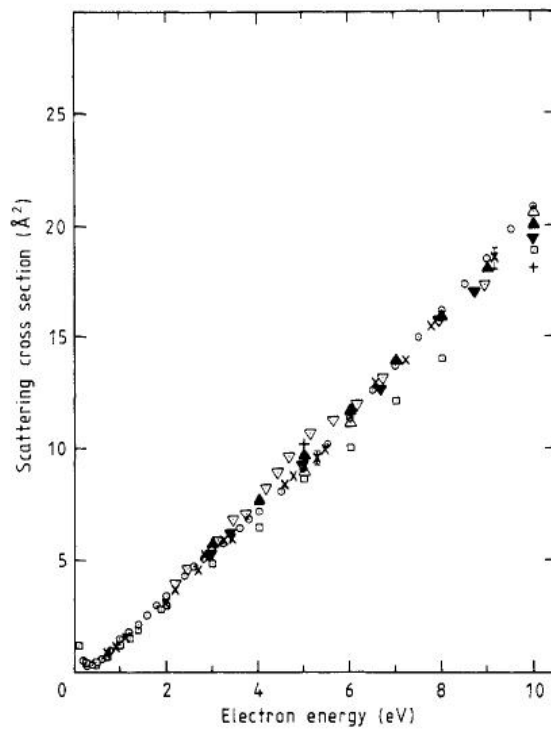


Figure 7.11: The total scattering cross section of an electron with Argon atom as a function of incident electron energy from 0.7 to 10 eV.

is continuously improved. When one wants to have the best value of some cross-section, a resurvey of the original, particularly more recent, literature should be strongly recommended.

8.1 Personal publication

1. B. Zhou, A. Houard, Y. Liu, B. Prade, A. Mysyrowicz A. Couairon, P. Mora C. Smeenk, L. Arissian, P. Corkum, *Electric current oscillations in dilute air plasmas* (to be submitted)
2. B. Zhou, B. Prade, A. Houard, J. Larour, A. Mysyrowicz, *A specially designed air core high speed Rogowski coil* submitted to Journal of Applied Physics
3. B. Zhou, A. Houard, Y. Liu, B. Prade, A. Mysyrowicz A. Couairon, P. Mora C. Smeenk, L. Arissian, P. Corkum, *Measurement and control of longitudinal electric currents inside femtosecond filaments* **106**, p 255002, Phys. Rev. Let. 2011
4. C. Smeenk, L. Arissian, B. Zhou, A. Mysyrowicz, D. M. Villeneuve, A. Staudte1, P. B. Corkum, *Partitioning of the linear photon momentum in multiphoton ionization* **106**, p. 193002, Phys. Rev. Let. 2011
5. S. Chen, A. Jarnac, A. Houard, Y. Liu, C. Arnold, B. Zhou, B. Forestier, B. Prade, and A. Mysyrowicz, *High-transmission flared waveguide tapers: Application to high-energetic ultrashort laser pulse compression* **28**, p. 1009, The Journal of Opt. Soc. Ame. A 2011
6. C. L. Arnold, B. Zhou, S. Akturk, S. Chen, A. Couairon and A. Mysyrowicz, *Pulse compression with planar hollow waveguides: a pathway towards relativistic intensity with table-top lasers*, New Journal of Physics, **12**, p. 073015 (juil 2010)
7. B. Zhou, S. Akturk, B. Prade, Y.-B. André, A. Houard, Y. Liu, M. Franco, C. D'Amico, E. Salmon, Z.-Q. Hao, N. Lascoux and A. Mysyrowicz, *Revival of femtosecond laser plasma filaments in air by a nanosecond laser*, Opt. Exp. 17, Issue 17, pp. 11450-11456 (juin 2009)
8. S. Akturk, C. Arnold, B. Zhou, and A. Mysyrowicz, *High energy ultrashort laser pulse compression in hollow planar waveguides* Opt. Lett. 34, Issue 9, pp. 1462-1464 (avril 2009)
9. S. Akturk, B. Zhou, M. Franco, A. Couairon and A. Mysyrowicz, *Generation of long plasma channels in air by focusing ultrashort laser pulses with an axicon* Opt. Commun. 282, Issue 1, pp. 129-134 (janvier 2009)

10. S. Akturk, B. Zhou, A. Houard, M. Franco, A. Couairon and A. Mysyrowicz, *Long plasma channels formed by axicon-focused filaments* Proc. SPIE, Vol. 7027, 70271E (2008)
11. S. Akturk, B. Zhou, B. Pasquiou, M. Franco and A. Mysyrowicz, *Intensity distribution around the focal regions of real axicons* Opt. Commun. 281, pp 4240-4244 (2008)
12. B. Zhou Y. Ling X. Chen Y. Leng R. Li Z. Xu, *Numerical simulation on propagation of ultra-short laser pulse in different GVD regions of photonic crystal fibers* ACTA OPTICA SINICA (in Chinese) VOL.27.No.3. 2007
13. B. Zhou, G. Liang, H. Wang, *Narrow frequency and sharp angular defect mode of one dimensional photonic crystals in visible and near-infrared*, LASER JOURNAL (in Chinese) Vol. 26. No.1. 2005

8.2 International conference

1. B. Zhou, A. Houard, Y. Liu, B. Prade, A. Mysyrowicz, A. Couairon, P. Mora, C. Smeenk, L. Arissian and P. Corkum, "Measurement and control of electric currents in Ar and N₂ filaments", oral talk CLEO/QELS 2011, Baltimore, USA
2. B. Zhou, A. Houard, Y. Liu, B. Prade, A. Mysyrowicz, A. Couairon, P. Mora, C. Smeenk, L. Arissian and P. Corkum, "Spontaneous currents inside air filaments", oral talk CLEO/QELS 2011, Baltimore, USA
3. B. Zhou, B. Prade, J. Larour, A. Houard, A. Mysyrowicz, "Direct measurement of oscillating currents in filaments", 3rd International Symposium on Filamentation (COFIL 2010), 31 May- 05 June 2010, Crete, Greece
4. B. Zhou, S. Akturk, B. Prade, Y. B. Andre, A. Houard, Y. Liu, M. Franco, C. D'Amico, E. Salmon, Z. Q. Hao, N. Lascoux and A. Mysyrowicz, "Long Time Revival of Femtosecond Laser Plasma Filaments in Air", CLEO Pacific Rim 2009, Shanghai, China
5. C.L. Arnold, S. Akturk, B. Zhou, M. Franco, A. Couairon, and A. Mysyrowicz, "Compression of ultrashort laser pulses in planar hollow waveguides", 18th International Laser Physics Workshop (LPHYS'09), July 13 - 17 2009, Barcelona, Spain
6. C.L. Arnold, S. Akturk, B. Zhou, M. Franco, A. Couairon, and A. Mysyrowicz, "Compression of Ultrashort Laser Pulses in a Planar Hollow Waveguide", CLEO Europe 2009, CF9.3, 14-19 juin 2009, Munich, Germany
7. S. Akturk, B. Zhou, B. Pasquiou, A. Houard, M. Franco, A. Couairon and A. Mysyrowicz, Retaining high laser intensities and generating plasma channels

over long distances in air by using an axicon, Ultrafast Phenomena, TUE51.17, 9-13 juin 2008, Stresa, Lago Maggiore, Italy

8. S. Akturk, B. Zhou, B. Pasquiou, A. Houard, M. Franco, A. Couairon and A. Mysyrowicz, "Generation of Long Plasma Channels in Air by Using Axicon-Generated Bessel Beams", CLEO/QELS 2008, CWI7, 4-9 mai 2008, San Jose, USA
9. B. Zhou, S. Akturk, B. Prade, Y.-B. Andre, A. Houard, Y. Liu, M. Franco, C. D'Amico, E. Salmon, Z. Q. Hao, N. Lascoux and A. Mysyrowicz, "Long Time Revival of Femtosecond Laser Plasma Filaments in Air", CLEO/IQEQ 2009, CMU4, 1-5 juin 2009, Baltimore, USA
10. S. Akturk, C.L. Arnold, B. Zhou, M. Franco, A. Couairon, and A. Mysyrowicz, "Compression of High Energy Ultrashort Laser Pulses in Hollow Planar Waveguides", CLEO/IQEQ 2009, CMU4, 1-5 juin 2009, Baltimore, USA
11. B. Zhou et al. "Coincidence of polarization dependent and independent anti-Stokes line emission by a few cycle pulse in birefringent photonic crystal fiberr", CLEO, Oct, 2006, USA

Bibliography

- [Ackermann 2004] R. Ackermann, K. Stelmaszczyk, P. Rohwetter, G. Méjean, E. Salmon, J. Yu, J. Kasparian, G. Méchain, V. Bergmann, S. Schaper, B. Weise, T. Kumm, K. Rethmeier, W. Kalkner, L. Wöste and J.-P. Wolf. *Triggering and guiding of megavolt discharges by laser-induced filaments under rain conditions*. Appl. Phys. Lett., vol. 85, no. 23, pages 5781–5783, 2004. 1
- [Agostini 1979] KP. Agostini, F. Fabre, G. Mainfray, G. Petite and N. K. Rahman. *Free-Free Transitions Following Six-Photon Ionization of Xenon Atoms*. Phys. Rev. L, vol. 42, no. 17, 1979. 135
- [Akturk 2004] S. Akturk, M. Kimmel, P. O. Shea and R. Trebino. *Extremely simple device for measuring 20 fs pulses*. Opt.Lett., vol. 29, pages 1025–1027, 2004. 132
- [Akturk 2007] Selcuk Akturk, Ciro D’Amico, Michel Franco, Arnaud Couairon and Andre Mysyrowicz. *Pulse shortening, spatial mode cleaning, and intense terahertz generation by filamentation in xenon*. Phys. Rev. A, vol. 76, no. 6, page 063819, 2007. 27, 54
- [Akturk 2008a] S. Akturk, C. D’Amico and A. Mysyrowicz. *Measuring Ultrashort Pulses in the Single-Cycle Regime using Frequency Resolved Optical Gating*. J. Opt. Soc. Am. B, vol. 25, no. 6, pages A63–A69, 2008. 33
- [Akturk 2008b] S. Akturk, B. Zhou, B. Pasquiou, M. Franco and A. Mysyrowicz. *Intensity distribution around the focal regions of real axicons*. Opt. Com., vol. 281, page 4240, 2008. 23
- [Akturk 2008c] Selcuk Akturk, Ciro D’Amico and Andre Mysyrowicz. *Measuring ultrashort pulses in the single-cycle regime using frequency-resolved optical gating*. J. Opt. Soc. Am. B, vol. 26, no. 6, pages A63–A69, 2008. 107, 133
- [Akturk 2009] Selcuk Akturk, Cord L. Arnold, Bing Zhou and Andre Mysyrowicz. *High-energy ultrashort laser pulse compression in hollow planar waveguides*. Opt. Lett., vol. 34, no. 9, pages 1462–1464, 2009. 94, 99, 100, 101, 108
- [Arnold 2009] C. L. Arnold, S. Akturk, M. Franco, A. Couairon and A. Mysyrowicz. *Compression of ultrashort laser pulses in planar hollow waveguides: a stability Analysis*. Opt. Express, vol. 17, no. 13, pages 11122–11129, 2009. 94, 99, 100, 101, 102
- [Baltuska 1998] A. Baltuska, M. S. Pshenichnikov and D. Wiersma. *Amplitude and phase characterization of 4.5 fs pulses by frequency-resolved optical gating*. Opt. Lett., vol. 23, pages 1474–1476, 1998. 133

- [Bespalov 1966] V. I. Bespalov and V. I. Talanov. *Filamentary structure of light beams in nonlinear liquids*. Zh. Eksper. Teor. Fiz. Pis'ma, vol. 3, pages 471–476, 1966. [JETP Lett. 3 (1966) 307-310]. 101
- [Bespalov 2002] V. G. Bespalov, S. A. Kozlov, Yu. A. Shpolyanskiy and I. A. Walmsley. *Simplified field wave equations for the nonlinear propagation of extremely short light pulses*. Phys. Rev. A, vol. 66, page 013811, 2002. 6
- [Bohman 2008] Samuel Bohman, Akira Suda, Masanori Kaku, Muhammad Nurhuda, Takuya Kanai, Shigeru Yamaguchi and Katsumi Midorikawa. *Generation of 5 fs, 0.5 TW pulses focusable to relativistic intensities at 1 kHz*. Opt. Express, vol. 16, no. 14, pages 10684–10689, 2008. 90
- [Bourayou 2005] R. Bourayou, G. Méjean, J. Kasparian, M. Rodriguez, E. Salmon, J. Yu, H. Lehmann, B. Stecklum, U. Laux, J. Eislöffel, A. Scholz, A. P. Hatzes, R. Sauerbrey, L. Wöste and J.-P. Wolf. *White-light filaments for multiparameter analysis of cloud microphysics*. J. Opt. Soc. Am. B, vol. 22, no. 2, pages 369–377, 2005. 1
- [Boyd 2003] R. W. Boyd. *Nonlinear optics*. Academic Press, 2003. 18
- [Brabec 1997] T. Brabec and F. Krausz. *Nonlinear Optical Pulse Propagation in the Single-Cycle Regime*. Phys. Rev. Lett., vol. 78, no. 17, pages 3282–3285, 1997. 97
- [Braun 1995] A. Braun, G. Korn, X. Liu, D. Du, J. Squier and G. Mourou. *Self-channeling of high-peak-power femtosecond laser pulses in air*. Opt. Lett., vol. 20, no. 1, pages 73–75, 1995. 1
- [Brueckne 1974] K.A. Brueckne and S. Jorna. *Laser-Driven Fusion*. Reviews Of Modern Physics, vol. 46, no. 2, pages 325–367, 1974. 88
- [Burch 1958] D. S. Burch, S. J. Smith and L. M. Branscomb. *Photodetachment of O₂*. Phys. Rev. 112, 171-175 (1958), vol. 112, pages 171–175, 1958. 36
- [Casto 1981] S. C. Casto, H. F. Schaefer and R. M. Pitzer. *Electronic structure of the N₄⁺ molecular ion*. J. Chem. Phys., vol. 74, no. 1, page 550, 1981. 40
- [Chen 2006] F. Chen. *Introduction to plasma physics and controlled fusion*. Springer, 2006. 21, 34
- [Chen 2008] Jianfang Chen, Akira Suda, Eiji J. Takahashi, Muhammad Nurhuda and Katsumi Midorikawa. *Compression of intense ultrashort laser pulses in a gas-filled planar waveguide*. Opt. Lett., vol. 33, no. 24, pages 2992–2994, 2008. 93, 109
- [Chen 2009] X. Chen, A. Jullien, A. Malvache, L. Canova, A. Borot, A. Trisorio, C. G. Durfee and R. Lopez-Martens. *Generation of 4.3 fs, 1 mJ laser pulses*

- via compression of circularly polarized pulses in a gas-filled hollow-core fiber.* Opt. Lett., vol. 34, no. 10, page 1588, 2009. 90
- [Chiao 1964] R. Y. Chiao, E. Garmire and C. H. Townes. *Self-trapping of optical beams.* Phys. Rev. Lett., vol. 13, no. 15, pages 479–482, 1964. 27
- [Chin 2002] S. L. Chin, A. Talebpour, J. Yang, S. Petit, V. P. Kandidov, O. G. Kosareva and M. P. Tamarov. *Filamentation of femtosecond laser pulses in turbulent air.* Appl. Phys. B, vol. 74, pages 67–76, 2002. 54
- [Chin 2005] S. L. Chin, S. A. Hosseini, W. Liu, Q. Luo, F. Théberge, N. Aközbek, A. Becker, V.P. Kandidov, O.G. Kosareva and H. Schröder. *The propagation of powerful femtosecond laser pulses in optical media: physics, applications and new challenges.* Canadian Journal of Physics, vol. 83, pages 863–905, 2005. 27
- [Chiron 1999] A. Chiron, B. Lamouroux, R. Lange, J.-F. Ripoche, M. Franco, B. Prade, G. Bonnaud, G. Riazuelo and A. Mysyrowicz. *Numerical simulations of the nonlinear propagation of femtosecond optical pulses in gases.* Eur. Phys. J. D, vol. 6, pages 383–396, 1999. 8
- [Comtois 2000] D. Comtois, C. Y. Chien, A. Desparois, F. Génin, G. Jarry, T. W. Johnston, J.-C. Kieffer, B. La Fontaine, F. Martin, R. Mawassi, H. Pépin, F. A. M. Rizk, F. Vidal, P. Couture, H. P. Mercure, C. Potvin, A. Bondiou-Clergerie and I. Gallimberti. *Triggering and guiding leader discharges using a plasma channel created by an ultrashort laser pulse.* J. Appl. Phys., vol. 76, no. 7, pages 819–821, 2000. 1
- [Corkum 1993] P. B. Corkum. *Plasma perspective on strong field multiphoton ionization.* Phys. Rev. Lett, vol. 71, pages 1994–1997, 1993. 70
- [Couairon 2000] A. Couairon and L. Bergé. *Modeling the filamentation of ultrashort pulses in ionizing media.* Phys. Plasmas, vol. 7, no. 1, pages 193–209, 2000. 7
- [Couairon 2002] A. Couairon and L. Bergé. *Light filaments in air for ultraviolet and infrared wavelengths.* Phys. Rev. Lett., vol. 88, no. 13, pages 135003 1–4, 2002. 6
- [Couairon 2003] A. Couairon. *Dynamics of femtosecond filamentation from saturation of self-focusing laser pulses.* Phys. Rev. A, vol. 68, page 015801, 2003. 7, 44
- [Couairon 2005a] A. Couairon, M. Franco, A. Mysyrowicz, J. Biegert and U. Keller. *Pulse-compression to the single cycle limit by filamentation in a gaz with a pressure gradient.* Opt. Lett., vol. 30, pages 2657–2659, 2005. 3, 89

- [Couairon 2005b] A. Couairon, M. Franco, A. Mysyrowicz, J. Biegert and U. Keller. *Pulse self-compression to the single-cycle limit by filamentation in a gas with a pressure gradient*. *Opt. Lett.*, vol. 30, no. 19, pages 2657–2659, 2005. 54
- [Couairon 2006] A. Couairon, J. Biegert, C. P. Hauri, W. Kornelis, F. W. Helbing, U. Keller and A. Mysyrowicz. *Self-compression of ultrashort laser pulses down to one optical cycle by filamentation*. *J. Mod. Optics*, vol. 53, pages 75–85, 2006. 98
- [Couairon 2007] A. Couairon and A. Mysyrowicz. *Femtosecond filamentation in transparent media*. *Physics Reports*, vol. 441, pages 47–189, 2007. 6, 7, 19, 21, 24, 36, 97
- [Courtois 2001] C. Courtois, A. Couairon, B. Cros, J. R. Marques and G. Matthieussent. *Propagation of intense ultrashort laser pulses in a plasma filled capillary tube: Simulations and experiments*. *Physics of Plasmas*, vol. 8, no. 7, pages 3445–3456, 2001. 99
- [Dalgarno 1966] A. Dalgarno and A. E. Kingston. *The refractive indices and Verdet constants of the inert gases*. *Proc. Roy. Soc. London Ser. A*, vol. 259, pages 424–429, 1966. 97
- [D’Amico 2007] C. D’Amico, A. Houard, M. Franco, B. Prade, A. Mysyrowicz, A. Couairon and V. T. Tikhonchuk. *Conical Forward THz Emission from Femtosecond-Laser-Beam Filamentation in Air*. *Phys. Rev. Lett.*, vol. 98, page 235002, 2007. 1, 3, 44
- [Depret 2002] B. Depret, P. Verkerk and D. Hennequin. *Characterization and modelling of the hollow beam produced by a real conical lens* *Opt. Commun.* 211, 31-38 (2002). *Opt. Commun.*, vol. 211, page 31, 2002. 12, 13, 23
- [Dickinson 2004] J. T. Dickinson, S. Orlando, S. M. Avanesyan and S. C. Langford. *Color center formation in soda lime glass and NaCl single crystals with femtosecond laser pulses*. *Appl. Phys. B*, vol. 79, pages 859–864, 2004. 108
- [Ding 2002] Z. Ding, H. Ren, Y. Zhao, J. S. Nelson and Z. Chen. *High-resolution optical coherence tomography over a large depth range with an axicon lens*. *Opt. Lett.*, vol. 27, no. 4, page 243, 2002. 11
- [Dorchies 1999] F. Dorchies, J. R. Marquès, B. Cros, G. Matthieussent, C. Courtois, T. Vélikorousov, P. Audebert, J. P. Geindre, S. Rebibo, G. Hamoniaux and F. Amiranoff. *Monomode Guiding of 10^{16} W/cm² Laser Pulses over 100 Rayleigh Lengths in Hollow Capillary Dielectric Tubes*. *Phys. Rev. Lett.*, vol. 82, no. 23, pages 4655–4658, Jun 1999. 102
- [Durfee 1993] C. G. Durfee and H. M. Milchberg. *Light pipe for high intensity laser pulses*. *Phys. Rev. Lett.*, vol. 71, no. 15, page 2409, 1993. 2, 12, 19

- [Durnin 1987] J. Durnin, J. J. Miceli Jr and J. H. Eberly. *Diffraction-free beams*. Phys. Rev. Lett., vol. 58, no. 15, page 1499, 1987. 2, 19, 33
- [Dutin 2010] C. Fourcade Dutin, A. Dubrouil, S. Petit, E. Mével, E. Constant and D. Descamps. *Post-compression of high-energy femtosecond pulses using gas ionization*. Opt. Lett., vol. 35, no. 2, pages 253–255, 2010. 90
- [Eisenmann 2007] S. Eisenmann, A. Pukhov and A. Zigler. *Fine Structure of a Laser-Plasma Filament in Air*. Phys. Rev. Lett., vol. 98, no. 15, page 155002, 2007. 21
- [Ekdahl 1980] C.A. Ekdahl. *Voltage and current sensor for a high-density z-pinch experiment*. Rev. Sci. Instrum., vol. 51, 1980. 45
- [Ell 2001] R. Ell, U. Morgner, F. X. Kartner, J. G. Fujimoto, E. P. Ippen, V. Scheuer, G. Angelow, T. Tschudi, M. J. Lederer, A. Boiko and B. Luther-Davies. *Generation of 5-fs pulses and octave-spanning spectra directly from a Ti:sapphire laser*. Opt. Lett., vol. 26, no. 6, pages 373–375, 2001. 88
- [Esarey 2009] E. Esarey, C. B. Schroeder and W. P. Leemans. *Physics of laser-driven plasma-based electron accelerators*. Rev. Mod. Phys., vol. 81, no. 3, pages 1229–1285, Aug 2009. 3, 44, 88
- [Faure 2006] J. Faure, C. Rechatin, A. Norlin, A. Lifschitz, Y. Glinec and V. Malka. *Controlled injection and acceleration of electrons in plasma wakefields by colliding laser pulses*. Nature, vol. 444, page 737, 2006. 44
- [Feit 1974] M. D. Feit and J. A. Fleck. *Effect of refraction on spot-size dependence of laser-induced breakdown*. Appl. Phys. Lett., vol. 24, no. 4, pages 169–172, 1974. 5
- [Feit 1988] M. D. Feit and J.A. Fleck, Jr. *Beam nonparaxiality, filament formation, and beam breakup in the self-focusing of optical beams*. J. Opt. Soc. Am. B, vol. 5, no. 3, page 633, 1988. 97
- [Fork 1987] R. L. Fork, C. H. Cruz, P. C. Becker and C. V. Shank. *Compression of optical pulses to six femtoseconds by using cubic phase compensation*. Opt. Lett., vol. 12, pages 483–485, 1987. 88
- [Gadonas 2001] R. Gadonas, V. Jarutis, R. Paskauskas, V. Smilgevicius, A. Stabinis and V. Vaicaitis. *Self-action of Bessel beam in nonlinear medium*. Opt. Commun., vol. 196, no. 1-6, page 309, 2001. 27
- [Gaeta 2000] A. L. Gaeta. *Catastrophic Collapse of Ultrashort Pulses*. Phys. Rev. Lett., vol. 84, no. 16, pages 3582–3585, 2000. 6
- [Gaižauskas 2006] E. Gaižauskas, E. Vanagas, V. Jarutis, S. Juodkazis, V. Mizeikis and H. Misawa. *Discrete damage traces from filamentation of Gauss–Bessel pulses*. Opt. Lett., vol. 31, page 80, 2006. 21, 27

- [Gallmann 1999] L. Gallmann, D. H. Sutter, N. Matuschek, G. Steinmeyer, U. Keller, C. Iaconis and I. A. Walmsley. *Characterization of sub-6-fs optical pulses with spectral phase interferometry for direct electric-field reconstruction*. OPT. LETT., vol. 24, no. 18, page 1314, 1999. 131
- [Garces-Chavez 2002] V. Garces-Chavez, D. McGloin, H. Melville, W. Sibbett, and K. Dholakia. *Simultaneous micromanipulation in multiple planes using a self-reconstructing light beam*. Nature 419, 145-147 (2002)., vol. 419, page 145, 2002. 12
- [Goulielmakis 008] E. Goulielmakis, M. Schultze, M. Hofstetter, V. S. Yakovlev, J. Gagnon, M. Uiberacker, A. L. Aquila, E. M. Gullikson, D. T. Attwood, R. Kienberger, F. Krausz and U. Kleineberg. *Single-cycle nonlinear optics*. Science, vol. 320, no. 5883, pages 1614–1617, JUN 20 2008. 88
- [Goulielmakis 2008] E. Goulielmakis, S. Koehler, B. Reiter, M. Schultze, A. J. Verhoef, E. E. Serebryannikov, A. M. Zheltikov and F. Krausz. *Ultrabroadband, coherent light source based on self-channeling of few-cycle pulses in helium*. Opt. Lett., vol. 33, no. 13, pages 1407–1409, 2008. 102
- [Grishkowsky 1990] D. Grishkowsky, S. Keiding, M. v. Exter and Ch. Fattinger. *Far-infrared time-domain spectroscopy with terahertz beams of dielectrics and semiconductors*. J. Opt. Soc. Am. B/Vol. 7, No. 10/October 1990, vol. 7, no. 10, page 2006, 1990. 51
- [Gu 2000] Min Gu. *Advanced optical imaging theory*. Springer, Berlin, 2000. 104
- [Guo 1998] C. Guo, M. Li, J. P. Nibarger and G. N. Gibson. *Single and double ionization of diatomic molecules in strong laser fields*. Phys. Rev. A, vol. 58, no. 6, page 4272, 1998. 73
- [Hao 2005] Z.Q. Hao, J. Zhang, Y.T. Liu, X. Lu, X.H. Yuan, Z.Y. Zheng, Z.H. Wang, W.J. Ling and Z.Y. Wei. *Prolongation of the fluorescence lifetime of plasma channels in air induced by femtosecond laser pulses*. Appl. Phys. B, vol. 80, pages 627–630, 2005. 2, 32
- [Hauri 2004] C. P. Hauri, W. Kornelis, F. W. Helbing, A. Heinrich, A. Couairon, A. Mysyrowicz, J. Biegert and U. Keller. *Generation of intense, carrier-envelope phase-locked few-cycle laser pulses through filamentation*. Appl. Phys. B, vol. 79, pages 673–677, 2004. 88, 90, 92
- [Hecht 1998] E. Hecht. *Optics*. Addison Wesley Longman, 1998. 14
- [Henis 2008] Z. Henis, G. Milikh, K. Papadopoulos and A. Zigler. *Generation of controlled radiation sources in the atmosphere using a dual femtosecond/nanosecond laser pulse*. J. Appl. Phys., vol. 103, page 103111, 2008. 32

- [Herman 1991] R. M. Herman and T. A. Wiggins. *Production and uses of diffractionless beams*. J. Opt. Soc. Am. A, vol. 8, no. 6, page 932, 1991. 12
- [Houard 2007] A. Houard, Y. Liu, A. Mysyrowicz and B. Leriche. *Calorimetric detection of the conical terahertz radiation from femtosecond laser filaments in air*. App. Phys. Lett., vol. 91, no. 24, 2007. 3, 44
- [Houard 2008] A. Houard, Y. Liu, B. Prade, V.T. Tikhonchuk and A. Mysyrowicz. *Strong enhancement of Terahertz radiation from laser filaments in air by a static electric field*. Phys. Rev. Lett., vol. 100, page 255006, 2008. 1
- [Iaconis 1998] C. Iaconis and I. A. Walmsley. *Spectral phase interferometry for direct electric-field reconstruction of ultrashort optical pulses*. OPT. LETT., vol. 23, no. 10, page 792, 1998. 131
- [Itikawaa 2006] Y. Itikawaa. *Cross Sections for Electron Collisions with Nitrogen Molecules*. J. Phys. Chem. Ref. Data, vol. 35, no. 1, page 31, 2006. 72, 136
- [Iwasakil 2003] A. Iwasakil, N. Akzbek, B. Ferland, Q. Luo, G. Roy, C.M. Bowden and S.L. Chin. *A LIDAR technique to measure the filament length generated by a high-peak power femtosecond laser pulse in air*. Appl. Phys. B, vol. 76, page 231, 2003. 34
- [Jaroszewicz 1993] Z. Jaroszewicz, J. Sochacki, A. Kolodziejczyk and L. R. Staron-ski. *Apodized annular-aperture logarithmic axicon: smoothness and uniformity of intensity distributions*. Opt. Lett, vol. 18, no. 22, page 1893, 1993. 12
- [Johannisson 2003] P. Johannisson, D. Anderson, M. Lisak and M. Marklund. *Non-linear Bessel beams*. Opt. Commun., vol. 222, page 107, 2003. 12, 19
- [Kandidov 1997] V. P. Kandidov, O. G. Kosareva, A. Brodeur and S. L. Chin. *State of the art of investigations into the filamentation of high-power subpicosecond laser pulses in gases*. Atmos. Oceanic Opt., vol. 10, no. 12, page 966, 1997. 8
- [Kane 1993] D. J. Kane and R. Trebino. *Characterization of arbitrary femtosecond pulses using frequency resolved optical gating*. IEEE J. Quantum Electron, vol. 29, page 571, 1993. 132
- [Kasparian 2001] J. Kasparian, M. Rodriguez, G. Méjean, J. Yu, E. Salmon, H. Wille, Y.-B. André R. Bourayou S. Frey, A. Mysyrowicz, R. Sauerbrey, J.-P. Wolf and L. Wöste. *White-Light Filaments for Atmospheric Analysis*. Science, vol. 301, no. 5629, pages 61–64, 2001. 1, 19
- [Kasparian 2003] J. Kasparian, M. Rodriguez, G. Mejean, J. Yu, E. Salmon, H. Wille, R. Bourayou, S. Frey, Y.B. Andre, A. Mysyrowicz, R Sauerbrey, JP Wolf and L Woste. *White-light filaments for atmospheric analysis*. Science, vol. 301, no. 5629, pages 61–64, 2003. 19

- [Keldysh 1960] L. V. Keldysh. *Kinetic theory of impact ionization in semiconductors*. Sov. Phys. JETP, vol. 37, no. 10, pages 509–518, 1960. 74
- [Keldysh 1965] L. V. Keldysh. *Ionization in the Field of a Strong Electromagnetic Wave*. Sov. Phys. JETP, vol. 20, pages 1307–1314, 1965. 74, 98
- [Keller 2003] U. Keller. *Recent developments in compact ultrafast lasers*. Nature, vol. 424, page 831, 2003. 89
- [Kim 2008] K. Y. Kim, A. J. Taylor, J. H. Glowina and G. Rodriguez. *Coherent control of terahertz supercontinuum generation in ultrafast laser–gas interactions*. Nature Photonics, vol. 2, pages 605–609, 2008. 81
- [Kim 2009] K. Y. Kim. *Generation of coherent terahertz radiation in ultrafast laser–gas interactions*. Phys. Plasmas, vol. 16, page 056706, 2009. 83
- [Kolesik 2004] M. Kolesik and J. V. Moloney. *Nonlinear optical pulse propagation simulation: From Maxwell’s to unidirectional equations*. Phys. Rev. E, vol. 70, page 036604, 2004. 97
- [Kornelis 2003] W. Kornelis, J. Biegert, J. W. G. Tisch, M. Nisoli, G. Sansone, C. Vozzi, S. De Silvestri and U. Keller. *Single-shot kilohertz characterization of ultrashort pulses by spectral phase interferometry for direct electric-field reconstruction*. Opt. Lett., vol. 28, pages 281–283, 2003. 131
- [Krausz 009] Ferenc Krausz and Misha Ivanov. *Attosecond physics*. Rev. Mod. Phys., vol. 81, no. 1, pages 163–234, JAN-MAR 2009. 39, 88
- [Laakmann 1976] Katherine D. Laakmann and William H. Steier. *Waveguides: characteristic modes of hollow rectangular dielectric waveguides*. Appl. Opt., vol. 15, no. 5, pages 1334–1340, 1976. 94, 95
- [Ladouceur 2001] H. D. Ladouceur, A. P. Baronavski, D. Lohrmann, P. W. Grounds and P. G. Girardi. *Electrical conductivity of a femtosecond laser generated plasma channel in air*. Opt. Commun., vol. 189, page 107, 2001. 31, 32
- [Lange 1998] H. R. Lange, J.-F. Ripoche, A. Chiron, B. Lamouroux, M. Franco, B. Prade, E.T.J. Nibbering and A. Mysyrowicz. *Time-Space Self-Compression of Femtosecond Laser Pulses in Air*. In Technical digest of the CLEO/IQEC conference, page 243, San Francisco, 1998. OSA. 8
- [Larour 2003] J. Larour and J. Wei. *High frequency performance of I-dot monitors based on annular grooves*. In Pulse Power Seminar, page 12. IEE Material and Devices Professional Network, 2003. 45
- [Lehmeier 1985] H. J. Lehmeier, W. Leupacher and A. Penzkofer. *Nonresonant third order hyperpolarizability of rare gases and N₂ determined by third harmonic generation*. Optics Commun., vol. 56, no. 1, pages 67–72, 1985. 62

- [L'Huillier 995] A. L'Huillier, T. Auguste, P. H. Balcou, B. Carre, P. Monot, P. Salieres, C. Altucci, M. B. Gaarde, J. Larsson, E. Mevel, T. Starczewski, S. Svanberg, C. G. Wahlstrom, R. Zerne, K. S. Budil, T. Ditmire and M. D. Perry. *High-order harmonics - a coherent source in the XUV range*. J. Nonl. Opt. Phys. Mat., vol. 4, no. 3, pages 647–665, JUL 1995. 88
- [Liu 2008] Y. Liu, A. Houard, B. Prade, A. Diaw, V.T. Tikhonchuk and A. Mysyrowicz. *Amplification of Transition-Cherenkov Terahertz Radiation of Femtosecond Filament in Air*. Appl. Phys. Lett., vol. 93, page 051108, 2008. 55
- [Manek 1998] I. Manek, Y. B. Ovchinnikov and R. Grimm. *Generation of a hollow laser beam for atom trapping using an axicon*. Opt. Commun., vol. 147, page 67, 1998. 12
- [Mangles 2004] S. P. D. Mangles, C. D. Murphy, Z. Najmudin, A. G. R. Thomas, J. L. Collier, A. E. Dangor, E. J. Dival, P. S. Foster, J. G. Gallacher, C. J. Hooker, D. A. Jaroszynski, A. J. Langley, W. B. Mori, P. A. Norreys, F. S. Tsung, R. Viskup, B. R. Walton and K. Krushelnick. *Monoenergetic beams of relativistic electrons from intense laser plasma interactions*. Nature, vol. 431, page 535, 2004. 44
- [Marburger 1975] J. H. Marburger. *Self-focusing: Theory*. Prog. Quant. Electr., vol. 4, pages 35–110, 1975. 5, 27
- [Marcatili 1964] E. A. J. Marcatili and R. A. Schmelzer. *Hollow Metallic and Dielectric Waveguides for Long Distance Optical Transmissions and Lasers*. Bell Syst. Tech. J., vol. 43, pages 1783–1809, 1964. 95
- [McLeod 1954] J. H. McLeod. *The Axicon: A new type of optical element*. JOSA, vol. 44, no. 8, page 592, 1954. 2, 11, 19
- [McLeod 50] J. H. McLeod. *Axicons and their uses*. J. Opt. Soc. Am., vol. 2, no. 166, page 1960, 50. 19
- [Méjean 2006] G. Méjean, R. Ackermann, J. Kasparian, E. Salmon, J. Yu, J.-P. Wolf, K. Rethmeier, W. Kalkner, P. Rohwetter, K. Stelmaszczyk and L. Wöste. *Improved laser triggering and guiding of megavolt discharges with dual fs-ns pulses*. Appl. Phys. Lett., vol. 88, page 021101, 2006. 32, 37
- [Mizrahi 1985] V. Mizrahi and D. P. Shelton. *Dispersion of nonlinear susceptibilities of Ar, N₂ and O₂ measured and compared*. Phys. Rev. Lett., vol. 55, no. 7, page 696, 1985. 53
- [Mysyrowicz 2008] A. Mysyrowicz, A. Couairon and U. Keller. *Self-compression of optical laser pulses by filamentation*. New J. Phys., vol. 10, page 025023, 2008. 90

- [Nibbering 1996] E. T. J. Nibbering, P. F. Curley, G. Grillon, B. S. Prade, M. A. Franco, F. Salin and A. Mysyrowicz. *Conical emission from self-guided femtosecond pulses in air*. Opt. Lett., vol. 21, no. 1, pages 62–64, 1996. 1
- [Nibbering 1997a] E. T. J. Nibbering, G. Grillon, M. A. Franco, B. S. Prade and A. Mysyrowicz. *Determination of the inertial contribution to the nonlinear refractive index of air, N₂, and O₂ by use of unfocused high-intensity femtosecond laser pulses*. J. Opt. Soc. Am. B, vol. 14, no. 3, pages 650–660, 1997. 7
- [Nibbering 1997b] E. T. J. Nibbering, G. Grillon, M. A. Franco, B. S. Prade and A. Mysyrowicz. *Determination of the inertial contribution to the nonlinear refractive index of air, N₂, and O₂ by use of unfocused high-intensity femtosecond laser pulses*. J. Opt. Soc. Am. B, vol. 14, no. 3, pages 650–660, 1997. 108
- [Nisoli 1997] M. Nisoli, S. de Silvestri, O. Svelto, R. Szipöcz, K. Ferencz, C. Spielmann, S. Sartania and F. Krausz. *Compression of high-energy laser pulses below 5 fs*. Opt. Lett., vol. 22, no. 8, pages 522–524, 1997. 88, 90
- [Nurhuda 2004] M. Nurhuda, A. Suda and K. Midorikawa. *Saturation of nonlinear susceptibility*. Journal of Nonlinear Optical Physics & Materials, vol. 13, no. 2, pages 301–313, 2004. 62
- [Nurhuda 2006] Muhammad Nurhuda, Akira Suda, Samuel Bohman, Shigeru Yamaguchi and Katsumi Midorikawa. *Optical Pulse Compression of Ultrashort Laser Pulses in an Argon-Filled Planar Waveguide*. Phys. Rev. Lett., vol. 97, no. 15, page 153902, Oct 2006. 93
- [Paul 2001] P. M. Paul, E. S. Toma, P. Breger, G. Mullot, F. Augé, P. Balcou, H. G. Muller and P. Agostini. *Observation of Train of Attosecond Pulses from High Harmonic Generation*. Science, vol. 292, page 1689, 2001. 88
- [Perelomov 1966] A. M. Perelomov and V. S. Popov. *Ionization of atoms in an alternating electric field*. Sov. Phys. JETP, vol. 23, pages 924–934, 1966. 98
- [Polesana 2002] P. Polesana, D. Faccio, P. Di Trapani, A. Dubietis, A. Piskarkas, A. Couairon and M. A. Porras. *High localization, focal depth and contrast by means of nonlinear Bessel Beams*. Opt. Express, vol. 13, no. 16, page 6160, 2002. 19, 24
- [Polesana 2006] P. Polesana, A. Dubietis, M. A. Porras, E. Kučinskas, D. Faccio, A. Couairon and P. Di Trapani. *Near-field dynamics of ultrashort pulsed Bessel beams in media with Kerr nonlinearity*. Phys. Rev. E, vol. 73, page 056612, 2006. 19
- [Polesana 2007] P. Polesana, A. Couairon, D. Faccio, A. Parola, M. A. Porras, A. Dubietis, A. Piskarkas and P. Di Trapani. *Observation of conical waves*

- in focusing, dispersive and dissipative Kerr media.* Phys. Rev. Lett., 2007. 19
- [Polesana 2008] P. Polesana, M. Franco, A. Couairon, D. Faccio and P. Di Trapani. *Filamentation in Kerr media from pulsed Bessel beams.* Phys. Rev. A, vol. 77, page 043814, 2008. 22, 27
- [Polyakov 2001] Sergey Polyakov, Fumiyo Yoshino and George Stegeman. *Interplay between self-focusing and high-order multiphoton absorption.* J. Opt. Soc. Am. B, vol. 18, no. 12, pages 1891–1895, 2001. 27
- [Porras 2004] M. A. Porras, A. Parola, D. Faccio, A. Dubietis and P. Di Trapani. *Nonlinear unbalanced Bessel beams: Stationary conical waves supported by nonlinear losses.* Phys. Rev. Lett., vol. 93, no. 15, page 153902, 2004. 19
- [Proulx 2000] A. Proulx, A. Talebpour, S. Petit and S. L. Chin. *Fast pulsed electric field created from the self-generated filament of a femtosecond Ti:Sapphire laser pulse in air.* Optics Commun., vol. 174, pages 305–309, 2000. 3, 45
- [Pyragaite 2006] V. Pyragaite, K. Regelskis, V. Smilgevicius and A. Stabinis. V. Pyragaite, K. Regelskis, V. Smilgevicius, and A. Stabinis, "Self-action of Bessel light beams in medium with large nonlinearity." Opt. Commun., vol. 257, page 139, 2006. 19
- [Rioux 1978] M. Rioux, R. Tremblay and P. A. Belanger. *Linear, annular, and radial focusing with axicons and applications to laser machining* Appl. Opt. Appl. Opt., vol. 17, no. 10, page 1532, 1978. 12
- [Ripoche 1997] J. F. Ripoche, G. Grillon, B. Prade, M. Franco, E. Nibbering, R. Lange and A. Mysyrowicz. *Determination of the time dependence of n_2 in air.* Opt. Commun., vol. 135, pages 310–314, 1997. 7, 53
- [Rodriguez 2002] M. Rodriguez, R. Sauerbrey, H. Wille, L. Woste, T. Fujii, Y.B. Andre, A. Mysyrowicz, L. Klingbeil, K. Rethmeier, W. Kalkner, J. Kasparian, E. Salmon, J. Yu and J.P. Wolf. *Triggering and guiding megavolt discharges by use of laser-induced ionized filaments.* Opt. Lett., vol. 27, no. 9, pages 772–774, 2002. 1
- [Rogowski 1912] W. Rogowski and W. Steinhaus. *Die Messung der magnetischen Spannun.* Arch Elektrotech, vol. 1, no. 4, page 141, 1912. 45, 47
- [Roskey 2007] D. E. Roskey, M. Kolesik, J. V. Moloney and E. M. Wright. *Self-action and regularized self-guiding of pulsed Bessel-like beams in air.* Optics Express, vol. 15, no. 16, page 9893, 2007. 2, 19, 22, 27
- [Schenkel 2003] B. Schenkel, J. Biegert, U. Keller, C. Vozzi, M. Nisoli, G. Sansone, S. Stagira, S. De Silvestri and O. Svelto. *Generation of 3.8-fs pulses from adaptive compression of a cascaded hollow fiber supercontinuum.* Opt. Lett., vol. 28, no. 20, pages 1987–1989, 2003. 88

- [Schillinger 1999] H. Schillinger and R. Sauerbrey. *Electrical conductivity of long plasma channels in air generated by self-guided femtosecond laser pulses*. Appl. Phys. B, vol. 68, pages 753–756, 1999. 31
- [Shelton 1990] D. P. Shelton. *Nonlinear-optical susceptibilities of gases measured at 1064 and 1319 nm*. Phys. Rev. A, vol. 42, no. 5, pages 2578–2592, 1990. 62, 109
- [Shimoji 1989] Y. Shimoji, A. T. Fay, R. S. F. Chang and N. Djeu. *Direct measurement of the nonlinear refractive index of air*. Opt. Lett., vol. 6, no. 11, pages 1994–1996, 1989. 53
- [Shon 2001] N. H. Shon, A. Suda, Y. Tamaki and K. Midorikawa. *High-order harmonic and attosecond pulse generations: Bulk media versus hollow waveguides*. Phys. Rev. A, vol. 63, page 063806, 2001. 88
- [Siegman 1986] A. E. Siegman. *Lasers*. University Science Books, Sausalito, California, 1986. 111
- [Sprangle 2002] P. Sprangle, J. R. Peñano and B. Hafizi. *Propagation of intense short laser pulses in the atmosphere*. Phys. Rev. E, vol. 66, no. 4, page 046418, 2002. 6
- [Stelmaszczyk 2004] K. Stelmaszczyk, P. Rohwetter, G. Méjean, J. Yu, E. Salmon, J. Kasparian, R. Ackermann, J.-P. Wolf and L. Wöste. *Long-distance remote laser-induced breakdown spectroscopy using filamentation in air*. Appl. Phys. Lett., vol. 85, no. 18, pages 3977–3979, 2004. 1
- [Stolen 1989] R. H. Stolen, J. P. Gordon, W. J. Tomlison and H. A. Haus. *Raman response function of silica-core fibers*. J. Opt. Soc. Am. B, vol. 6, no. 6, pages 1159–1166, 1989. 5
- [Stolen 1992] R. H. Stolen and W. J. Tomlison. *Effect of the Raman part of the nonlinear refractive index on propagation of ultrashort optical pulses in fibers*. J. Opt. Soc. Am. B, vol. 9, no. 4, pages 565–573, 1992. 5
- [Strickland 1985] D. Strickland and G. Mourou. *Compression of amplified chirped optical pulses*. Opt. Comm., vol. 56, page 219, 1985. 88
- [Subramanian 1987] K. P. Subramanian and V. Kumar. *Total electron scattering cross sections for argon, krypton and xenon at low electron energies*. J. Phys. B: At. Mol. Phys., vol. 20, page 5505, 1987. 72, 136
- [Suda 2005] Akira Suda, Masatoshi Hatayama, Keigo Nagasaka and Katsumi Midorikawa. *Generation of sub-10-fs, 5-mJ-optical pulses using a hollow fiber with a pressure gradient*. Appl. Phys. Lett., vol. 86, page 111116, 2005. 90
- [Tajima 1979] T. Tajima and J. M. Dawson. *Laser Electron Accelerator*. Phys. Rev. Lett., vol. 43, page 267, 1979. 44

- [Tanaka 2000] T. Tanaka and S. Yamamoto. *Comparison of aberration between axicon and lens* *Opt. Commun.* 184(113-118)(2000). *Opt. Commun.*, vol. 184, page 113, 2000. 12
- [Tempea 1998] Gabriel Tempea and Thomas Brabec. *Theory of self-focusing in a hollow waveguide*. *Opt. Lett.*, vol. 23, pages 762–764, 1998. 97, 99
- [Tzortzakis 1999] S. Tzortzakis, M.A. Franco, Y.B. Andre, A. Chiron, B. Lamouroux, B.S. Prade and A. Mysyrowicz. *Formation of a conducting channel in air by self-guided femtosecond laser pulses*. *Phys. Rev. E*, vol. 60, no. 4, pages R3505–R3507, 1999. 31
- [Tzortzakis 2000] S. Tzortzakis, B. Prade, M. Franco and A. Mysyrowicz. *Time-evolution of the plasma channel at the trail of a self-guided IR femtosecond laser pulse in air*. *Opt. Commun.*, vol. 181, no. 1-3, pages 123–127, 2000. 31, 32
- [Valdmanis 1986] A.J . Valdmanis and L. R. Fork. *Design considerations for a femtosecond pulse laser balancing self phase modulation, group velocity dispersion, saturable absorption, and saturable gain*. *IEEE J.Quantum Electron*, vol. 22, pages 112–118, 1986. 88
- [Vujicic 2006] N. Vujicic, H. Skenderovic, T. Ban, D. Aumiler and G. Pichler. *Low-density plasma channels generated by femtosecond pulses*. *Appl. Phys. B*, vol. 82, no. 3, page 377, 2006. 21
- [Wagner 2004] Nicholas L. Wagner, Emily A. Gibson, Tenio Popmintchev, Ivan P. Christov, Margaret M. Murnane and Henry C. Kapteyn. *Self-Compression of Ultrashort Pulses through Ionization-Induced Spatiotemporal Reshaping*. *Phys. Rev. Lett.*, vol. 93, no. 17, page 173902, Oct 2004. 102
- [Wells 2002] E. Wells, M. J. DeWitt and R. R. Jones. *Comparison of intense-field ionization of diatomic molecules and rare-gas atoms*. *Phys. Rev. A*, vol. 66, page 013409, 2002. 73
- [Wille 2002] H. Wille, M. Rodriguez, J. Kasparian, D. Mondelain, J. Yu, A. Mysyrowicz, R. Sauerbrey, J. P. Wolf and L. Wöste. *Teramobile: a Mobile Femtosecond-Terawatt Laser and Detection System*. *European Physical Journal - Appl. Phys.*, vol. 20, pages 183–190, 2002. 33
- [Xu 2009] H.L. Xu, A. Azarm, J. Bernhardt, Y. Kamali and S.L. Chin. *The mechanism of nitrogen fluorescence inside a femtosecond laser filament in air*. *Chemical Physics*, vol. 360, page 171, 2009. 37
- [Yablonovitch 1972a] E. Yablonovitch and N. Bloembergen. *Avalanche Ionization and the Limiting Diameter of Filaments Induced by Light Pulses in Transparent Media*. *Phys. Rev. Lett.*, vol. 29, no. 14, pages 907–910, 1972. 7, 36, 98

- [Yablonovitch 1972b] Eli Yablonovitch and N. Bloembergen. *Avalanche Ionization and the Limiting Diameter of Filaments Induced by Light Pulses in Transparent Media*. Phys. Rev. Lett., vol. 29, no. 14, pages 907–910, Oct 1972. 37
- [Yang 2002] H. Yang, J. Zhang, W. Yu, Y. J. Li and Z. Y. Wei. *Long plasma channels generated by femtosecond laser pulses*. Phys. Rev. E, vol. 65, no. 1, page 016406, 2002. 2, 32
- [Yariv 1989] Amnon Yariv. Quantum electronics, 3rd edition. Wiley, January 1989. 95
- [Yu 2001] J. Yu, D. Mondelain, G. Ange, R. Volk, S. Niedermeier, J. P. Wolf, J. Kasparian and R. Sauerbrey. *Backward supercontinuum emission from a filament generated by ultrashort laser pulses in air*. Opt. Lett., vol. 26, no. 8, page 533, 2001. 1
- [Yu 2004] W. Yu, M. Y. Yu, J. Zhang, L. J. Qian, X. Yuan, P. X. Lu, R. X. Li, Z. M. Sheng, J. R. Liu and Z. Z. Xu. *Long-distance propagation of intense short laser pulse in air*. Phys. Plasmas, vol. 11, no. 11, page 5360, 2004. 54, 88
- [Zaïr 2007] A. Zaïr, A. Guandalini, F. Schapper, M. Holler, J. Biegert, L. Gallmann, U. Keller, A. Couairon, M. Franco and A. Mysyrowicz. *Spatio-temporal characterization of few-cycle pulses obtained by filamentation*. Opt. Express, vol. 15, no. 9, page 5394, 2007. 19
- [Zhao 1995] X. M. Zhao, J.-C. Diels, C. Y. Wang and J. M. Elizondo. *Propagation dynamics of intense femtosecond pulses: Multiple splittings, coalescence, and continuum generation*. IEEE J. Quantum Electron., vol. 31, page 599, 1995. 2, 31, 32, 36
- [Zhu 2006] J. Zhu, Z. Ji, Y. Deng, J. Liu, R. Li and Z. Xu. *Long lifetime plasma channel in air generated by multiple femtosecond laser pulses and an electrical field*. Opt. Exp., vol. 14, page 4915, 2006. 32

Laser Nonlinear Propagation In Gases: The Properties And Applications

Abstract:

When an intense femtosecond laser pulse propagates in a gas, it undergoes filamentation, a spectacular process where the pulse spatial, spectral and temporal characteristics change considerably. A thin short-lived plasma column is formed in the wake of the propagating pulse. My PhD work has been dedicated to the further understanding of the filamentation process. In a first part, I compare the properties of a usual filament with those of a filament formed by a femtosecond laser pulse with a Bessel beam profile. Using a laser pulse of same intensity and duration, I show that a Bessel beam can form a longer and more uniform plasma column in air, but that the plasma density is significantly lower. In a second part, I show that it is possible to increase considerably the lifetime of the plasma column, using a dual femtosecond/nanosecond laser pulse technique. To obtain an increased lifetime over a significant segment of a plasma column, I rely on the properties of Bessel beams in the nonlinear regime developed in the first chapter. In a third part, I study the dynamics of free electrons that are produced in the filamentation process. To do this, I have developed a specially designed current probe. Experiments reveal a very rich behaviour. The longitudinal displacements of electrons in the plasma column depend sensitively on the nature of the gas and its pressure as well as on the laser polarization of the laser. I propose a model to explain this behaviour. The direction of electron flow results from the competition between pure laser forces and a Coulomb wake field force. In the last chapter, I study filamentation in a Helium gas. This required improving the laser characteristics in order to reach the necessary power for filamentation. Improved characteristics have been achieved by implementing a planar compression stage which shortened the laser pulse from 50 fs to 10 fs without appreciable energy loss. The first experimental evidence for filamentation in He is presented at the end of the thesis. Agreement is found with a numerical simulation.

Keywords: Filamentation, Bessel beam, Axicon, Oscillating current, Planar wave guide.
